Improving the Accuracy of Image Co-registration in InSAR

by

Weibao Zou

The dissertation presented for the Degree

of Doctor of Philosophy

Department of Land Surveying & Geo-Informatics
The Hong Kong Polytechnic University
Hung Hom, Kwonloon, Hong Kong

Dec., 2004

Improving the Accuracy of Image Co-registration in InSAR

The dissertation submitted in partial fulfillment of the requirements for the Degree of Doctor of Philosophy

Weibao Zou

Chief supervisor:	***Prof. Zhilin Li***
Co-supervisor:	***Dr. XiaoLi Ding***
	Prof. Yongqi Chen

Department of Land Surveying & Geo-Informatics
The Hong Kong Polytechnic University
Dec., 2004

CERTIFICATE OF ORIGINALITY

I hereby declare that this thesis is my own work and that, to the best of my knowledge and belief, it reproduces no material previously published or written nor material which has been accepted for the award of any other degree or diploma, except where due acknowledgement has been made in the text.

_________________(Signed)

Weibao ZOU (Name of student)

ABSTRACT

Synthetic aperture radar interferomery (InSAR) has gained attention in many fields because of its accuracy, convenience and efficiency. It has been demonstrated to be a potential tool for generating digital elevation models (DEM).

But many critical factors affect the robustness and accuracy of InSAR technology and limit its applications and development. This project is devoted to improving the accuracy of DEM generated by InSAR. Some factors influencing on the accuracy of SAR image co-registration have been systematically investigated.

Firstly, a quantitative measure for the quality of interferogram is proposed based on the sum of phase difference (SPD). The simulation results show the variation of the quality of an interferogram can be correctly reflected by the value of SPD.

When lacking of well-defined tiepoint for co-registration, the tiepoints are selected in grid form. In order to understand the effects of tiepoint interval on the reliability of co-registration, a series of experiments with different grid sizes have been carried out. The effects of the tiepoint interval and the accuracy of DEM were systematically investigated. The tiepoint interval is not a very sensitive parameter. However, a tiepoint interval with around 200*30 pixels is an appropriate grid size for tiepoint, which can make results more reliable.

If feature points are available, more accurate co-registration can be achieved. To extract the feature points, a method is proposed. The extraction of such points is based on the wavelet gradient modulus maximum after decomposing SAR images. The feature points extracted by wavelet and the tiepoints selected in grid form should be combined together for a reliable co-registration. The experimental results show that the reliability of co-registration was improved by the method. Specially, the accuracy of DEM was improved by 16%~35%.

The window size is a factor to be considered for tiepoint matching in co-registration. Optimum window size can be determined based on the autocorrelation of SAR image, which indicates the degree of similarity between pixels in an image. With wavelet, the autocorrelation coefficient can be decomposed into different frequency components. By analyzing the variation of amplitude, the optimum window size can be determined. The experimental results show that it is a reliable method to determine the optimum window size by decomposing autocorrelation coefficient with wavelet.

Finally, a system for automated SAR image co-registration is implemented. It fuses all techniques developed in this project systematically and efficiently for enhancing the accuracy of co-registration.

Acknowledgements

The research was carried out under the direction of my chief supervisor, Prof. Zhilin Li, as well as two co-supervisors, Dr. Xiaoli Ding and Prof. Yongqi Chen. I would like to express my sincere gratitude to them. Without their enthusiasm in scientific research, enlightening guidance, continuous support and great encouragement, I could not successfully finish the research work and the dissertation. I am truly grateful to them for their encouragement, invaluable advice, and patient guidance during this work.

I am thankful for the financial support by a grant from the Research Grants Council of the Hong Kong Special Administrative Region (Project No. PolyU 5070/00E) and from the Hong Kong Polytechnic University (Grant No.: G-T179).

Special appreciations go to my former colleague Dr. Guoxiang Liu, currently in Southwest Jiaotong University, China; Mr. Zhiwei Li, a Ph.D candidate in the department and Prof. Dawei Zheng, Research Fellow in the department and Professor of the Shanghai Astronomical Observatory for their many helpful discussions and suggestions for the research and sharing of research experiences with me.

I am very grateful to Mr. Kevin Kawai Kwan, Dr. Tracy C.K. Cheung, Mr. Charles Man Sing Wong and Mr. Yan Wai Yeung for their enthusiastic help.

I would like to thank both of the former and the current Chairmen of the Departmental Research Committee, Prof. Christopher Gold and Dr. Xiaoli Ding, for their efficient management and a series of interesting seminars and lectures organised by them.

I would also like to thank the research colleagues in the Department, Ahmed Shaker, Asma Ibrahim, Eric K. Forkuo, Kourosh Khoshelham, Meng Yu, Ng Hoi Man, Peter Damoah-Afari, Xinghua Zhou and Zhu Xu, for sharing with me their research experiences and making my studies more enjoyable.

Last but not least, I thank my family right from the bottom of my heart for their love and understanding during my Ph.D study.

Table of Contents

Abstract

Acknowledgements

Table of content

List of figures

List of tables

List of Figures

List of Tables

Chapter 1

Introduction

1.1 Significance of the research

Interferometric Synthetic Aperture Radar (InSAR) has undergone rapid development since its first proposal by Graham in 1974. Within three decades, InSAR has gained increasing attention from researchers in a variety of areas due to its advantages of all weather conditional, rapid and accurate topographic data collection (Zebker et al., 1994a). As a result, it has matured to be a widely applied technique in many fields (Hanssen, 2000), such as surface deformation monitoring (Rosen et al., 1996; Tobita et al., 1998; Liu, 2003); forest management and classification (Askne and Hagberg, 1993; Varekamp and Hoekman, 2001; Wegmller and Werner, 1997; Weydahl, 2001); ocean currents and glacier movement monitoring (Mattar et al., 1998; Joughin et al., 1998; Wangensteen et al., 1999); hydrologic studies (Ludwing et al., 1998) and polar research (Madsen et al., 1993; Shi et al., 1994).

InSAR is a potential technique for generating digital elevation models (DEM) by using the phase component of the complex radar signal (Gens, 1998). A DEM is one of the most demanded products in the remote sensing community (Gens, 1998). It is widely used within the geoscientific community, e.g. for mapping purposes, geomorphological studies based on slope and aspect maps, and as a layer in geographical information systems (GIS) for combining relief data with thematic information. A properly equipped spaceborne InSAR system can be used to produce a highly accurate global DEM with its advantages in significantly less time and at significantly lower cost than other systems (Hilland et al., 1998). This greatly attracts researchers' attention in military field. In the navigation field, a highly accurate DEM is one of the important information for improving the accuracy of the navigational system (Burgett, 1993; Layne and Paschall, 1994; Guarino and Ibsen, 1995; Li and Zelnio, 1996; Hilland et al., 1998; Fornaro, 1999).

In short, InSAR is enjoying widespread applications in many fields. It is a promising technique to solve some difficult problems in a study area accurately, economically, conveniently and efficiently, rapidly gaining attention in many fields. There are, however, numerous critical factors affecting the quality of InSAR data. One such factor is the SAR image co-registration that determines both the robustness and the accuracy of InSAR technology and limit its applications and developments. There is no doubt that improving the accuracy of image co-registration in InSAR will greatly benefit the development of InSAR technology in civilian and military applications.

1.2 Researches on InSAR: An overview

1.2.1 Historical development of InSAR

The concept of Synthetic Aperture Radar (SAR) is usually attributed to Carl Wiley of Goodyear Aircraft Corporation in 1951 (Wiley, 1965). At the University of Illinois, a group of scientists have validated the first experiment in 1953 (Sherwin et al., 1962);

later on, the U.S. Army commissioned Project Wolverine on this subject to the University of Michigan. This was the beginning of a series of activities that contributed to the development of SAR techniques (Franceschetti and Lanari, 1999).

Beginning in the late 1960s, NASA began to sponsor the development of SAR systems for civilian application. Jet Propulsion Laboratory (JPL) developed for NASA an L-band SAR sensor. This was installed in 1962 on a rocket and tested during a set of experiments carried out at the New Mexico missile test site. This sensor was finally installed onboard (NASA CV-990 airplane) in 1966 and subsequently upgraded by JPL again (Franceschetti and Lanari, 1999; Hanssen, 2000).

Environmental Research Institute of Michigan (ERIM) and JPL jointly conducted the Apollo Lunar Sounder experiment, which successfully flew onboard the Apollo 17 lunar orbiter in 1972 (Porcello et al., 1974).

NASA approved the Shuttle Imaging Radar (SIR) flight series. The program started with the SIR-A experiment flown in 1981. The SIR-B mission was launched in 1984 (Franceschetti et al., 1995).

The European Space Agency (ESA) has also contributed to SAR technology development with the launch of two flying C-band sensor: ERS-1 and ERS-2. The former was successfully launched in 1991 and the latter in 1995 (Franceschetti and Lanari, 1999).

Other countries have also been involved in the development of free-flying spaceborne SAR sensors for civilian applications. Russian launched the S-band in 1991; Japan, the L-band sensor JERS-1 in 1992; and Canada, the RADARSAT sensor equipped with a multimode C-band system in 1995 (Hanssen, 2000).

A very important feature of SAR application is represented by interplanetary missions. In addition to spaceborne SAR missions, many airborne SAR sensors have also been developed over the years. Airborne operations are more flexible than spaceborne operations and are more commonly practiced nowadays. A large number of SAR sensors are already planned for the near future (Hilland et al., 1998).

SAR interferometric data can provide information on three-dimensional objects. These data are derived from the phase component of the complex radar signal. The use of SAR interferometry can be traced back to the 1960s when the American military used an airborne system for mapping the Darien province in Panama at a scale of 1:250000 by means of radar interferometry. The first published results using this information source for the observation of the surface of the Venus and the Moon are given by Rogers and Ingalls, 1969 (Gens, 1998).

Graham (1974) introduced this synthetic aperture radar (SAR) technique for topographic mapping. He showed that SAR interferometry, with side-looking airborne geometry, could be used to create topographic maps for two reasons:

a. The resolution of some SAR data is adequate to identify various features and objects of the terrain.
b. In addition to this, a sufficient number of points can be measured using the interferometric geometry to describe a terrain surface in detail.

Gabriel and Goldstein (1988) extended the interferometric technique by adapting the existing technique to crossed orbits using interferometric repeat-pass data from the SIR-B mission inclined by an angle of 1.2 degrees.

The technique of differential interferometry was introduced by Gabriel et al. (1989). With two interferograms derived from three different SEASAT observations a double-difference interferogram was calculated. It was assumed that differential interferometry could detect small elevation changes in the order of 1cm or even less (Gabriel et al. 1989).

Since the launch of ERS-1 in July 1991, a large number of interferometric data sets acquired in C-band have become available. The ERS-1 satellite was the first operational spaceborne system, which acquired radar data suitable for SAR interferometry on a routine basis. With these data sets it was possible to investigate the potentials and limitations of SAR interferometry. With the availability of data sets from ERS-2 launched in April 1995, the ESA could set up the tandem mission, which combined data sets from ERS-1 and ERS-2 acquired only one day apart. An initial testing of ERS tandem data quality for InSAR applications was performed by Solaas et al. (1996). The tandem data sets enabled more detailed investigations on the optimal performance of spaceborne systems in terms of temporal decorrelation and atmospheric effects.

1.2.2 Present researches on InSAR

At present, the research on InSAR is in the ascendant and attracting more and more attentions from researchers. Many researches have been done with various methods and many are still in progress to reduce the effects of error sources on the quality of InSAR data. Atmospheric effects are assumed to be one of the error sources of differential interferometry. A homogeneous atmosphere affects the entire image. Such an effect depends on the incidence angle as well as on the baseline. These atmospheric effects can be removed by adequate processing. The refraction causes pixel misregistration. The heterogeneous atmospheric effects are difficult to detect. These effects are caused by tropospheric turbulences and variations in the water vapour content in time and space. A method for the reduction of the effect of atmospheric noise is the averaging of interferometric measurements from independent image pairs (Zebker et al., 1997). Another method is to model the atmosphere based on many parameters to improve the quality of SAR data. A method of stochastic simulation has been proposed to model the atmospheric effect on InSAR measurements based on sample data, resulting in a 37.44% reduction in the standard deviation of the atmospheric errors (Li and Ding, 2003).

Temporal decorrelation is one of the major constraints on repeat-pass interferometry. It is caused by all the physical changes occurring on the terrain surface between two epochs of data acquisitions. In order to get more accurate and reliable results of earth surface deformation, uniform error models are proposed by Liu (2003). The correlation of a desert area may remain unchanged whereas forestry terrain might show a significant loss of coherence with time. More detailed investigations on temporal decorrelation and atmospheric effects have been conducted with ERS tandem data by Solaas et al. (1996).

Baseline decorrelation is a factor of the viewing geometry, which is determined by the orbit chosen for the data acquisition. With an increasing length of the baseline, the noise level increases which leads to a decorrelation of the radar signals. The baseline decorrelation is always in the system and cannot be avoided. It can be reduced to a certain extent at the expense of image resolution. A method to estimate baseline using ground points with heights and their interferometric phase was proposed by Kimura and Todo (1997). In differential interferometry, the baseline can be determined from a given interferogram based on existing DEM (Singh et al., 1997).

A multi-baseline study by Li and Goldstein (1990) presented an error model for topographic mapping. They demonstrated that interferometric data regularly acquired by a spaceborne SAR could provide extremely useful topographic information. This study also showed that the sensitivity of the height measurements increased with the length of the baseline. At the same time, the phase error also increased.

A lot of researches have been carried out to reduce the errors that are caused by interferometric processing. The InSAR processing consists of co-registration, interferogram generation, phase unwrapping and geocoding. Researches have been done in co-registration (Wey, 1991; Lin et al., 1992; Zebker et al., 1994b; Guarnieri and Prati, 1997), generation of interferogram (Bamler and Just, 1993), phase unwrapping (Lim et al., 1997; Ainsworth and Lee, 1998; Bamler et al., 1998; Bao et al., 1998), and geocoding (Wivell et al., 1992).

The co-registration of SAR complex images is the first step in interferometric processing and it is one of the most important processing procedures involved in InSAR. For the quality of the final products, accurate co-registration of the two input images is a prerequisite. Based on a good image registration, ideally up to 1/10 of a pixel, interferometric products with reliable quality could be achieved.

The SAR image co-registration chain consists of two steps: i.e., coarse co-registration and fine co-registration. The fine co-registration is an important step, which includes selection of tiepoints, tiepoint matching, transformation models and resampling method. The distribution and the window size of tiepoints for image co-registration will greatly affect the final generation of SAR image co-registration. Some work has been done on these aspects (Wan, 1990; Weydahl, 1991; Lin et al., 1992; Zebker et al., 1994b; Guarnieri and Prati, 1997).

An automatic approach with multi-step image matching algorithm was used by Liao (2000). In the first step, some interesting tiepoints have been selected by an operator in a grid form in the master image. The grid size is 9*9. The tiepoint matching was carried out based on a normalized correction coefficient. A set of window sizes during tiepoint matching is adopted to do experiments. Good results of InSAR image processing are obtained based on the window size, 63*63. Therefore, it was selected as the optimum window size for tiepoint matching. The next step based on relaxation technique is used to ensure the reliability. At last, least-squares adjustment is carried out to improve the accuracy of co-registration.

Another method for image co-registration in the Fourier domain, using Fast Fourier Transform (FFT), is performed (Adbelfattah and Nicolas, 2004). Indeed, this method works very fast. However, it is just suitable for the stationary regions. For non-stationary regions, the result is unreliable.

There are three kinds of issues in image co-registration. The first is the selection of tiepoint that includes two factors: the distribution of tiepoints; and the number of tiepoint to be selected. For the distribution of tiepoints, theoretically, more tiepoints will result in a more reliable registration. It has been stated in many literatures that tiepoints with features should be selected and evenly distributed over the whole image. However, too many tiepoints would result in a dramatic increase in calculation but it does not necessarily result in a more reliable co-registration. The tiepoints with common features such as a house or an island do not always exist in SAR images. Therefore, tiepoints are usually selected in a grid form, i.e. at grid nodes. The grid size of tiepoints, 2*10, 9*9, 6*6 and 8*8 have been adopted by Zebker et al. (1994b), Wan (1990), Yang and Wang (1999) and Liu et al. (2001), respectively. At present, the selection of tiepoints is determined almost by experiences.

The second is the tiepoint matching that includes two factors: the window size, and the method for matching. Generally, the method for tiepoint matching is based on the maximum cross-correlation. The size of window is a very important factor to be considered. Too large a window size would result in not only a dramatic calculation but also the appearance of pseudo-tiepoint. However, too small a window size would make the co-registration unreliable. A multi-window sized 21*21pixels based on maximum cross-correlation is developed by Li and Fan (2001). The window size, 33*33 pixels, 9*9 pixels and 63*63 pixels have been adopted by Zebker et al. (1994b), Weydahl (1991) and Liao (2000). However, no theory has been developed to guide the selection of window size.

The third is the mathematical models for transformations. The models include geometric transformation models, and radiometric transformation models for resampling. The transformation models can affect the reliability of co-registration.

The reliability of co-registration is a very important consideration for SAR image processing. So far, the root mean square error (RMSE) of the residuals at tiepoints after least-squares adjustment is adopted as a measure for the reliability of co-registration. It implies that the smaller the RMSE, the better or more reliable the co-registration. However, it is not always the case. Therefore, a more effective indicator should be used to measure the reliability of co-registration.

All in all, in order to improve the accuracy of co-registration of SAR image in InSAR, these problems need to be addressed.

1.3 Research Objectives

In the project, the master images are acquired on March 18, 1996; and the slave images are acquired on March 19, 1996. The time interval of acquisition of SAR images is just one day, and the local incidence is the same common factor for all images. So the incidence is not considered here.

Co-registration is the first and one of the most important steps in the interferometric processing. In this step, as previous description, the distribution of tiepoints, the size of window, and the mathematical models can affect the quality of the co-registration. The quality of the co-registration determines the quality of any InSAR products, and thus on the quality of final InSAR product, e.g. DEM. Therefore, the distribution of tiepoints and the size of window are considered in the study. However, the mathematical models are not considered. A reliable measure for the quality of interferogram is necessary in the study, so it is also considered. Therefore, this study aims to improve the accuracy of SAR image co-registration to generate an accurate DEM. The research objectives are as follows:

- to analyze the effects of interval of tiepoint on the reliability of co-registration;
- to determine the optimum window size for tiepoint matching;
- to develop a new method for extracting feature points for co-registration; and
- to develop a reliable quantitative measure for the quality of interferogram.

1.4 Structure of the dissertation

This dissertation consists of eight chapters. After this introductory chapter, the theoretical principle of DEM generation by SAR interferometry is described in chapter 2. In this chapter, firstly, the principle of InSAR is described and the acquisition of SAR image is introduced. Then, procedures for DEM generation (e.g. co-registration, interferogram generation, phase unwrapping and geocoding) are described. Especially, the principle and the procedure of image co-registration are discussed in detail, and factors influencing the reliability of co-registration are examined.

A new quantitative measure for the quality of interferogram is described in chapter 3. At the same time, existing measures for the quality of interferogram are reviewed. The details of the new approach are described. Experimental tests, both direct and indirect, are conducted and reported.

Chapter 4 focuses on the effects of interval of tiepoints on the reliability of SAR image co-registration. A systematic experimental investigation into this issue has been reported.

Chapter 5 investigates the determination of optimum window size for tiepoint matching. The line of thought for the investigation is firstly presented. Then, a new method based on multiresolution wavelet analysis is described. This method is also intensively tested.

A new method for extraction of feature points based on wavelet for co-registration is described in chapter 6. A comparison of test results between the traditional methods and the new method is given.

Chapter 7 describes an automated system for SAR image co-registration. The concept and procedure of the automated system is presented. An automated operators employed this automated system are described in detail.

Chapter 8 presents a summary and some conclusions of the work done in this project. Some recommendations for future research are also given.

Chapter 2

Generation of DEM by InSAR

This chapter introduces the procedures for generating a DEM by InSAR in detail to serve as a theoretical background of discussions to be conducted in future chapters.

2.1 Generation of DEM by InSAR: Overview

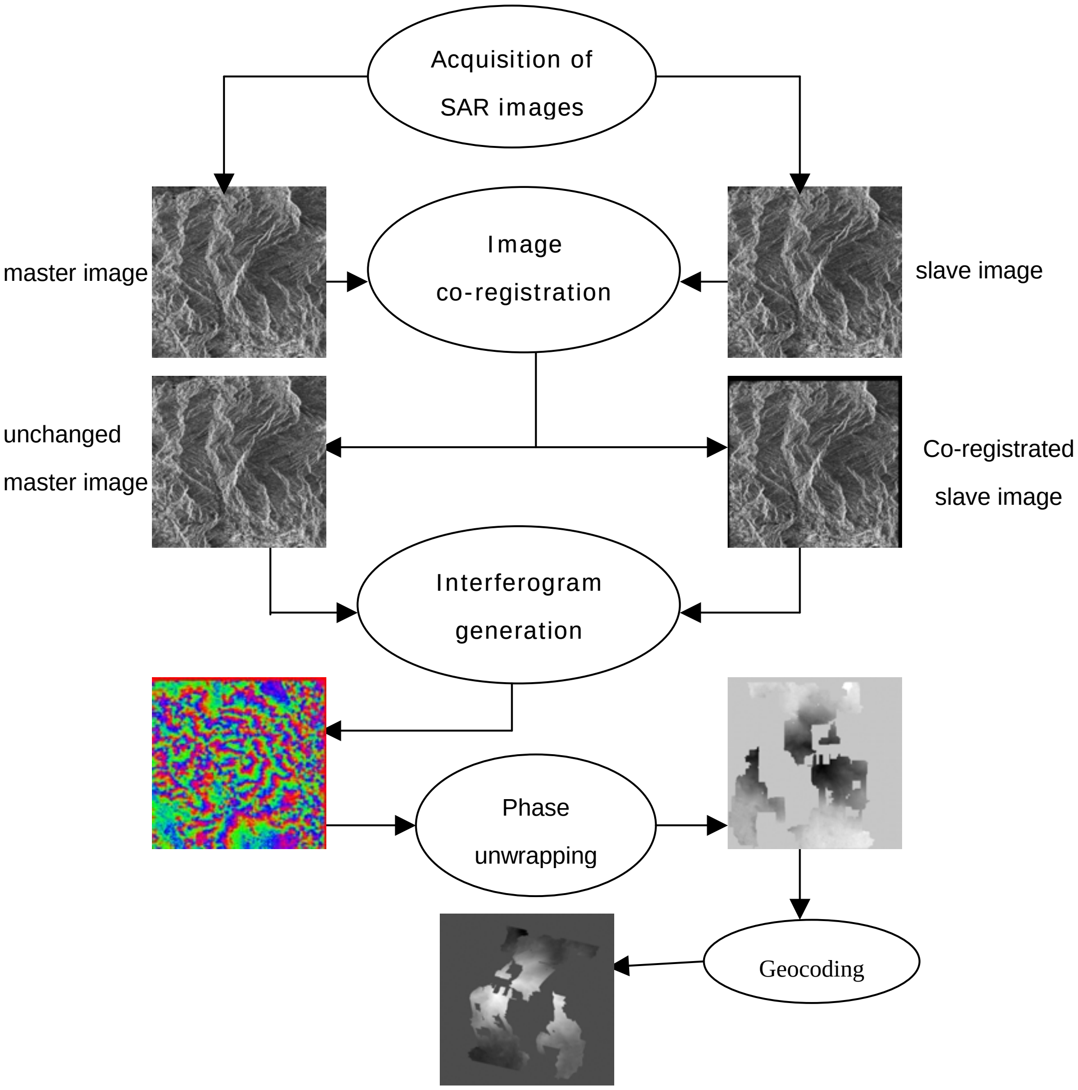

Fig 2.1 Procedures for DEM generation by InSAR

There are five steps in the procedures for generating a DEM. They can be summarized in Fig.2.1, i.e.

1. Acquisition of SAR images;
2. Co-registration of two SAR images;
3. Generation of interferogram;
4. Phase unwrapping of the wrapped interferometric phase;
5. Geocoding of DEM.

Then, we will introduce the details of a DEM's generation step by step from next section on.

2.2 Acquisition of SAR images

From the Fig.2.1, it is seen that the first step is to acquire two SAR images. Normally, there are three ways to acquire SAR images according to the number of antenna mounted on platform and the orientation of the formed baseline (Gens, 1998; Rosen et al., 1996). They are repeat-pass, across-track and along-track, respectively.

In order to understand the principle of acquiring the SAR images, the general InSAR imaging geometry is illustrated in Fig.2.2. Two antennas s_1 and s_2 on ideally parallel flight paths are separated by a baseline B. The slant range from antenna s_1 to an illuminated point on the ground is r_1; r_2 is the slant range from antenna s_2 to the same point. With the looking angle θ, the angle of baseline with respect to horizontal line α and the flying height H, the imaging geometry of InSAR is fixed.

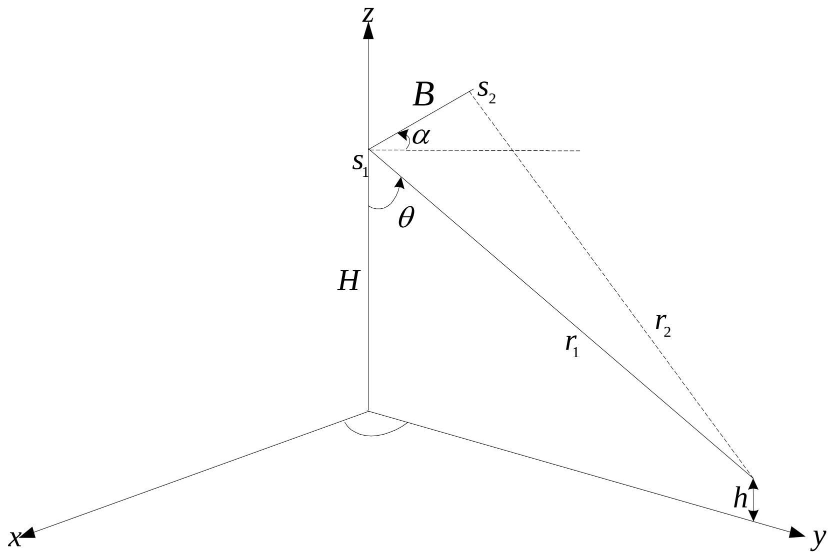

Fig. 2.2 Imaging geometry of SAR interferometry

2.2.1 Acquiring SAR images by Repeat-pass

The term “repeat-pass” means to pass the same area repeatedly. In this approach, only one antenna is used and the SAR system acquires SAR data sets by passing the same area twice, covering it with a slightly different viewing geometry. The imaging geometry of repeat-pass SAR interferometry is illustrated in Fig.2.3. From the figure, it is noticed that, on the first pass, the radar wave is transmitted from antenna s_1, and after interaction with the terrain, the backscattered return is also recorded by antenna s_1. The signal is then processed to a complex SAR image, so does s_2 on the second pass. The signal is processed to another complex SAR image. These SAR images are respectively called the master image and the slave image, as shown in Fig.2.1.

This approach is most suited to spaceborne systems. This is because precise location of the flight path is required, and satellites typically have much more precise and stable orbital paths in the absence of the atmosphere than aircrafts.

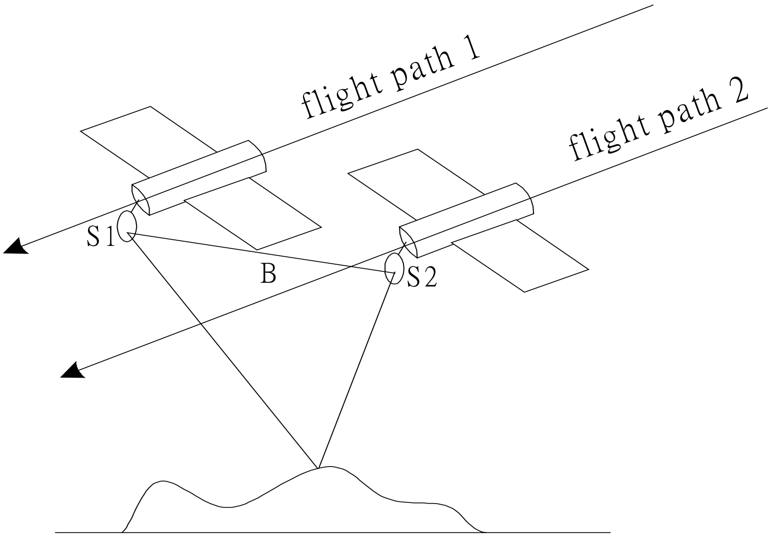

Fig. 2.3 Imaging geometry of repeat-pass SAR interferometry

The repeat-pass approach for airborne SAR was studied by Gray and Farris-Manning (1993). The suitability of interferometric airborne data sets depends on a non-changing terrain backscatter, a stable viewing geometry and phase-preserved information of the motion-compensated signal. The compensation of non-linear motions of the two antennae is essential for achieving accurate interferometric results from airborne data. Stevens et al. (1995) have given an overview of the work done in this field. Optimal motion compensation requires a precise knowledge of the relative geometry of the radar and each illuminated target. The motion compensation can be implemented in different ways (Gray et al., 1992). One of the ways is to implement the motion compensation for each antenna separately through the definition of two reference tracks. Madsen et al. (1993) estimated the two antenna positions performing a resampling in the motion compensation stage using measurements from a digital avionics data system, a global position system (GPS) and an inertial navigation system (INS).

Normally, the repeat-pass approach is adopted to obtain SAR images to generate a DEM. In this study, all of SAR interferometry data are ERS-1/2 data that are obtained by repeat-pass approach.

2.2.2 Acquiring SAR images by Across-track

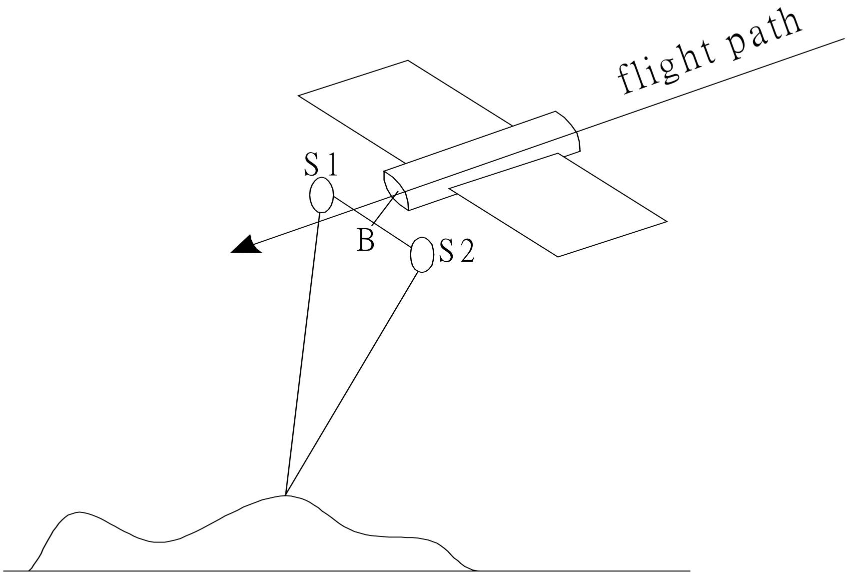

Fig. 2.4 Imaging geometry of across-track SAR interferometry

Another approach to acquire SAR images is by across-track. Its imaging geometry is illustrated in Fig.2.4. In this approach, two SAR antennae, s_1 and s_2, are mounted on the same platform. The SAR data are acquired at the same time and the baseline, B, is perpendicular to the flight path. The system, therefore, records the master image and the slave image at the same time but from two slightly different locations.

The main problem with the geometry of the across-track approach in the airborne configuration due to errors caused by the aircraft roll cannot be distinguished from the influence of the terrain slope. This problem is less critical in the spaceborne case, as a satellite track is more stable than an airborne flight path.

2.2.3 Acquiring SAR images by Along-track

The along-track means to acquire SAR images by two SAR antennae, s_1 and s_2. The two antennae follow each other at a short distance on the same orbit and possibly on the same platform for SAR data acquisition. The baseline, B, is parallel to the flight direction. Its imaging geometry is illustrated in Fig.2.5. At present, the along-track approach is only applicable to airborne SAR systems, as it requires two antennae on the same platform. The along-track approach is sensitive to movement of the scatters in the range direction. It can be used to measure Earth-surface velocities. As such, this technique holds promise for the detection of slowly moving ground targets. It was developed in mapping ocean currents. Above sea, it produces a map of the current velocity component parallel to the radar look direction. Now the master image and the slave image are recorded from the same position but at slightly different times. Therefore, the phase differences between the corresponding signals are caused by the movement of the measured object, e.g. water current. The moving surface leads to a Doppler shift according to the phase velocity of the water waves. All stationary targets are not visible whereas the moving ones can be seen in the radar imagery.

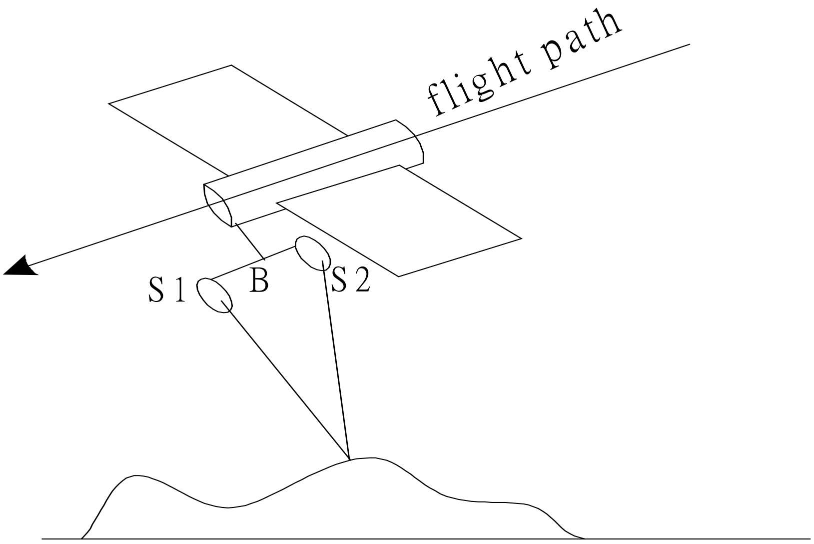

Fig. 2.5 Imaging geometry of along-track SAR interferometry

The quality of interferometric measurements depends on the relative distance of the antenna(s), the so-called base line. Across-track and along-track are only possible using airborne systems with two antennas. The yaw and pitch cause baseline components in y- and z-direction produce additional phase differences. The base line can, therefore, be readily found to the required precision. In principle, repeat-pass way is also possible for aircraft, but the flight track and the aircraft attitude should be known with sufficient accuracy.

2.3 Co-registration of SAR image

2.3.1 Principle of co-registration

From the Fig.2.1, it can be seen that once the master image and the slave image are obtained, the co-registration of two SAR images is needed. Since two complex images are taken at the same scene but at different times, their orientations could be different. Geometrically, they are in different coordinate systems. Therefore, there is a need of a transformation to bring them down to identical coordinate systems. There are two solutions, i.e. either to bring both down to absolute ground coordinate or to fit one image to the coordinate systems of the other. Normally, co-registration refers to the latter.

The co-registration consists of two steps: the coarse co-registration and fine co-registration. The coarse co-registration means the master image and the slave image are registered to the accuracy of one pixel. The fine co-registration means these two images are registered to the accuracy of sub-pixel based on the coarse co-registration. Based on the orbital state data, the moments and the centers of the image, the coarse co-registration of two images, master and slave images are carried out.

Once the coarse co-registration is determined, the fine co-registration can be performed. In order to bring slave image to fit into the coordinate system of the master's, the relationship between these two images needs to be established. In InSAR practice, some sorts of polynomials are used as approximate models for the transformation between them. Once a model is selected, the next step is to solve the coefficients of the model (polynomial). In this case, a set of reference points (so-called tiepoint – the corresponding points on both images) needs to be selected. Due to the lack of well-defined points on images, the normal practice is to select a set of tiepoints in a grid form from master image. Then a matching process is employed to find the points on the slave image, which are the corresponding positions of the grid nodes on the master image. The cross-correlation coefficient is a parameter widely used for the evaluation of the matching results. The principle is: a window of, say, 3x3, pixels on the master image is selected with the given point to be matched at the center; this window is to be matched. Correspondingly, a window as the same size one in master image is selected in the slave image. This window shifts along the row and column direction in the slave image. There is a cross-correlation coefficient between the two windows. Since the window in the slave image shifts, there are many matching of windows of the same size, but the one matching with the highest cross-correlation coefficient is regarded as the true matching. The central pixels of the two windows are regarded as the corresponding pixels to be found. After this, using transform model, the slave image can be fitted into the coordinate system of master image. Afterwards, the slave image is resampled and the registered slave image can be obtained. Till this, image co-registration has been finished. The sequence of SAR image co-registration is shown in Fig.2.6.

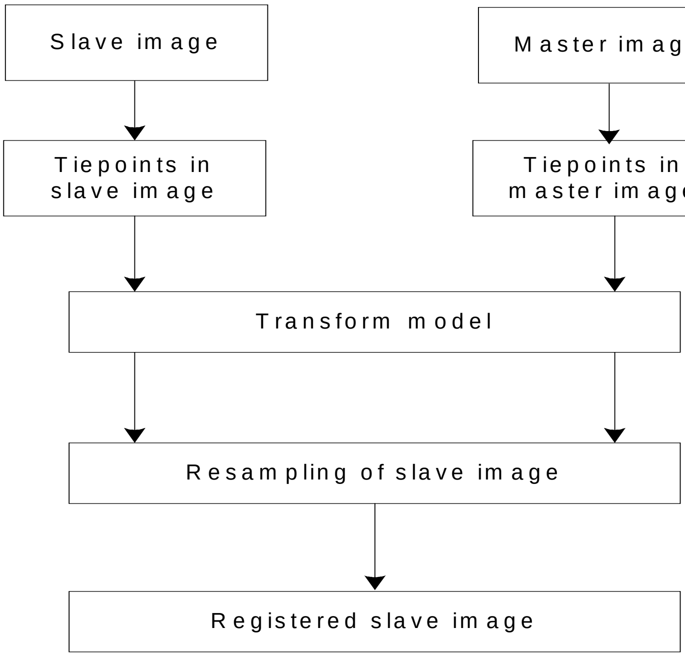

Fig 2.6 Sequence of SAR image co-registration

2.3.2 Tiepoint matching

In the co-registration, tiepoints matching is implemented by using the strategy of image cross-correlation maximization. Let $z_1(m,n)$ and $z_2(m,n)$ represent the two SAR complex images, the master image and the slave image, respectively:

$$z_1(m,n) = |z_1(m,n)| e^{j\varphi_1(m,n)} \quad (2.1a)$$

$$z_2(m,n) = |z_2(m,n)| e^{j\varphi_2(m,n)} \quad (2.1b)$$

where $m = 0,1,2,\cdots,M-1$, $n = 0,1,2\cdots,N-1$, the image size is $M \times N$, $\varphi_1(m,n)$ and $\varphi_2(m,n)$ are the phase values.

The cross-correlation coefficient γ is expressed as:

$$\gamma = \frac{\left|E(z_1 z_2^*)\right|^2}{\sqrt{E(\left|z_1\right|^2)E(\left|z_2\right|^2)}} \tag{2.2}$$

The expanded form of Equation (2.2) can be written as:

$$\gamma(m,n) = \frac{\left|\sum_{l=-(L-1)/2}^{(L-1)/2}\sum_{k=-(K-1)/2}^{(K-1)/2} z_1(m+l,n+k)z_2^*(m+l,n+k)e^{-j\varphi(m+l,n+k)}\right|}{\sqrt{\sum_{l=-(L-1)/2}^{(L-1)/2}\sum_{k=-(K-1)/2}^{(K-1)/2}\left|z_1(m+l,n+k)\right|^2 \sum_{l=-(L-1)/2}^{(L-1)/2}\sum_{k=-(K-1)/2}^{(K-1)/2}\left|z_2(m+l,n+k)\right|^2}} \tag{2.3}$$

where $L \times K$ is the image patch size, $\varphi(m,n)$ is the phase difference between two images. It can be imagined that the computation would be heavy due to the involvement of φ. In order to reduce the calculation, an alternative solution has been in use, i.e. to use the power correlation coefficient $\hat{\rho}$ (Guarnieri and Prati, 1997). The computation of $\hat{\rho}$ is shown as:

$$\hat{\rho}\ (m,n) = \frac{\left|\sum_{l=-(L-1)/2}^{(L-1)/2}\sum_{k=-(K-1)/2}^{(K-1)/2}\left|z_1(m+l,n+k)\right|^2\left|z_2(m+l,n+k)\right|^2\right|}{\sqrt{\sum_{l=-(L-1)/2}^{(L-1)/2}\sum_{k=-(K-1)/2}^{(K-1)/2}\left|z_1(m+l,n+k)\right|^4 \cdot \sum_{l=-(L-1)/2}^{(L-1)/2}\sum_{k=-(K-1)/2}^{(K-1)/2}\left|z_2(m+l,n+k)\right|^4}} \tag{2.4}$$

The relation between $\hat{\gamma}$ and $\hat{\rho}$ is as follows:

$$\hat{\gamma} = \begin{cases} \sqrt{2\hat{\rho} - 1} & \hat{\rho} \rangle 0.5 \\ 0 & \hat{\rho} \le 0.5 \end{cases} \tag{2.5}$$

The one matching with the maximum cross-correlation coefficient means the central pixels of the two windows are homologous.

Another tiepoints matching method based on spectral maximization is proposed by Gabriel and Goldstein (1988). The method multiplies one window of the master image by the complex conjugate of the corresponding window in the slave image. For registered windows this product is essentially a constant amplitude and linear phase term: its FT is then rather peaked. Misalignments broaden the spectrum around the peak.

2.3.3 Transformation model

In order to enhance the accuracy of the results, different transformation models could be adopted in different situations. In the case of a photograph, one frame of an image is taken at one time. For each frame, there are six orientation elements (three rotation and three translation). The elements are the same for all image pixels on the same frame. If the image coordinate system is that the origin being the center of the image and the x-axis being along the flight direction, an arbitrary Cartesian coordinate system could possibly be used in the image plane. It is as follows (Li, 2001):

$$x = \frac{A_1 X + A_2 Y + A_3 Z + A_4}{A_9 X + A_{10} Y + A_{11} Z + 1} \tag{2.6a}$$

$$y = \frac{A_5 X + A_6 Y + A_7 Z + A_8}{A_9 X + A_{10} Y + A_{11} Z + 1} \tag{2.6b}$$

where, $A_1 \sim A_{11}$ are the coefficients; x and y are the coordinates of an image point; X, Y and Z are the coordinates of its position on the ground.

In the case of scanner images, image pixels are acquired scan by scan. A frame of an image may consist of thousands of scan line. In this case, there are six orientation elements and there is a need of at least three control points for the computation of coefficients for each scan line. This is not feasible. The problem could be simplified if the relationship among the scan lines is known. However, this is normally not the situation. In this case, a single polynomial could be used to approximate the geometric model transformation for all scan lines (Li, 2001):

$$x = a_0 + a_1 X + a_2 Y + a_3 X^2 + a_4 Y^2 + a_5 XY + \cdots \tag{2.7a}$$

$$y = b_0 + b_1 X + b_2 Y + b_3 X^2 + b_4 Y^2 + b_5 XY + \cdots \tag{2.7b}$$

where, $a_0 \sim a_5$ and $b_0 \sim b_5$ are the coefficients; x and y are the coordinates of an image point; X and Y are the coordinates of its position on the ground. Indeed, in this case, the errors caused by distortions are re-distributed rather than removed by the polynomial function.

The latter case is suitable for InSAR practice. Normally, the bicubic function is used as the polynomial for the transformation between master image and slave image. In InSAR image co-registration, (x, y) is the pixel's coordinate in the slave image while (X, Y) is the pixel's coordinate in the master image.

After co-registration, the master image remains unchanged while the slave image is registered, as shown in Fig.2.1.

2.4 Generation of interferogram

Once co-registration has been carried out, the interferogram can then be generated. SAR raw imagery data records not only the amplitude but also the phase information determined by the distance between the target and the radar antenna. The phase measured in each image is the difference on a pixel basis. A SAR interferogram is produced using the phase differences between the relevant pixels of two SAR images of the same scene taken from repeat orbits at nearly the same positions in space. Its processes consist of three steps as follows:

- formation of a rough interferogram with flat-earth phase trend;
- removal of flat-earth phase trend using precise orbit data; and
- filtering of the interferogram.

After these processes, an enhanced interferogram could be obtained. In this dissertation, InSAR interferogram refers to the enhanced interferogram.

2.4.1 Formation of a rough interferogram

The formation of a rough interferogram is carried out by extracting the phase difference, which is implemented via the product between the master image and the complex conjugate of the registered (slave) image. The interferometric phase is computed from the following equation:

$$\varphi = ph[z_1(m,n) * z_3^*(m,n)] = \frac{4\pi}{\lambda}(r_1 - r_2) \tag{2.8}$$

where r_1 and r_2 are slant ranges from point on the ground to the radar at two times. λ is the wavelength. $z_1(m,n)$ and $z_3(m,n)$ represent the two SAR complex images, master image and the registered (slave) image, respectively. The resultant interferogram contains interferometric phases. However, flat-earth phase trend and noise are still included in the interferogram. Therefore, the next step is referred to as phase flattening where the interferogram phase component due to a flat-earth phase trend is removed. To remove the flat-earth phase trend facilitates interpretation of the topography in the interferogram phase and reduces phase wrapping complexity.

2.4.2 Removal of flat-earth phase trend using precise orbit data

Assuming a surface without topographic relief, the interferometric phase could be expressed as follows (Rosen et al., 1996):

$$\varphi_0 = \frac{4\pi}{\lambda} B \cdot \sin(\theta - \alpha) \tag{2.9}$$

where α is the orientation angle of the baseline and θ is the looking angle. If relief is present, the looking angle will differ from θ by $\delta\theta$,

$$\varphi = \frac{4\pi}{\lambda} B \cdot \sin(\theta + \delta\theta - \alpha) \tag{2.10}$$

Combining equations (2.9) and (2.10), the flattened phase is (Rosen et al., 1996):

$$\varphi_{flattened} = \varphi - \varphi_0 \approx \frac{4\pi}{\lambda} \frac{B^{\perp}}{R\sin\theta} h + \frac{4\pi}{\lambda} \Delta r \tag{2.11}$$

where, R is the slant range from point on the ground to radar; Δr is the ground deformation along the direction of radar line-of-sight between the two SAR acquisitions.

Theoretically, every pixel corresponds to a certain orbit data and baseline data. So flat-earth phase included in every pixel phase could be removed by the method, pixel by pixel, after every orbit data and baseline data that correspond to every pixel have been obtained. However, too many pixels would result in a dramatic increase in calculation but does not necessarily result in better phase flattening. It is noticed that the earth is considered as an ellipsoid, which results in the flat-earth phase trend. The trend is systematic, so the whole flat-earth phase trend could be systematically removed by modeling with some pixels that have been suitably selected in the whole SAR image.

When comparing the flattened interferogram with the amplitude image, a correlation between the fringe pattern and the region’s topography will be apparent. The residual phase after flattening is directly proportional to terrain height so the residual interferogram looks much like a contour map of terrain height.

It is noticed that the term of baseline, B in equation (2.11), will greatly influence the precision of the flattened phase. Precise orbit determination and baseline estimation have attracted a lot of research. The errors of orbit and baseline are caused by many complex factors, such as systematical factor and random factors. The baseline error always exists in the system and cannot be avoided (Zebker et al., 1996). It can be reduced to a certain extent at the expense of image resolution (Gatelli et al., 1994). For ERS-1/2, precise orbit determination is based on tracking data, a gravity model, and several dynamical models (Hanssen, 2000).

2.4.3 Filtering of the interferogram

Filtering of the SAR data sets can be applied at different stages of the InSAR processing. Each filtering step can reduce disturbing effects such as speckle or noise that is in the SAR data, at the expense of losing a part of the original information. After the generation of the flattened interferogram, the interferogram must be filtered to enhance its quality. For example, a low-pass filter was applied by Schwabish (1995) while an adaptive filter has been proposed by Goldstein and Werner (1998).

The InSAR interferogram contains several types of information (Ge et al., 2002):

- topographic, a contour-like pattern representing the topography of the area;

- geometric pattern, a systematic striped pattern caused by differences between the two SAR sensor trajectories; and
- differential pattern, fringes associated with any change of the range between the two SAR imaging, the sources of which include ground displacement, change of atmospheric refraction, and phase change by reflection due to growth of vegetation.

After these steps, an enhanced interferogram is obtained as shown in Fig.2.1, the color image.

2.5 Phase unwrapping

An interferogram contains phase information directly related to the topography. Since this information is given modulo 2π, there is an ambiguity problem in calculating the correct integer number of phase cycles that needs to be added to each measurement in order to obtain the correct slant range distance (Gens, 1998). This ambiguity solution is referred to as phase unwrapping. It is one of the focuses in InSAR research.

The absolute interferometric phase may be related directly to the topographic height and amount of deformation. However, the measured interferometric phase represents the absolute interferometric phase modulo 2π. To go from the measured phase to the absolute phase, a two-step process is required: phase unwrapping and absolute phase determination. The relation between the measured interferometric phase $\varphi_{measured}$, the unwrapped interferometric phase $\varphi_{unwrapped}$, and the absolute interferometric phase

$\varphi_{absolute}$ may be summarized as follows:

$$\varphi_{measured} = \mathrm{mod}(\varphi_{absolute}, 2\pi) \tag{2.12}$$

$$\varphi_{unwrapped} = (\varphi_{measured})_{unw} = \varphi_{absolute} + 2\pi n \tag{2.13}$$

$$\varphi_{absolute} = \frac{4\pi}{\lambda}\delta P \tag{2.14}$$

where n is an integer, δP represents the one-way path length difference due to topography and deformation, and $(\bullet)_{unw}$ represents the phase unwrapping process.

2.6 Geocoding of DEM

After the phase unwrapping, algebra and geometry yield the following equations for height:

$$\sin(\theta - \alpha) = \frac{r_1^2 - r_2^2 + B^2}{2r_1B} \approx \frac{-\lambda\varphi_{unwrapped}}{2\pi B} \tag{2.15}$$

$$\theta = \alpha - \arcsin\left[\frac{\lambda\varphi_{unwrapped}}{4\pi B}\right] \tag{2.16}$$

$$h = H - r_1 \cos\theta \tag{2.17}$$

where, H is the antenna s_1 height above the reference plane and h is the target height. r_1 and r_2 are the slant ranges from antennae to the point on the ground, respectively. θ is the looking angle. α is the angle of baseline with respect to horizontal line. $\varphi_{unwrapped}$ is the unwrapped interferometric phase. B is the baseline. Therefore, the DEM data can be derived from radar interferogram. But this DEM data are not goecoded yet as shown in Fig.2.1.

Normally, the DEM is provided in a coordinate system related to SAR geometric configuration. The geocoded DEM is the last product. Geocoding of a DEM includes two steps. The first step is referred to a coordinate transformation of the radar coordinates (range/azimuth/height) to coordinates in a convenient geodetic reference system such as WGS84 (Φ, Λ, H), where Φ and Λ are for the geographic latitude and longitude, respectively, and H is for height above the reference body (ellipsoid). The second step is the projection onto a cartographic map, usually the Universal Transverse Mercator (UTM). In this operation, each point (Φ, Λ) over the ellipsoid is projected onto a cylindrical surface, which is wound up and provides northern (y) and eastern (x) coordinates. The projection formulas are (Davis et al., 1981):

$$\begin{aligned} x = K_0 \Big[& N\,\Lambda' \cos\Phi + \frac{N}{6}\cos^3\Phi(1 - t^2 + \eta^2)\,\Lambda'^3 \\ & + \frac{N}{120}\cos^5\Phi(5 - 18t^2 + t^4 + 14\eta^2 - 58\eta^2 t^2)\Lambda'^5 + \cdots \Big] \end{aligned} \tag{2.18a}$$

$$\begin{aligned} y = K_0 \Big[& S_\Phi + \frac{N}{2}\sin\Phi\cos\Phi\cdot\Lambda'^2 \\ & + \frac{N}{24}\sin\Phi\cos^3\Phi\cdot(5 - t^2 + 9\eta^2 + 4\eta^4)\cdot\Lambda'^4 + \cdots \Big] \end{aligned} \tag{2.18b}$$

where, N is the radius of the sphere;

$t = \tan\Phi$;

$\eta^2 = \frac{\varepsilon^2 \cos^2\Phi}{1-\varepsilon^2}$, $\varepsilon = 0.0067686580$;

$\Lambda' = \Lambda - \Lambda_0$ =longitude difference from central meridian, Λ_0 in radians;

S_Φ =length of the meridian arc from the equator to latitude Λ;

$K_0 = 0.9996$.

This projection is in zones that are 6^o wide. The reference ellipsoid is Clarke 1866 in North America. The details of the projection can be referred to Davis et al. (1981), Maling (1992) and Frankich (1993).

Chapter 3

A quantitative measure for the quality of interferogram based on phase differences

In last chapter, the theoretical background of generation of a DEM is described. From that, it can be noticed the generation of interferogram is a critical process. This chapter aims to develop a reliable measure for the quality of InSAR interferogram.

3.1 Existing measures for the quality of interferogram

At present, there are several measures for the quality of interferogram. From literature, it can be found that visual appearance of the fringes is widely used to indicate the quality of interferogram (eg Eldhuset et al., 1996; Zou et al., 2002). That is, clear fringes mean good quality of an interferogram. In other words, if the interferometric fringes can be observed clearly, the quality of interferogram must be good. On the opposite, the blurry fringes will be found in bad interferogram as shown in Fig.3.1. The fringes in Fig.3.1.b are clearer than fringes in Fig.3.1.a. It means the quality of the interferogram in Fig.3.1.b is better than the one in Fig.3.1.a. Visual inspection is one type of manual interpretation.

One type of indicator reflecting the quality of interferogram is the RMS error (RMSE) of tiepoints. It is a pre-assumption that the RMSE of the residuals at tiepoints after least-squares adjustment is a good indicator for the quality. It implies that the smaller the RMSE, the better the quality of interferogram. However, it is not always the case. In some cases, when the RMSE is small, the resultant interferogram could not be good as identified visually as shown in Fig.3.1. For Fig.3.1.a interferogram, its RMSE is 0.0151 smaller than the one in Fig.3.1.b. However, the quality of the interferogram in Fig.3.1.b is obviously better than the one in Fig.3.1.a. It is an unreliable indicator for the quality of interferogram by RMSE.

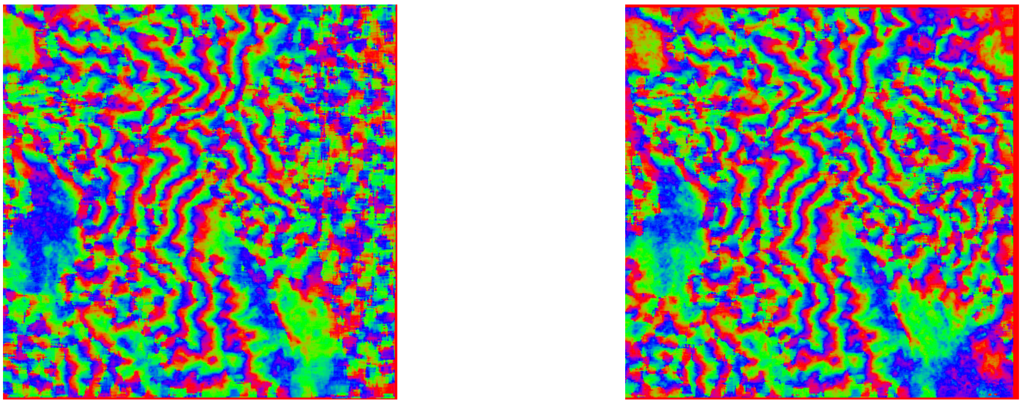

a. RMSE: 0.0151

b. RMSE: 0.0210

Fig.3.1 Identification of quality of interferogram visually

The coherence of interferometric SAR is another indicator for the quality of interferogram (Guarnieri and Prati, 1997; Gens, 1998). The coherence, varying in the range of 0 to 1, is a pixel basis as the correlation coefficient between two SAR images. It reflects the accuracy of phase in interferogram. The degree of coherence can, therefore, be used as a quality measure for the interferogram, the higher the coherence, the better the quality. The coherence of an image varies from area to area or even from pixel to pixel. Therefore, coherence image is produced to show the quality variation of an interferogram over the entire area. Fig.3.2 is a coherence image. In this image, some areas are brighter while some areas are darker. The brighter areas correspond to good coherence and the dark areas correspond to bad coherence.

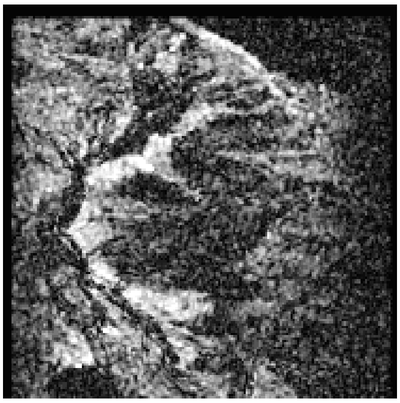

Fig.3.2 A coherence image

To make a coherence measure quantitative, histogram of the coherence image is used (Fig.3.3). More precisely, the mean of the distribution and the standard deviation (STD) from the mean are the two quantitative parameters for the coherence. Fig.3.3 shows three examples of such histograms and the corresponding coherence images. In Fig.3.3a, the mean is 0.4746 while its standard deviation (STD) is 0.2005. The corresponding coherence image is shown in Fig.3.3d. In Fig.3.3b, the mean is 0.4786 while its STD is 0.2012. The corresponding coherence image is shown in Fig.3.3e. In Fig.3.3c, the mean is 0.4759 while its STD is 0.2007. The corresponding coherence image is shown in Fig.3.3f. It can be easily observed that the coherence images are quite different and the distributions of pixel number in different interval of coherence are quite different among these three cases but the actual values for the means and

STD are quite similar. Therefore, such statistical parameters are not sufficient to differentiate the quality of interferograms.

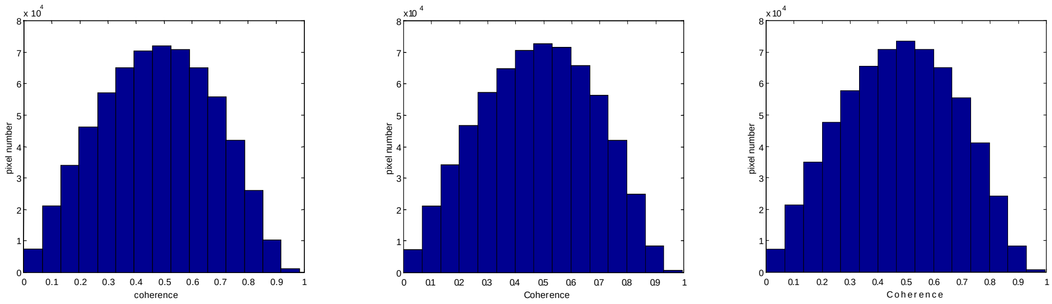

(a) (b) (c)

mean: 0.4746; STD: 0.2005 mean: 0.4786; STD: 0.2012 mean: 0.4759; STD: 0.2007

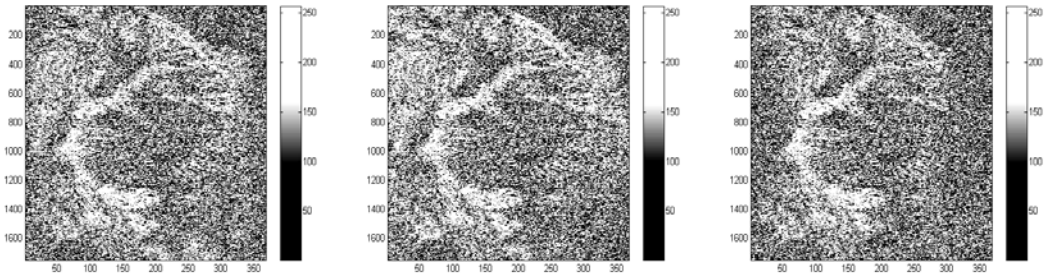

(d) (e) (f)

Fig.3.3 Histogram of coherence and corresponding coherence image

(d) a coherence image corresponding to histogram (a)

(e) a coherence image corresponding to histogram (b)

(f) a coherence image corresponding to histogram (c)

It seems that there are no better quantitative measures available for the quality of interferograms thus far. Therefore, a more robust measure is a matter of some urgency. This chapter aims to present such a measure for InSAR interferogram.

3.2 A quantitative measure based on the sum of phase differences

3.2.1 The line of thought

In chapter 2, the generation of interferogram is described in detail. From the processes for the generation of interferogram, it is noticed that the interferogram is generated via the product between the master image and the complex conjugate of the registered (slave) image. That is, the interferogram contains interferometric phase. In other words, the information contained in the interferogram is expressed only by phase and an interferogram is a type of phase image, which represents a two-dimensional relative phase signal -- the 2π-modulus of the (unknown) absolute phase signal. Technically, in the interferogram, the absolute phase is wrapped to a [0, 2π] interval. Every pixel of the interferogram corresponds to a phase value and is represented by a color.

There might be many different (color) fringes that express different phase values in the interferogram. The phase value changes gradually from 0 radian to 2π radian. One kind of color fringe indicates a phase value that is in the [0, 2π] interval. For example, green fringe may indicate about 2-radian phase and blue fringe indicates about 4.5-radian phase. The color of fringes gradually changes from red to green, green to blue and blue to red. Actually, this situation is the reflection of the phase variation which changes from 0-2 radian, 2-4.5 radian and 4.5-2π radian. The phase difference between two pixels that are in neighboring fringes should, therefore, be very small.

Ideally, the phase difference should be an infinitesimal value. If the two pixels are in the same color fringe, the phase difference between them should be zero.

There are eight pixels around any given pixel (central pixel). Totally, there are eight phase differences between the central and the neighboring pixels. The sum of the eight phase differences should be an infinitesimal value in ideal situation. In such case, the sum of the phase difference (SPD) in the whole interferogram is usually zero.

In practice, even if the two pixels are in neighboring fringes, their phase difference may not be an infinitesimal value because of noise. This happens in some part of the interferogram. In such a situation, the phase difference between two neighboring pixels may be bigger and thus the sum of the phase difference between the central and its neighbouring pixels may be much bigger than zero. As a result, the SPD of the whole interferogram is likely to be bigger than zero.

From such an observation, it can be imagined that the sum of the phase difference (SPD) could be a good quantitative measure for the quality of interferograms. The smaller the SPD, the better the interferogram quality.

3.2.2 Computational considerations

For every pixel, there is a SPD. For the whole interferogram, the SPD could be obtained by summarizing the SPD of all pixels. This seems to be a straightforward computation. However, a special case should be considered. That is, when the phase value changes from 2π-0 radian, the two pixels' phase difference is not an infinitesimal value but 2π radian instead. In such a case, the variation of fringes/phases is actually continuous and the phase difference value should be converted to zero.

For one pixel, its SPD_{local} could be calculated as follows:

$$SPD_{local}(x,y)=\sum_{l=-1}^{1}\sum_{k=-1}^{1}\left|\varphi_{flattened}(x,y)-\varphi_{flattened}(x+l,y+k)\right| \qquad (3.1)$$

where x =0, 1, 2, …, p-1; y =0, 1, 2, …, q-1, and the interferogram image size is p×q.

For the whole interferogram, the SPD could be calculated as follows:

$$SPD=\sum_{x=0}^{p-1}\sum_{y=0}^{q-1}SPD_{local}(x,y) \qquad (3.2)$$

It will be found later that the SPD values computed from Eq.(3.1) and Eq.(3.2) will be very big because some phase differences are repeatedly computed and added together. This only affects the absolute value but relatively it is still valid. Another way is to take average in Eq.(3.3) as follows:

$$APD_{local}(x,y)=\frac{1}{8}\times\sum_{l=-1}^{1}\sum_{k=-1}^{1}\left|\varphi_{flattened}(x,y)-\varphi_{flattened}(x+l,y+k)\right| \qquad (3.3a)$$

$$SPD_{whole}=\sum_{x=0}^{p-1}\sum_{y=0}^{q-1}APD_{local}(x,y) \qquad (3.3b)$$

In fact, instead of the absolute value of the phase differences, the square of phase differences is also a good alternative.

3.3 Experimental evaluation

3.3.1 Design of the simulation test

To test the adequacy of SPD as a quantitative measure for the quality of interferogram, a series of tests should be conducted. However, as discussed previously, there are too many factors influencing the quality of interferograms, and it is difficult to isolate so many factors in experimental tests. It is then decided to conduct a set of simulation.

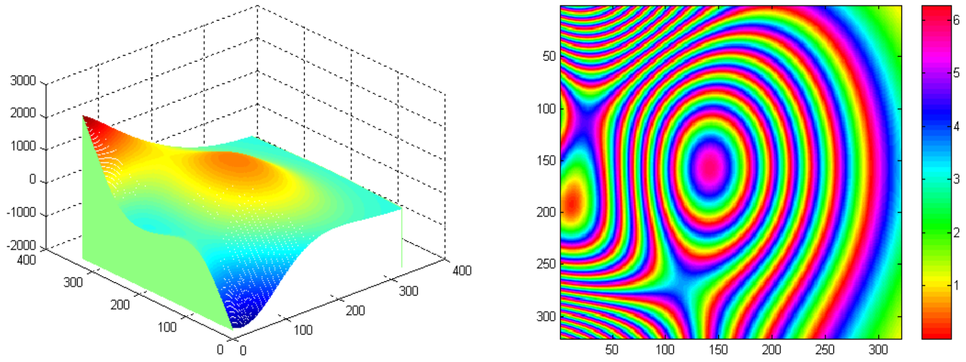

(a) Simulated DEM (b) The corresponding interferogram

Fig.3.4 Simulated DEM and the corresponding interferogram

First of all, a DEM is simulated for the test area, as shown in Fig.3.4. The size of DEM is 320m×320m. The height range is from –2000-2000 meters. The topographic variation could be observed clearly from Fig.3.4a. With the heights obtained from DEM, the flattened phase could be derived by Eq.(2.14), as shown in Fig.3.4b. Therefore, an interferogram can be simulated for this area.

It is a natural line of thought that one could add noise of different levels to the interferogram to deteriorate quality of interferogram to different degree to see whether the proposed measure is capable of differentiating the quality. Alternatively, one may add noises to the DEM instead of the interferogram. The former is a direct approach and the latter is an indirect approach. In this study both approaches are tested.

3.3.2 An indirect test

In the first test, the noise is added to DEM before the generation of interferogram. The resultant interferograms are shown in Fig.3.5a-h. The level of noise added to the DEM is listed in Table 3.1. The SPD for each of these interferograms are also listed in Table 3.1.

In the right, near to the interferogram, there is a color bar that represents phase value by different colors. The color varies from red to blue, blue to red. Correspondingly, the phase values vary from 0 - 3.14 radian, 3.14 - 6.28 radian.

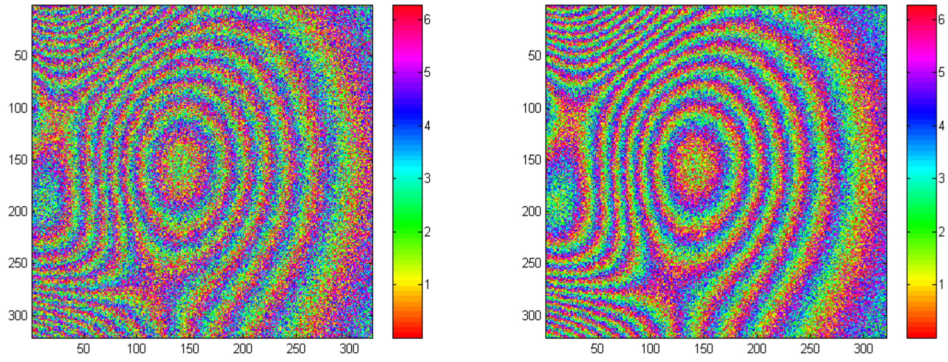

(a) (b)

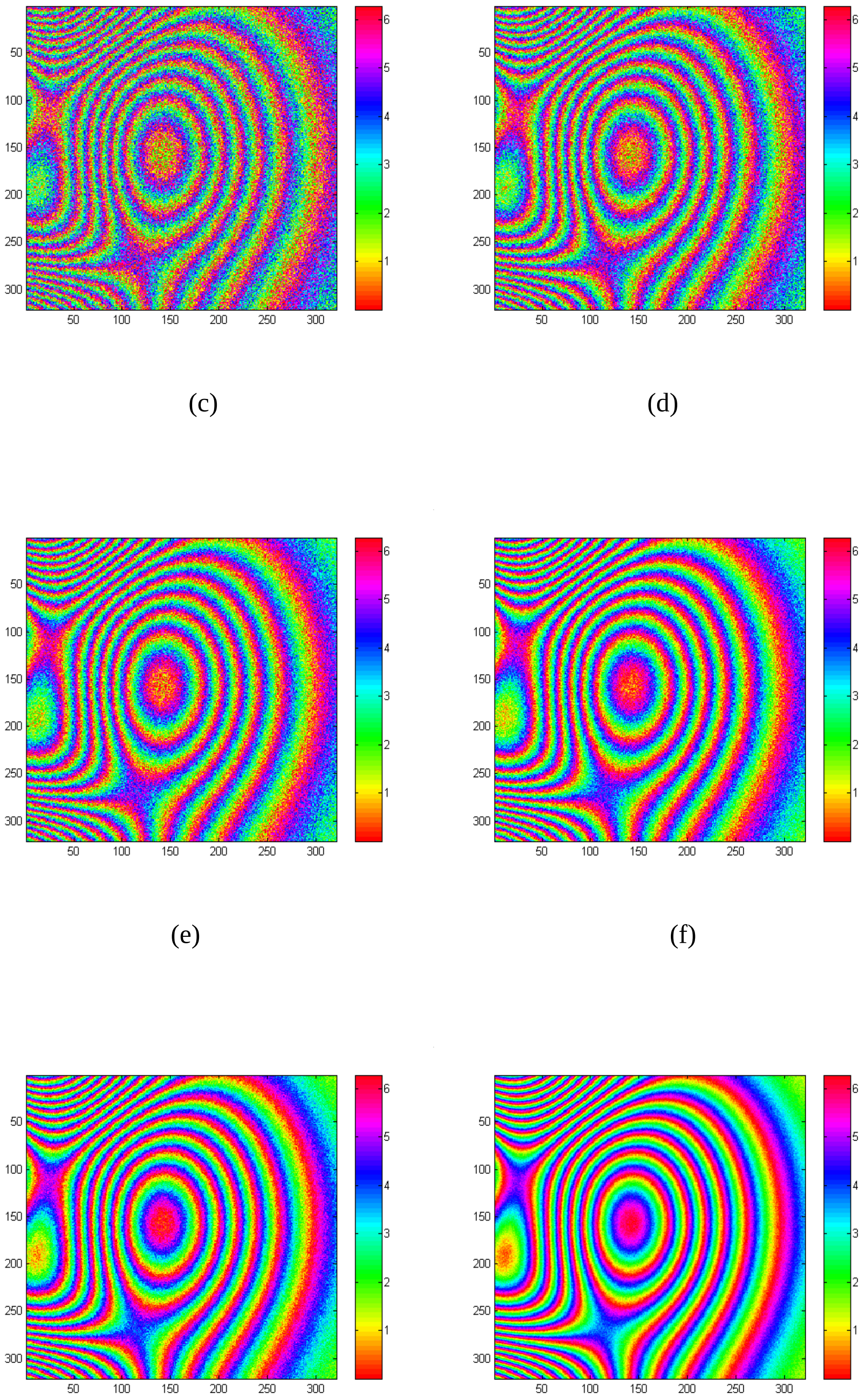

(c) (d)

(e) (f)

(g) (h)

Fig.3.5 Interferograms of the indirect test

Table 3.1: Noise levels for and SPD from the first test

Interferogram	Level of noise (Amplitude: meter)	SPD (radian)
Fig.3.5.a	160	1,585,900
Fig.3.5.b	140	1,497,300
Fig.3.5.c	120	1,368,400
Fig.3.5.d	100	1,217,700
Fig.3.5.e	80	1,035,500
Fig.3.5.f	60	835,580
Fig.3.5.g	40	629,900
Fig.3.5.h	20	436,970

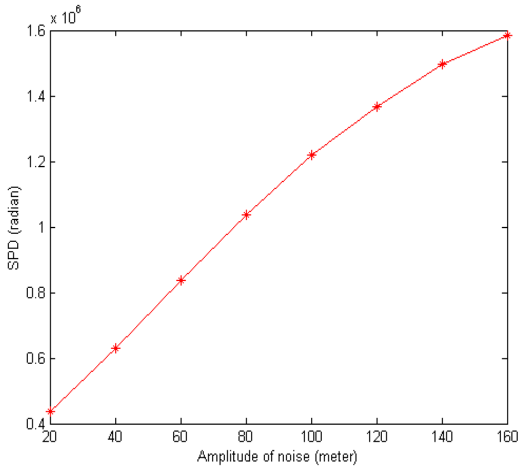

Fig.3.6 Relationship between the SPD and the level of noise added to DEM

For Fig.3.5a image, its SPD is 1,585,900. Fringes are very blurry and there is much noise in interferogram. This indicates much discontinuous variation of phase exists in the image. The interferogram is not good at all. From Fig.3.5b to Fig.3.5h, the quality of the interferograms improves as the fringes become clearer Correspondingly, the SPD values become gradually smaller. These SPD values have been plotted and shown in Fig.3.6. In this test, the noise is added to DEM and its amplitude varies from

20, 40, …, to 160 meters. It is clear that the SPD values are becoming bigger with the increasing noise.

3.3.3 A direct test

In order to get reliable results from the new measure, another test has been conducted, i.e. adding noise to the interferogram directly. The levels of noise are exactly the same as those used for the previous test. The test results are included in Fig.3.7 and Table 3.2.

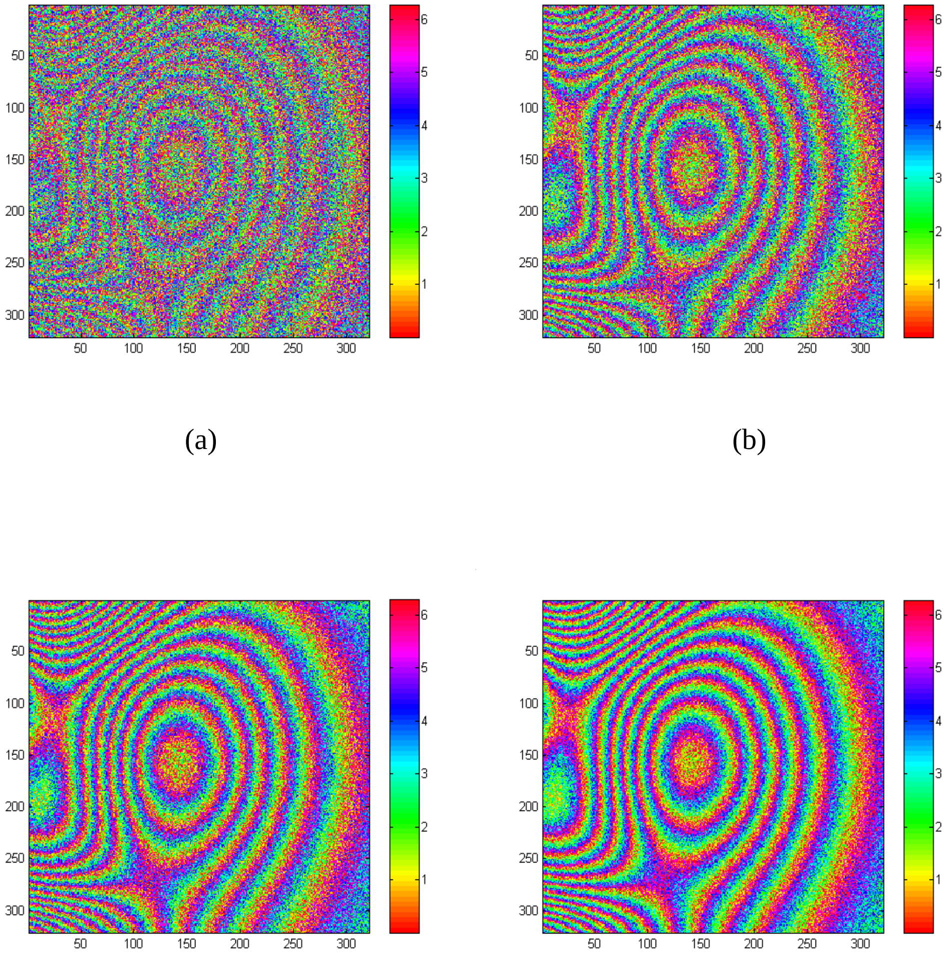

(a) (b)

(c) (d)

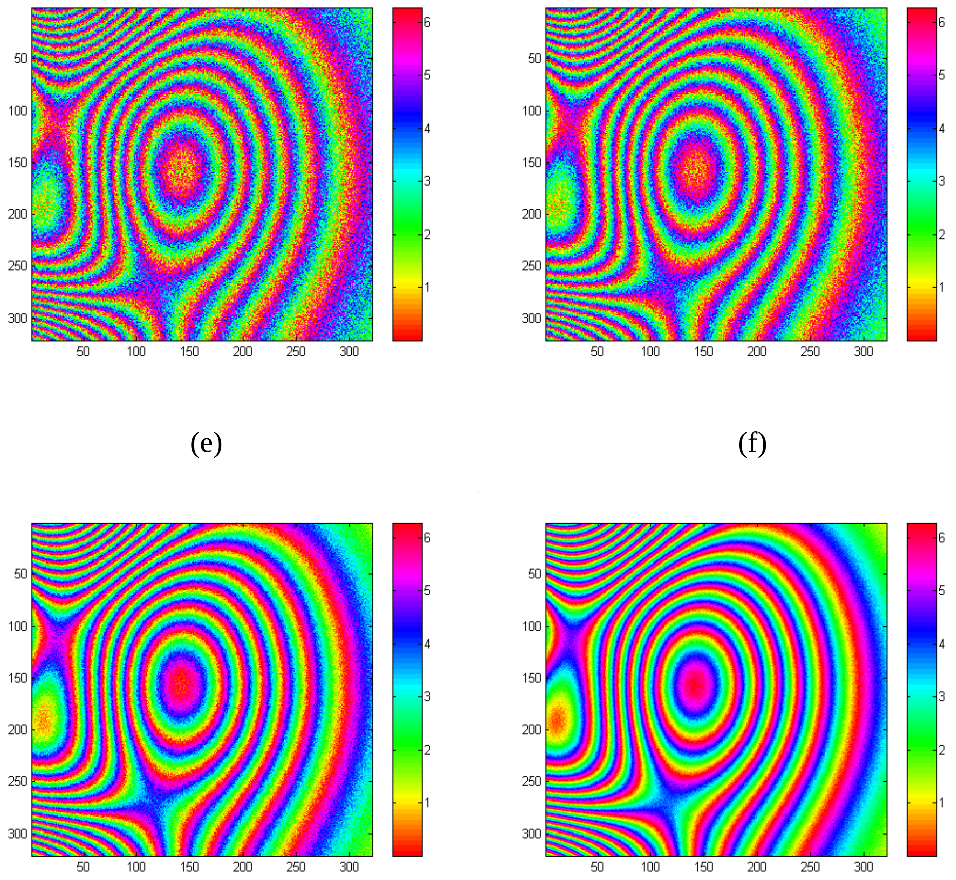

(e) (f)

(g) (h)

Fig.3.7 Interferograms of the direct test

Table 3.2: Noise levels for and SPD from the second test

Interferogram	Level of Noise (Amplitude: radian)	SPD(radian)
Fig.3.7.a	5	1,648,100
Fig.3.7.b	4	1,511,700
Fig.3.7.c	3.5	1,408,800
Fig.3.7.d	3	1,269,600
Fig.3.7.e	2.5	1,122,900
Fig.3.7.f	2	951,820
Fig.3.7.g	1	585,200
Fig.3.7.h	0.5	419,100

For Fig.3.7a image, its SPD is 1,648,100. The fringes are very blurry and the boundary of fringes is very difficult to be distinguished. The whole image is very blurry, and the signal is almost buried by noise. The SPD is very big and thus the resultant interferogram is very bad. From Fig.3.7a to Fig.3.7h, the interferogram varies from blurry to clear, clear to very clear. The boundary of fringes becomes gradually clearer. The corresponding SPDs become gradually smaller. It means the quality of interferograms gradually improves. The trend is shown in Fig.3.8. In this test, the noise is added to interferogram and its amplitude varies from 0.5, 1, …, to 5 radian. It is clear the SPD values are becoming bigger with the increasing noise.

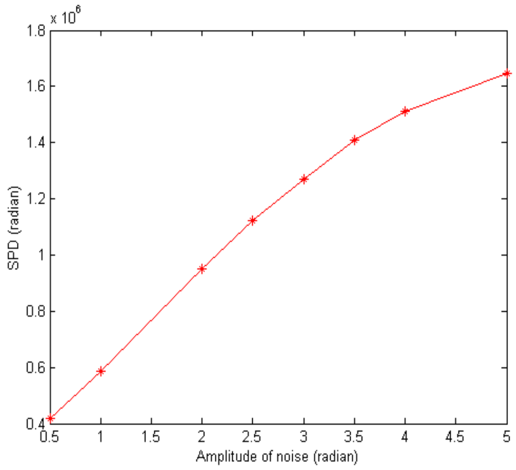

Fig.3.8 Relationship between the SPD and the level of noise added to the interferograms

3.4 Comparison of different indicators for the quality of the interferograms

As introduced in section 3.1, the mean of coherence is a measure for the quality of interferogram. In this section, a further analysis of the comparison between the SPD and the mean of coherence will be given. The three interferograms and their corresponding histograms of coherence images are shown in Fig.3.9.

The SPD_b is smaller than the SPD_a by 1680 radians. The percentage difference between Fig3.9.a and Fig3.9.b is 1.61%. The percentage difference is the ratio between the difference of two SPDs and the smaller SPD (here is SPD_b). The SPD_b is smaller than the SPD_c by 520 radians. The percentage difference between Fig3.9.b and Fig3.9.c is 0.5%. The SPD_c is smaller than the SPD_a by 1160 radians. The percentage difference between Fig3.9.a and Fig3.9.c is 1.1%.

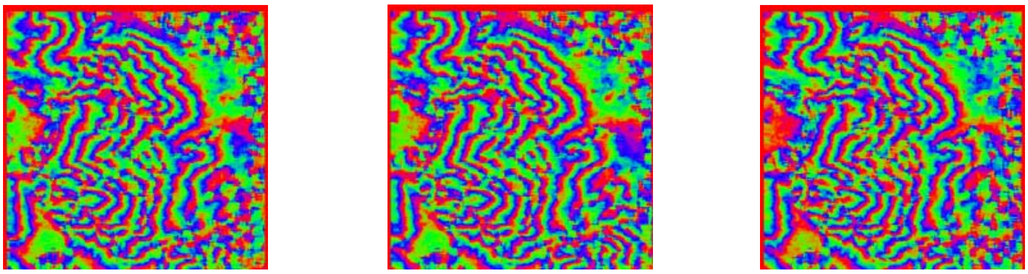

SPD_a : 106,140 (a)　SPD_b : 104,460 (b)　SPD_c : 104,980 (c)

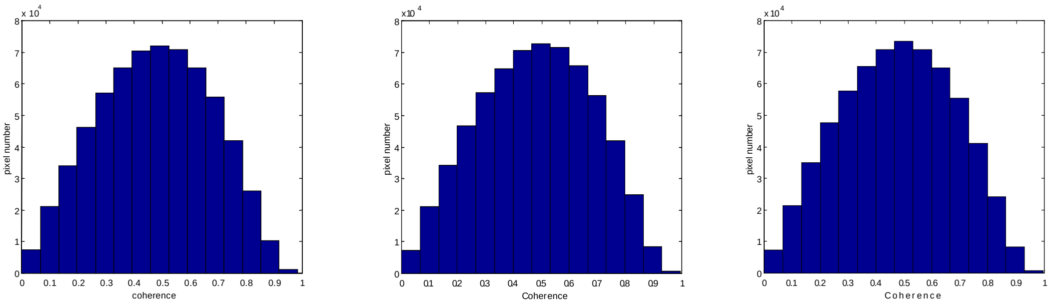

$Mean_d$: 0.4746 (d)　$Mean_e$: 0.4786 (e)　$Mean_f$: 0.4759 (f)

Fig.3.9 Comparison of different indicators

The $Mean_d$ is smaller than $Mean_e$ by 0.0040. The percentage change of the “mean of coherence” between Fig.3.9.d and Fig.3.9.e is 0.84%. The $Mean_f$ is smaller than

$Mean_e$ by 0.0027. The percentage change of the “mean of coherence” between Fig.3.9.e and Fig.3.9.f is 0.57%. The $Mean_d$ is smaller than $Mean_f$ by 0.0013. The percentage change of the “mean of coherence” between Fig.3.9.d and Fig.3.9.f is 0.27%.

Obviously, although all of the percentage change is small, all of the percentage difference of SPD is bigger than the one of “mean of coherence”. So, the SPD is a more effective quantitative measure for the quality of interferogram.

3.5 Summary

This chapter presents a quantitative measure for the quality of interferograms in InSAR. First of all, an examination of existing measures is given. Based on the evaluation results and an analysis of the characteristics of interferograms, a new measure is proposed based on the phase differences in the interferogram, i.e. the sum of phase differences (SPD).

In order to prove the efficacy of SPD as a quantitative measure for the quality of interferograms, two tests have been conducted. In the first test, noise is added to DEM while in the second test, noise is directly added to interferogram. Noise with eight different levels is used, resulting in eight interferograms for each test. By visual inspection, it can be found easily that the quality of interferograms is poorer with higher level of noise. From these interferograms, the SPD values are computed accordingly. Results show that the SPD values become smaller when the interferogram looks better. This also corresponds to a lower noise level. In other words, the SPD values reflect the quality of interferograms very well.

Additionally, a further analysis of the percentage difference of the SPD and the “mean of coherence” is carried out. The percentage difference of SPD is bigger than that of the “mean of coherence”. Therefore, the SPD is a more effective quantitative measure for the quality of interferogram.

From the test results and the analysis, it is found that the variation of the quality of an interferogram could be appropriately reflected by the SPD value of the interferogram. Therefore, it can be concluded that the SPD measure is a reliable measure of the quality of InSAR interferograms.

Chapter 4

Effects of tiepoint interval on the reliability of co-registration

In SAR image co-registration, one of the factors that affects the quality or reliability of the InSAR products is the distribution of tiepoint. Based on the quantitative measure for the quality of interferogram studied in last chapter, this chapter investigates the effects of tiepoint interval on the reliable of co-registration.

4.1 Principle of selecting tiepoints

SAR image co-registration is based on patch match using a set of tiepoints, which are congigate image points on both images. Generally, tiepoints are selected according to the following criteria:

- Distribution of tiepoint;
    a. Regular distribution: grid;
    b. Irregular distribution: feature points;
- Number of tiepoints to be selected.

The distribution of the tiepoints (i.e. configuration, orientation and point density) and accuracy are the parameters that will affect the accuracy of co-registration. As tiepoints are normally selected in a form of grid configuration (due to lack of well-defined points) from image pixels without measurement, the influencing parameters have been reduced to only one -- density, which can then be represented by grid interval. In other words, the interval of tiepoints has great effect on the reliability of SAR image co-registration. The question arising is "how much is the effect?"

This concerns a situation of lacking of feature points. But, if there are feature points that can be selected from image for co-registration, it will be another situation to be discussed in more details in Chapter 6.

4.2 Design of the experimental test

4.2.1 Benchmarks for the test

The products of SAR interferometric processing could be an intermediate (e.g. the interferogram) or final product (e.g. the DEM). The reliability of co-registration could be measured by the quality of interferogram and the accuracy of DEM. The quality of inteferogram can be quantitatively measured by “sum of phase differences” (SPD), described in Chapter 3.

In order to get a quantitative measurement for DEM accuracy, a suitable accuracy measure needs to be defined. The check-points can be used as an accuracy measure for a DEM. All of the checkpoints are distributed in grid or any other forms. The DEM accuracy is measured by the differences between the heights obtained from

DEM and the heights of check-points. Suppose H_k is the height of check-point and R_k is the height obtained from DEM corresponding to the check-point, then the accuracy of DEM can be expressed by the RMS error δ_{DEM} as follows (Li and Zhu, 2000):

$$\delta_{DEM} = \sqrt{\frac{1}{n}\sum_{k=1}^{n}(R_k - H_k)^2} \tag{4.1}$$

where n is the number of check points.

4.2.2 Data for the test

Four pairs of SAR complex images are used in the test so as to minimize the scene-dependency, which are Por Kai Shan, Ngau Yee Shek Shan, Tai Lam Country Park and Pok To Yan in Hong Kong (No.1 to No.4), shown in Fig. 4.1. The images are obtained by ERS-1/2. The master image is acquired on March 18, 1996; and the slave image is acquired on March 19, 1996. The time interval of acquiring images is just one day, and the local incidence is the common factor for all images. Therefore, the incidence is not considered here. In these images, every pixel represents an area 4m*20m (4m in row and 20m in column). Therefore, in order to get a square area, the ratio of pixel number between row and column should be 5:1. All images are of the same size, i.e. consisting of 1760*400 pixels. All images are nearly a square area.

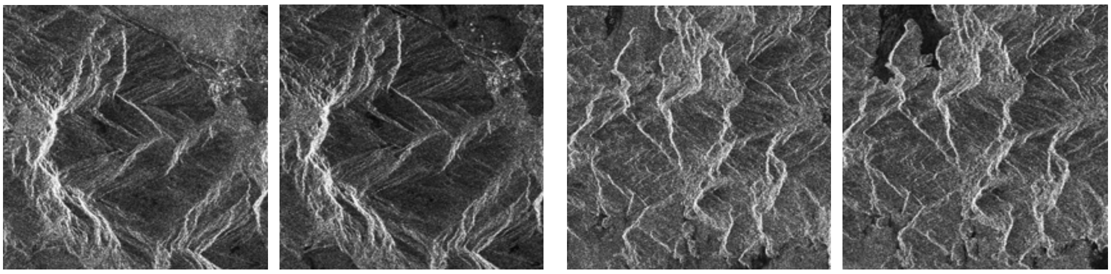

Master image Slave image Master image Slave image

a.The first pair of SAR images (Por Kai Shan) b.The second pair of SAR images (Ngau Yee Shek Shan)

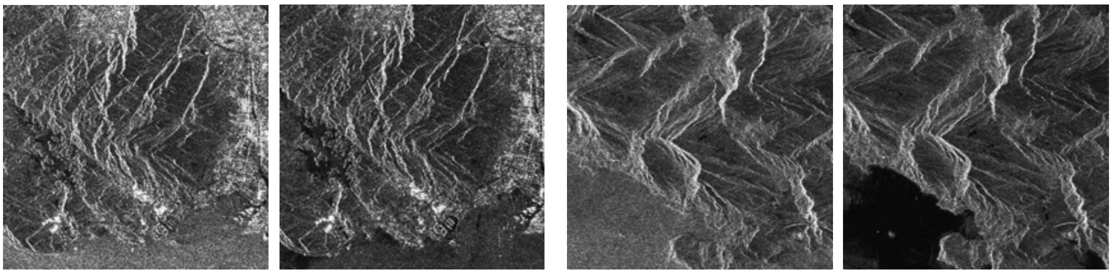

Master image Slave image Master image Slave image

c. The third pair of SAR images (Tai Lam Country Park) d. The forth pair of SAR images (Pok To Yan)

Fig. 4.1 SAR images of four different test areas

For the assessment of DEM accuracy, the use of reference DEMs is still a standard approach since it provides the possibility of comparing the complete DEM with a reference. The accuracy of the reference DEM should be at least one order better than the accuracy of the DEM to be evaluated. Contours are the source for creating reference DEM since they provide necessary morphological details, such as spot heights, to represent the terrain surface. In general, they are derived from existing topographic maps. The more precise contours can be obtained from larger scale topographic map. The accuracy of DEMs derived from contour data, in terms of RMSE or standard deviation, is about 1/3 to 1/5 of the contour interval (Li, 1994). In this study, the topographic map is at 1:5000 and the contour interval is 10 meters. The precision of reference DEMs derived from the contour data is, therefore, about 3 meters. This is sufficient as the reference to evaluate the accuracy of DEMs obtained from repeat-pass InSAR data. Based on the reference DEM, the accuracy of DEM can be calculated by the formula (4.1) described in section 4.2.1.

4.2.3 Strategy for the experiment

Of course, several factors included in co-registration can affect the quality of interferogram and the accuracy of DEM. In this study, other factors are kept unchanged and therefore interval of tiepoints will be considered only. As a result, a series of grids with different intervals are used for the selection of tiepoints so that the relationship between the grid interval and the qualities of products can be analyzed.

The tiepoint grids sizes vary from 4*4, 5*5, … to 9*9. The number of tie points varies from 16 to 81. The corresponding grid interval varies from 411*68 (i.e. 411 pixels in row and 68 pixels in column between two tiepoints) to 182*29. The detailed data information is provided in Table 4.1.

The experiment consists of two tests: one for the effects of tiepoint interval on the quality of interferogram; and the other for the effects of tiepoint interval on the accuracy of DEM. Combining the two tests, the variation of the qualities of the products with the tiepoint interval can be analyzed. A further test was also carried out in order to make the findings more reliable.

4.3 Effects of the tiepoint interval on the quality of interferogram

As discussed previously, the SPD is used to measure the quality of interferogram to analyze the effects of the tiepoint interval. The data of interferograms about the four test areas are included in Table 4.1. The SPD is calculated according to formula (3.3), included in Table 4.2.

Table 4.1 The interferograms of four different test areas

Image size (pixel)	Grid size (pixel)	Tiepoint interval		No.1 Image		No.2 Image		No.3 Image		No.4 Image	
		in row	in colum	RMSE of tiepoints (pixel)	Interfero-gram	RMSE of tiepoints (pixel)	Interfero-gram	RMSE of tiepoints (pixel)	Interfero-gram	RMSE of tiepoints (pixel)	Interfero-gram
1760*400	4*4	411	68	0.0827		0.0892		0.0505		0.0512	
	5*5	328	53	0.0735		0.0708		0.0440		0.0490	
	6*6	273	44	0.0294	Fig 4.2.1.a	0.0443	Fig 4.2.2.a	0.0398	Fig 4.2.3.a	0.0290	Fig 4.2.4.a
	7*7	234	38	0.1442	Fig 4.2.1.b	0.0805	Fig 4.2.2.b	0.0385	Fig 4.2.3.b	0.0481	Fig 4.2.4.b
	8*8	205	34	0.0619	Fig 4.2.1.c	0.0320	Fig 4.2.2.c	0.0212	Fig 4.2.3.c	0.0174	Fig 4.2.4.c
	9*9	182	29	0.0965	Fig 4.2.1.d	0.0664	Fig 4.2.2.d	0.0070	Fig 4.2.3.d	0.0641	Fig 4.2.4.d

Table 4.2 SPD values of different tiepoint intervals

Tiepoint interval		No.1 Image		No.2 Image		No.3 Image		No.4 Image	
in row	in colum	Interfero-gram	SPD (radian)	Interfero-gram	SPD (radian)	Interfero-gram	SPD (radian)	Interfero-gram	SPD (radian)
273	44	Fig 4.2.1.a	104,460	Fig 4.2.2.a	162,060	Fig 4.2.3.a	108,390	Fig 4.2.4.a	126,290
234	38	Fig 4.2.1.b	106,580	Fig 4.2.2.b	150,110	Fig 4.2.3.b	107,110	Fig 4.2.4.b	127,640
205	34	Fig 4.2.1.c	104,980	Fig 4.2.2.c	146,820	Fig 4.2.3.c	106,510	Fig 4.2.4.c	127,510
182	29	Fig 4.2.1.d	106,140	Fig 4.2.2.d	148,210	Fig 4.2.3.d	107,000	Fig 4.2.4.d	129,260

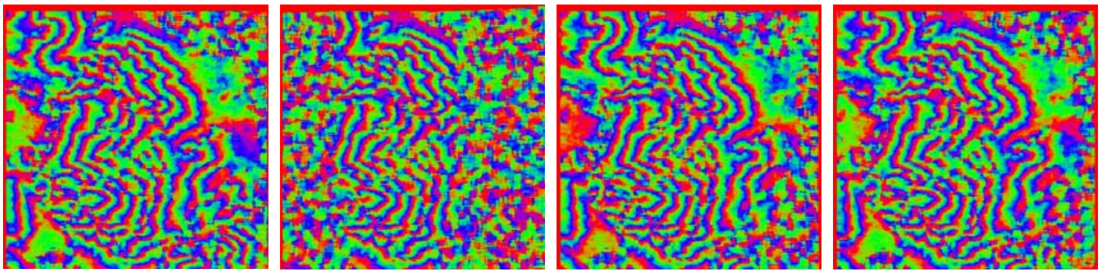

(a) Tiepoint interval: 273*44 (b) Tiepoint interval: 234*38 (c) Tiepoint interval: 205*34 (d) Tiepoint interval: 182*29

Fig. 4.2.1. The interferograms of No.1 image in different tiepoint intervals

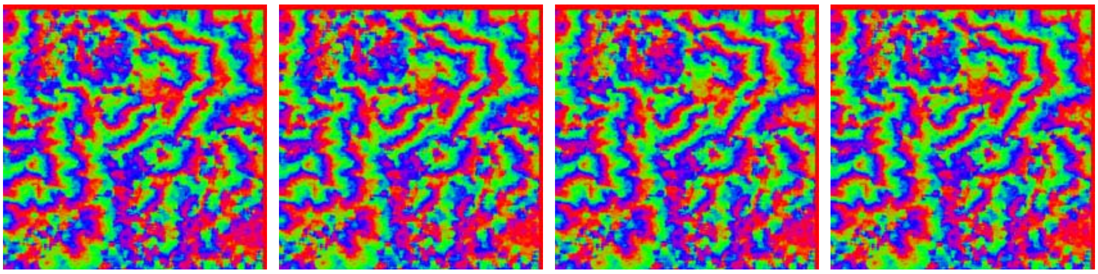

(a) Tiepoint interval: 273*44 (b) Tiepoint interval: 234*38 (c) Tiepoint interval: 205*34 (d) Tiepoint interval: 182*29

Fig. 4.2.2. The interferograms of No.2 image in different tiepoint intervals

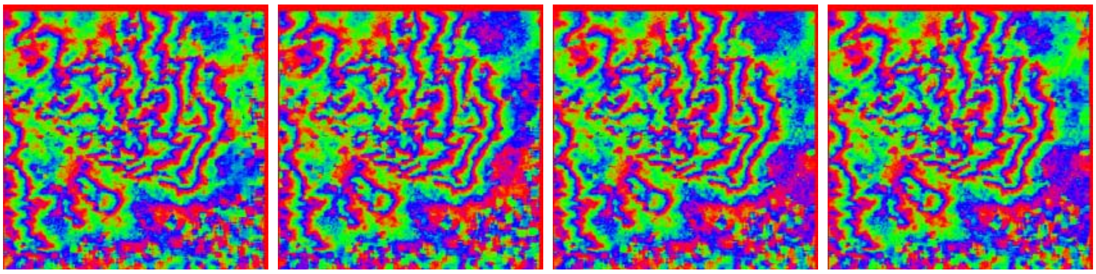

(a) Tiepoint interval: 273*44 (b) Tiepoint interval: 234*38 (c) Tiepoint interval: 205*34 (d) Tiepoint interval: 182*29

Fig. 4.2.3. The interferograms of No.3 image in different tiepoint intervals

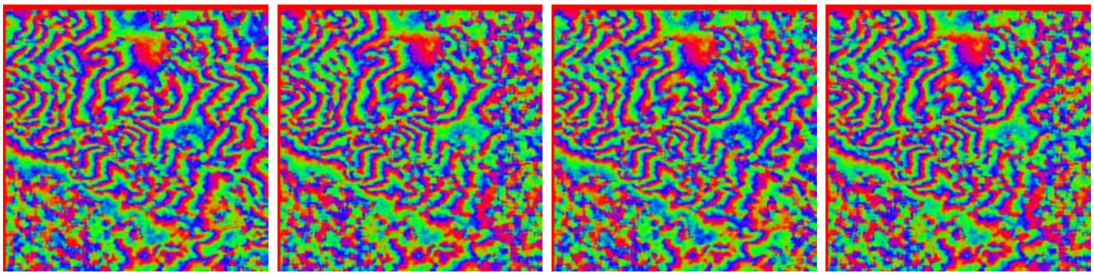

(a) Tiepoint interval: 273*44 (b) Tiepoint interval: 234*38 (c) Tiepoint interval: 205*34 (d) Tiepoint interval: 182*29

Fig. 4.2.4. The interferograms of No.4 image in different tiepoint intervals

Fig. 4.2. The interferograms generated in different tiepoint intervals on four test areas

More precisely, in each test area, not all but only four interferograms are included, one for the best, one next to the best, the third a worse one and the forth the worst one. The corresponding images are given in figures from Fig. 4.2.1 to Fig. 4.2.4. The difference of SPD, η_{SPD}, is analyzed and derived as followers:

$$\eta_{\mathrm{SPD}} = | \mathrm{SPD}_{8*8} - \mathrm{SPD}_{i*i} \; | \; / \; \mathrm{SPD}_{i*i}$$

Where SPD_{8*8} is the SPD of interferogram generated by the grid size 8*8. SPD_{i*i} is the SPD of interferogram generated by the grid size i*i. Therefore, the η_{SPD} between SPD_{8*8} and the biggest SPD is analyzed. Similarly, the η_{SPD} between SPD_{8*8} and the SPD next to the biggest is also analyzed.

For No.1 image, when the tiepoint grid interval is 273*44, the SPD is 104,460, which is the smallest. The resultant interferogram is the best among all. However, when the interval is 234*38, its SPD is 106,580, being the largest. When the interval is 205*34, the SPD is 104,980 next to the smallest. When the interval is 182*29, the SPD is 106,140 large. Relative to interval 234*38 and 182*29, when interval is 205*34, the SPD_{8*8} is smaller than SPD_{7*7} and SPD_{9*9} by 1.5% and 1.1%, respectively.

For No.2 image, when the interval is 273*44, its SPD is 162,060 large, and the resultant interferogram is not good. When the tiepoint interval is 234*38, its SPD is 150,110 large. When the tiepoint interval is 205*34, the SPD is 146,820 the smallest. Its interferogram is the best among all. When the tiepoint interval is 182*29, the SPD is 148,210 next to the smallest. Relative to interval 273*44 and 234*38, when interval is 205*34, the SPD_{8*8} is smaller than SPD_{6*6} and SPD_{7*7} by 9.4% and 2.2%, respectively.

For No.3 image, when the interval is 273*44, its SPD is 108,390 large. When the tiepoint interval is 234*38, the SPD is 107,110, which is also large. When the tiepoint interval is 205*34, the SPD is 106,510 the smallest. Its interferogram is the best. When the tiepoint interval is 182*29, the SPD is 107,000 next to the smallest. Relative to interval 273*44 and 234*38, when interval is 205*34, the SPD_{8*8} is smaller than SPD_{6*6} and SPD_{7*7} by 1.7% and 0.4%, respectively.

For No.4 image, when the interval is 273*44, the SPD is 126,290, the smallest among all. The experimental interferogram is the best. When the tiepoint interval is 234*38, the SPD is 127,640 large. When the tiepoint interval is 205*34, the SPD is 127,510, next to the smallest. When the tiepoint interval is 182*29, the SPD is 129,260 the largest. Relative to interval 234*38 and 182*29, when interval is 205*34, the SPD_{8*8} is smaller than SPD_{7*7} and SPD_{9*9} by 0.1% and 1.4%, respectively.

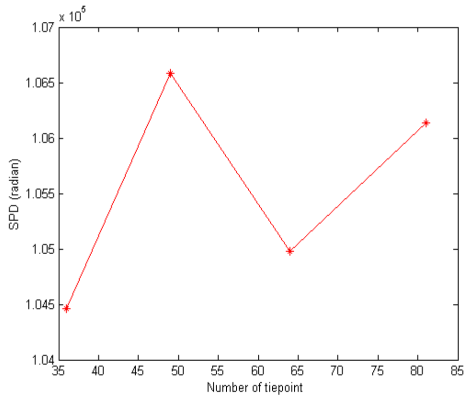

(a) SPD of No.1 image

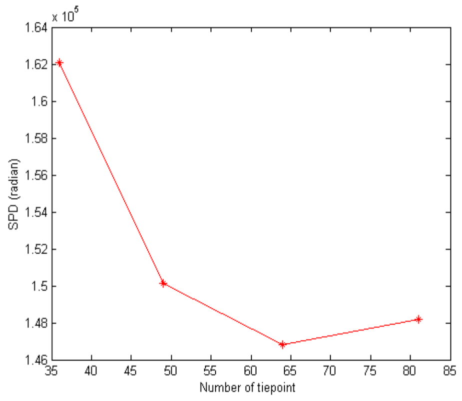

(b) SPD of No.2 image

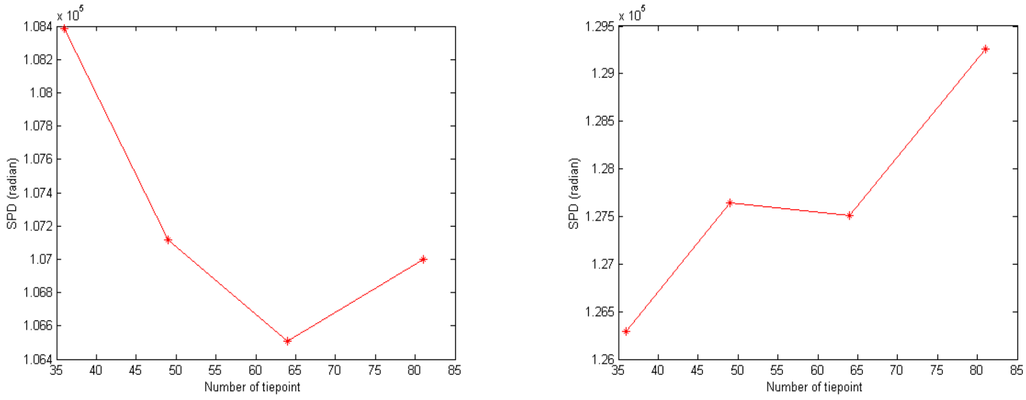

(c) SPD of No.3 image

(d) SPD of No.4 image

Fig. 4.3 Relationship between SPD values and tiepoint interval on four test areas

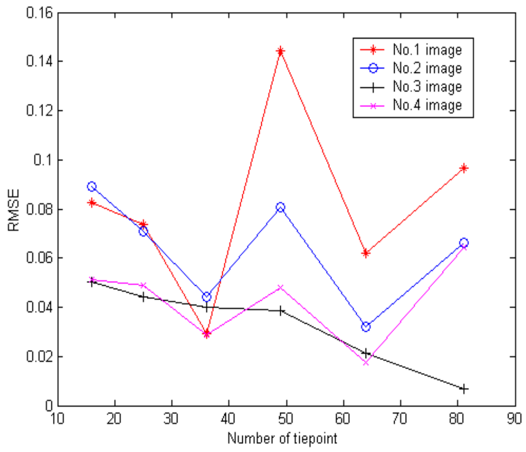

Fig. 4.4 Relationship between RMSE of tiepoints and tiepoint interval on four test areas

The relationship between the SPD and the grid interval for every test area are given in Fig. 4.3. The relationship between the RMSE of tiepoints and the grid interval for all these four test areas are given in Fig. 4.4.

From these results, it can be seen that the variations of quality of interferogram with the tiepoint interval are different for the four test areas. The change of SPD is not very significant. It seems that the tiepoint interval is not a very sensitive parameter for co-registration. But it is specially noticed that, when the grid interval is 205*34, corresponding to the 8*8 grid, all of the four RMSEs are small. All the corresponding SPDs are either very small or the smallest.

4.4 Effects of the tiepoint interval on the accuracy of the DEM

The DEM is the final product of InSAR image processing. For each test area, there is a corresponding reference DEM image as shown in Fig. 4.5. Since four interferograms, which correspond to tiepoint interval 273*44 to 182*29, are included in every test area, four DEM images corresponding to four interferograms are also included here. The DEM images are given in figures from Fig. 4.6.1 to Fig. 4.6.4. The results are shown in Table 4.3. The difference of δ_{DEM}, η_{DEM}, is also analyzed and derived as followers:

$$\eta_{\mathrm{DEM}} = |\,\delta_{\mathrm{DEM}\_8*8} - \delta_{\mathrm{DEM}\_i*i}\,| \,/\, \delta_{\mathrm{DEM}\_i*i}$$

Where δ_{DEM_8*8} is the δ_{DEM} of DEM generated by the grid size 8*8. δ_{DEM_i*i} is the δ_{DEM} of DEM generated by the grid size i*i. Therefore, the η_{DEM} between δ_{DEM_8*8} and the biggest δ_{DEM} is analyzed. Similarly, the η_{DEM} between SPD_{8*8} and the δ_{DEM} next to the biggest is also analyzed.

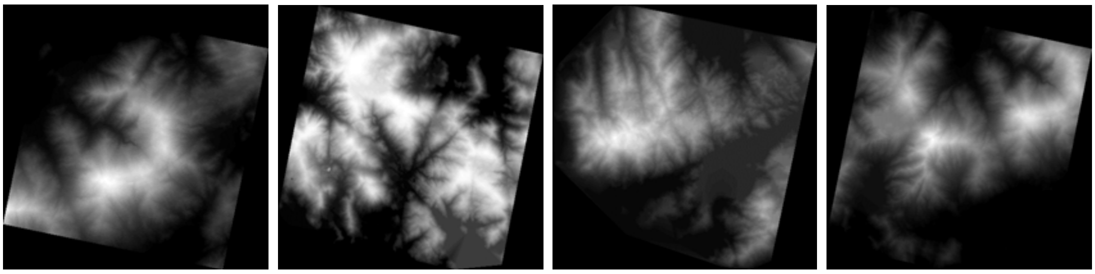

(a).DEM of No.1 testing area (b).DEM of No.2 testing area (c).DEM of No.3 testing area (d)DEM of No.4 testing area

Fig. 4.5 Reference DEMs corresponding to four test areas, respectively

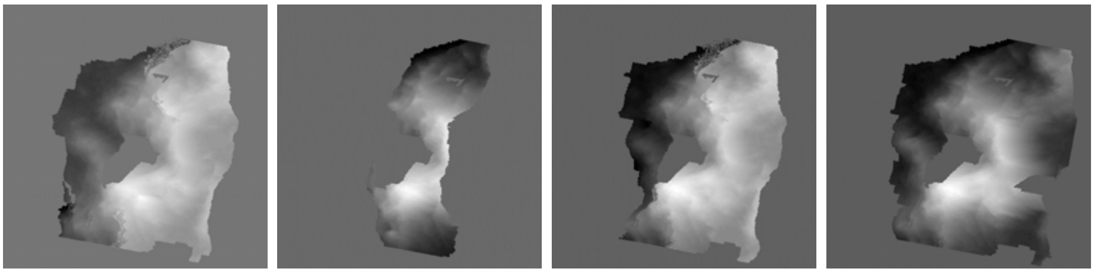

(a) Tiepoint interval: 273*44 (b) Tiepoint interval: 234*38 (c) Tiepoint interval: 205*34 (d) Tiepoint interval: 182*29

Fig. 4.6.1. DEMs of No.1 image in different tiepoint intervals

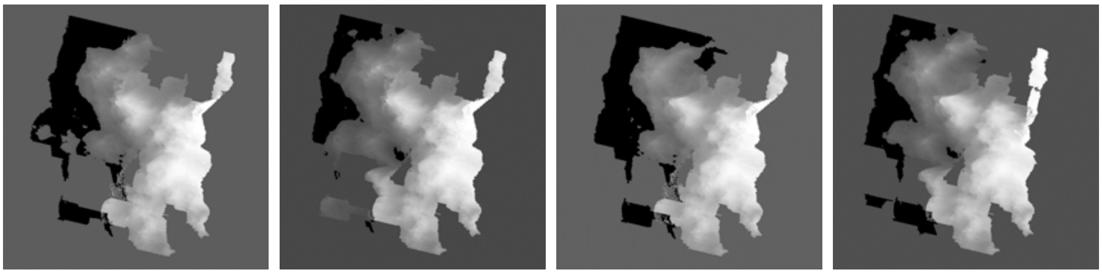

(a) Tiepoint interval: 273*44 (b) Tiepoint interval: 234*38 (c) Tiepoint interval: 205*34 (d) Tiepoint interval: 182*29

Fig. 4.6.2. DEMs of No.2 image in different tiepoint intervals

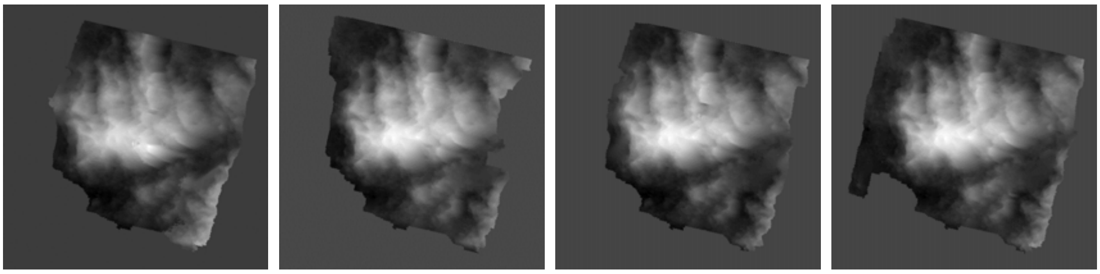

(a) Tiepoint interval: 273*44 (b) Tiepoint interval: 234*38 (c) Tiepoint interval: 205*34 (d) Tiepoint interval: 182*29

Fig. 4.6.3. DEMs of No.3 image in different tiepoint intervals

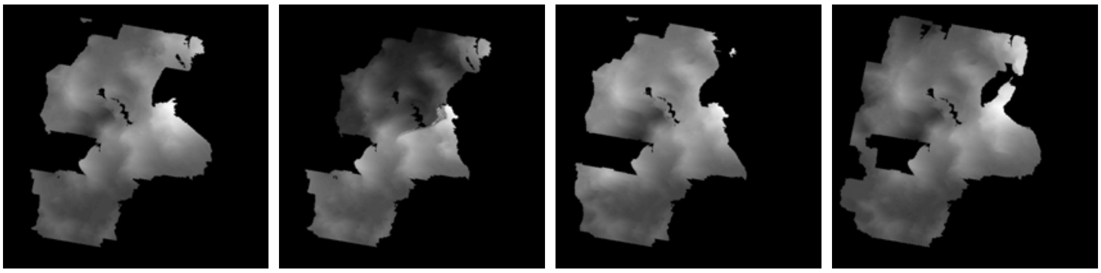

(a) Tiepoint interval: 273*44 (b) Tiepoint interval: 234*38 (c) Tiepoint interval: 205*34 (d) Tiepoint interval: 182*29

Fig. 4.6.4. DEMs of No.4 image in different tiepoint intervals

Fig. 4.6 DEMs generated in different tiepoint intervals on four test areas

Table 4.3 Data of DEMs generated by different tiepoint intervals

Tiepoint interval		No.1 Image		No.2 Image		No.3 Image		No.4 Image	
In row	In column	DEM image	δ_{DEM} (m)	DEM image	δ_{DEM} (m)	DEM image	δ_{DEM} (m)	DEM image	δ_{DEM} (m)
273	44	Fig 4.6.1.a	20	Fig 4.6.2.a	28	Fig 4.6.3.a	25	Fig 4.6.4.a	20
234	38	Fig 4.6.1.b	26	Fig 4.6.2.b	26	Fig 4.6.3.b	23	Fig 4.6.4.b	24
205	34	Fig 4.6.1.c	22	Fig 4.6.2.c	22	Fig 4.6.3.c	21	Fig 4.6.4.c	23
182	29	Fig 4.6.1.d	24	Fig 4.6.2.d	23	Fig 4.6.3.d	22	Fig 4.6.4.d	25

For DEMs of No.1 image, when the tiepoint grid interval is 273*44, its δ_{DEM} is 20 meters, which is the smallest, meaning that the resultant DEM is the best among all. However, when the interval is 234*38, its corresponding δ_{DEM} is 26 meters, which is the largest. When the interval is 205*34, the δ_{DEM} is 22 meters, the second smallest. When the interval is 182*29, the δ_{DEM} is 24 meters. When interval is 205*34, the δ_{DEM_8*8} is smaller than δ_{DEM_7*7} and δ_{DEM_9*9} by 15% and 8%, respectively.

For DEMs of No.2 image, when the interval is 273*44, its δ_{DEM} (28 meters) is the largest. When the tiepoint interval is 234*38, its δ_{DEM} (26 meters) is relatively large. When the tiepoint interval is 205*34, the δ_{DEM} (22 meters) is the smallest. When the tiepoint interval is 182*29, the δ_{DEM} (23 meters) is relatively small. When interval is 205*34, the δ_{DEM_8*8} is smaller than δ_{DEM_6*6} and δ_{DEM_7*7} by 21% and 15%, respectively.

For DEMs of No.3 image, when the interval is 273*44, the δ_{DEM} (25 meters) is the largest. When the tiepoint interval is 234*38, the δ_{DEM} (23 meters) is relatively large.

When the tiepoint interval is 205*34, the δ_{DEM} (21 meters) is the smallest. When the tiepoint interval is 182*29, the δ_{DEM} (22 meters) is relatively small. When interval is 205*34, the δ_{DEM_8*8} is smaller than δ_{DEM_6*6} and δ_{DEM_7*7} by 16% and 9%, respectively.

For DEMs of No.4 image, when the interval is 273*44, the δ_{DEM} (20 meters) is the smallest among all. When the tiepoint interval is 234*38, the δ_{DEM} (24 meters) is relatively large. When the tiepoint interval is 205*34, the δ_{DEM} (23 meters) is next to the smallest. When the tiepoint interval is 182*29, the δ_{DEM} (25 meters) is the largest. When interval is 205*34, the δ_{DEM_8*8} is smaller than δ_{DEM_7*7} and δ_{DEM_9*9} by 4% and 8%.

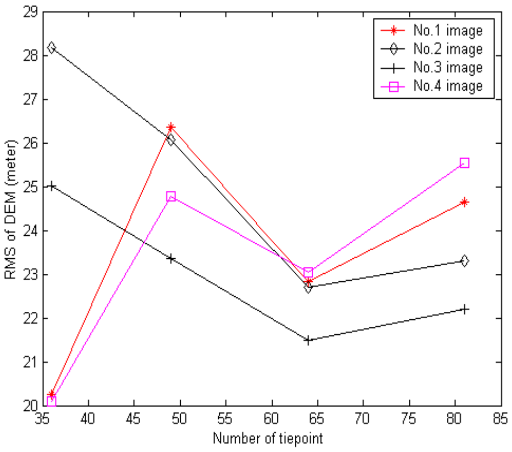

Fig. 4.7 Relationship between the DEM accuracy and the tiepoint interval on four test areas

The variations of DEM accuracy with the tiepoint interval are shown in Fig.4.7. It can be seen that the change of δ_{DEM} is not very significant. From the test results and analysis on the quality of interferogram and the accuracy of DEM, it can be found that the tiepoint interval is not a very sensitive parameter for co-registration. But, specially, when the grid interval is 205*34, corresponding to the 8*8 grid, it can make the co-registration more reliable, with these images.

4.5 A further test

From the analysis of test results, it is found that the RMSE of DEM is small when the grid interval is 205*34. However, from Fig.4.4, it can be found that when the grid size is 6*6, the RMSE of tiepoints is small for all four images. However, surprisingly, the resultant interferogram for No.2 area is the worst, despite the good results for all three areas. Additionally, in Fig.4.7, it is noticed that when grid size is 6*6, DEMs' RMSE of No.1 and No.4 areas are very small. But for No.2 and No.3 area, the resultant DEM accuracy is worst or worse. In order to make the findings from this study more reliable, a pair of SAR images (Fig.4.8) with much larger area (2862*624) is employed for further investigation. The results of RMSE of tiepoints are shown in Fig.4.9. The SAR image processing data on Hong Kong Mui Wo are included in Table 4.4. The resultant interferograms are shown in Fig.4.10.

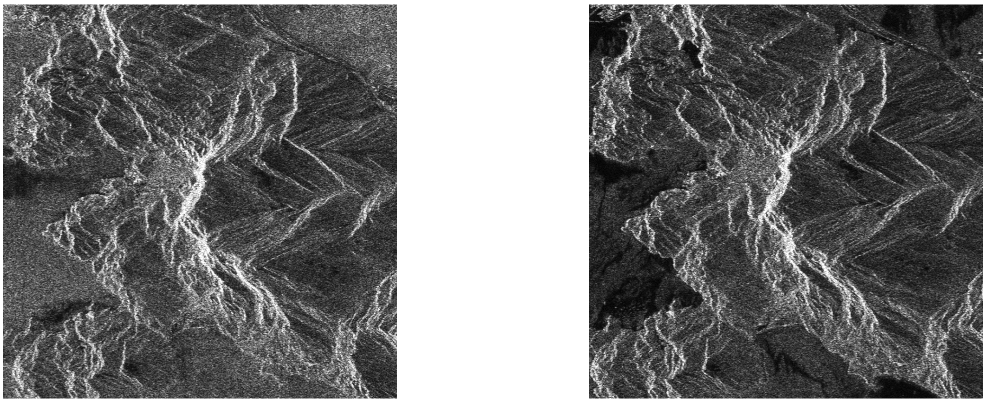

Master image obtained by ERS-2

Slave image obtained by ERS-1

Fig.4.8 A pair of SAR images of Mui Wo in Lantau Island in Hong Kong

Table 4.4. SAR image processing data of Mui Wo in Hong Kong

SAR image size(pixel)	Tiepoint Interval (pixel)		Grid size (pixel)	RMSE of tiepoints (pixel)	Interfero -gram	SPD (radian)	DEM image	δ_{DEM} (m)
	row	colum						
2862*624	411	68	6*6	0.0681	Fig 4.10.a	133,620	Fig 4.13.a	28
	328	53	8*8	0.0680				
	273	44	9*9	0.0425				
	234	38	11*11	0.0395	Fig 4.10.b	127,620	Fig 4.13.b	22
	205	34	13*13	0.0411	Fig 4.10.c	128,520	Fig 4.13.c	23
	182	29	14*14	0.0577	Fig 4.10.d	131,120	Fig 4.13.d	25

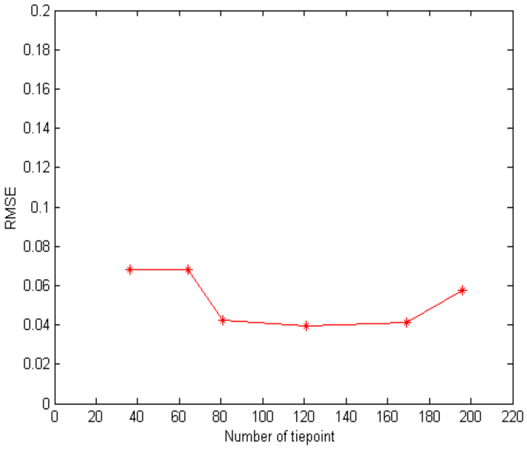

Fig.4.9 Relationship between RMSE of tiepoints and tiepoint interval

These results are obtained with identical parameters. The only difference being the grid interval is larger in terms of number of pixels for the same number of grid lines. For example, the 4*4, 5*5, … 9*9 are corresponding to 6*6, 8*8, … 14*14. The above six different tiepoint intervals are adopted. Four interferograms are respectively shown in Fig.4.10.a, Fig.4.10.b, Fig.4.10.c and Fig.4.10.d. Their tiepoint intervals are 411*68, 234*38, 205*34, 182*29, respectively. The SPD corresponding to these four situations are shown in Fig.4.11. The reference DEM shown in Fig.4.12 is derived from contour whose interval is 10 meters. The DEM images corresponding to different tiepoint interval are respectively shown in Fig.4.13.a, Fig.4.13.b, Fig.4.13.c and Fig.4.13.d. The δ_{DEM} of DEM obtained from InSAR corresponding to different tiepoint interval is shown in Fig.4.14.

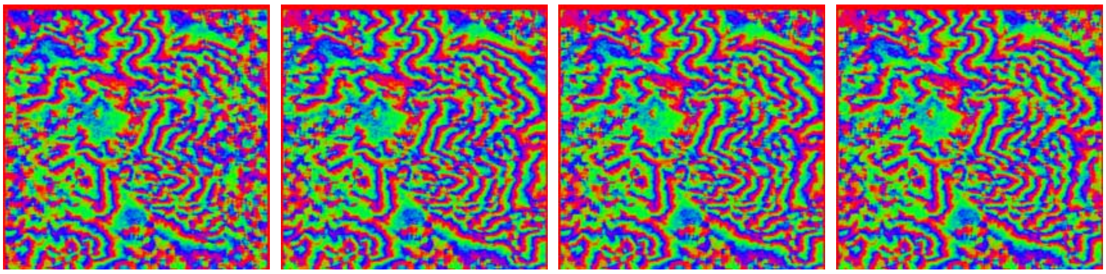
a Tiepoint interval: 411*68 b Tiepoint interval: 234*38 c Tiepoint interval: 205*34 d Tiepoint interval: 182*29

Fig.4.10 SAR image interferograms of Hong Kong Mui Wo in different tiepoint intervals

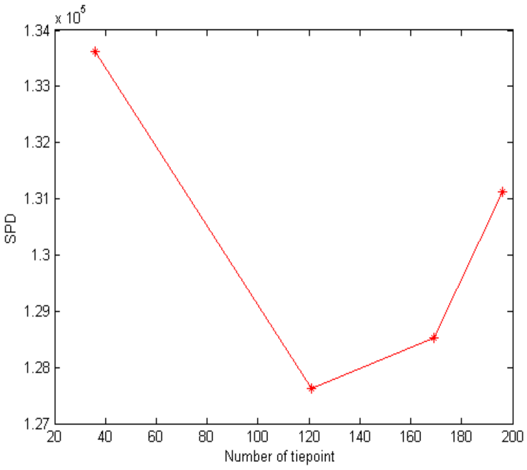

Fig.4.11 Relationship of SPD values and tiepoint intervals

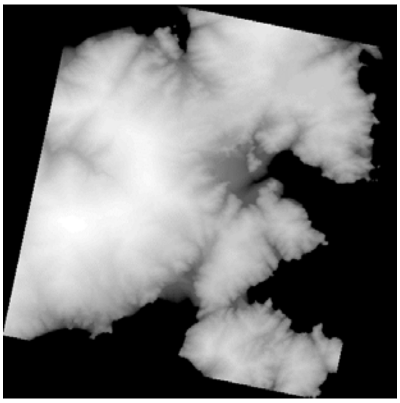

Fig.4.12 Reference DEM corresponding to Mui Wo area

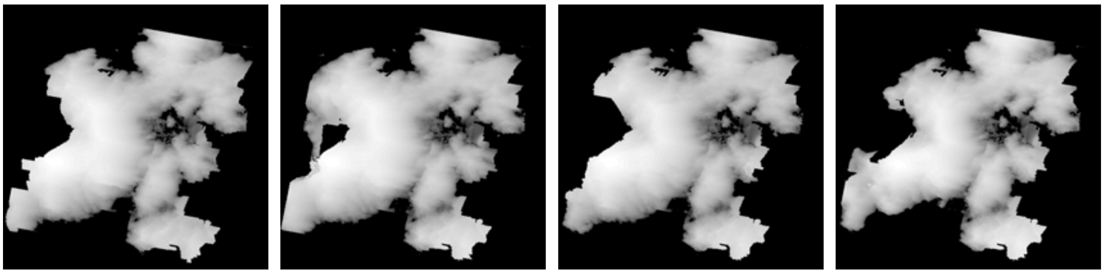

a.Tiepoint interval: 411*68 b.Tiepoint interval: 234*38 c.Tiepoint interval: 205*34 d.Tiepoint interval: 182*29

Fig.4.13 DEMs of Mui Wo in different tiepoint intervals

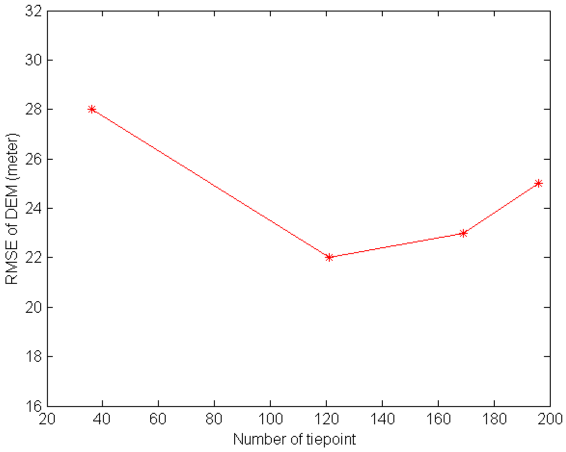

Fig.4.14 Relationship between the DEM accuracy and the tiepoint interval on Mui Wo area

From Fig. 4.9 and Fig. 4.11, it could be found that the RMSE, 0.0411, and the SPD, 128,520, are small when the tiepoint interval is 205*34. The variation of DEM accuracy with tiepoint interval is shown in Fig. 4.14. It is noticed that the DEM is accurate when the tiepoint interval is 205*34.

This test has been carried out on a large area for more reliable finding. From the test results, the similar finding as previous has been obtained. Although the tiepoint interval is not a very sensitive parameter for co-registration, it can make the co-registration more reliable when the grid interval is 205*34.

4.6 Summary

This chapter aims to analyze the effects of tiepoint interval on the reliability of co-registration. In the study, the tiepoint interval is the only factor considered while others are kept unchanged. Based on the quality of interferogram and the accuracy of DEM, the effects of tiepoint interval is implemented.

Based on the strategy for the experiment, four pairs of images sized 1760*400 pixels have been used for testing the variation of the qualities of products with the tiepoint interval. It has been noticed that although the tiepoint interval is not a very sensitive parameter for co-registration, the interferogram is best and the DEM is accurate when tiepoint interval is 205*34. In order to make the finding more reliable, an image with much larger size, i.e. 2862*624 pixels, has been used for a further test. Similar results were also obtained. From these test results, the follows could be concluded:

(1) The tiepoint interval is not a very sensitive parameter and can be chosen rather freely. However, the grid interval with around 200*30 pixels is appropriate for co-registration that can make co-registrations more reliable;

(2) The tests are limited on SAR image about hill area in Hong Kong. The tiepoint interval around 200*30 pixels can be used as a guideline for processing SAR image of hill area.

Chapter 5

Determining the optimum window size for tiepoint matching based on decomposition of auto-correlation by wavelet

The tiepoint interval, one of the important factors that affect the reliability of co-registration, was studied in last chapter. Another important factor to be considered in SAR images co-registration is the window size for tiepoint matching. Therefore, this chapter investigates how to determine the optimum window size based on decomposition of auto-correlation by wavelet.

5.1 The line of the thought

The concept of optimization has been widely used in many fields, such as control field. Optimization is the aim for most projects to get the best result based on a certain parameter. In other words, the optimum result could be obtained based on a parameter while it could not be obtained based on other parameters.

Concretely, in tiepoint matching, the optimum window size refers to the window size that could result in the best results of InSAR products, i.e. the intermediate product – interferogram, and the final product -- DEM. Just as described previously, the quality of interferogram can be measured by SPD while the accuracy of DEM could be measured by δ_{DEM}. Based on the optimum window, the SPD and δ_{DEM} should be the smallest if one compares the results obtained based on windows with different sizes.

At present, from literatures, the determination of optimum window size for tiepoint matching is almost made by experiences. In this way, a series of experiments has to be implemented by different window sizes. The window size that corresponds to the best result is selected as the optimum window size. It takes a lot of time in the experiments for the determination of optimum window size with this way. Different optimum window sizes have been selected by different researchers, such as 33*33 pixels selected by Zebker et al. (1994b) and 63*63 pixels selected by Liao (2000). Therefore, it is a matter of some urgency to find a way to determine optimum window size.

The tiepoint matching is usually implemented based on the cross-correlation maximization. As described in chapter 2, in order to find the points in the slave image, there are a lot of possible matches of windows of the same size. Every match of window corresponds to a cross-correlation coefficient, but only the match with the highest cross-correlation coefficient is regarded as the best match. It is noticed that the window size could influence the cross-correlation coefficient and the result of tiepoint matching. Therefore, it leads to the thought that, perhaps, there is a relation between the window size and the correlation.

Correlation reflects the degree of similarity between pixels in images. If the gray values of pixels are identical, then the correlation coefficient is 1. If they are totally different, the correlation coefficient is 0. When pixels in two independent images are compared, the procedure is known as cross-correlation. When the pixels in the same image are compared to distance shifted copies of themselves, the procedure is known as autocorrelation.

In short, the optimum window size refers to the size with which the best tiepoint matching is achieved. The best tiepoint matching is normally measured by the highest cross-correlation. User is usually interested in the best products (i.e. interferogram and DEM). Here, the optimum window size refers to the size with which the best interferogram and DEM can be generated. Different optimum window sizes are for different images because of different terrain variation and features. The optimum window size could be determined by analyzing an image with the auto-correlation function. The auto-correlation could be analyzed by wavelet because it has powerful analysis of a signal at different scales. It is very effective in detecting a signal rupture.

5.2 Computation of auto-correlation within a window size

In one dimension, the auto-correlation function is defined as:

$$R(d) = \frac{Cov(d)}{V} \tag{5.1}$$

where, R(d) is the autocorrelation coefficient of all pixels with the distance of d part. Cov(d) is the covariance of all pixels with the distance of d part. V is the variance of all pixels. Respectively, they are as follows:

$$V = \frac{\sum_{i=1}^{N} (Z_i - M)^2}{N - 1} \tag{5.2}$$

and

$$Cov(d) = \frac{\sum_{i=1}^{N} (Z_i - M)(Z_{i+d} - M)}{N - 1} \tag{5.3}$$

where Z_i is the ith pixel's gray value. Z_{i+d} is the gray value of pixel whose distance is d from the ith pixel. M is the average of all pixels. N is the total number of pixels used in calculation.

Obviously, Cov(d) varies with d, so does R(d) derived from Cov(d). Normally, the bigger the d, the smaller Cov(d) and R(d). Their relations can be described by density function or Gauss function, as follows:

$$Cov(d) = V \times e^{-\frac{2d}{c}} \tag{5.4}$$

$$Cov(d) = V \times e^{-\frac{2d^2}{c^2}} \tag{5.5}$$

where c is the correlative distance when Cov(d) tends to zero. The covariance and the autocorrelation denote the average degree of similarity of all pixels.

In two dimension, Cov(d) and V are respectively as follows:

$$V = \frac{\sum_{i=1}^{N} \sum_{j=1}^{K} (Z_{i,j} - M)^2}{(N - 1)(K - 1)} \tag{5.6}$$

$$Cov(d) = \frac{\sum_{i=1}^{N} \sum_{j=1}^{K} [(Z_{i,j} - M)(Z_{i,j+d} - M) + (Z_{i,j} - M)(Z_{i+d,j} - M)]}{(N-1)(K-1)} \tag{5.7}$$

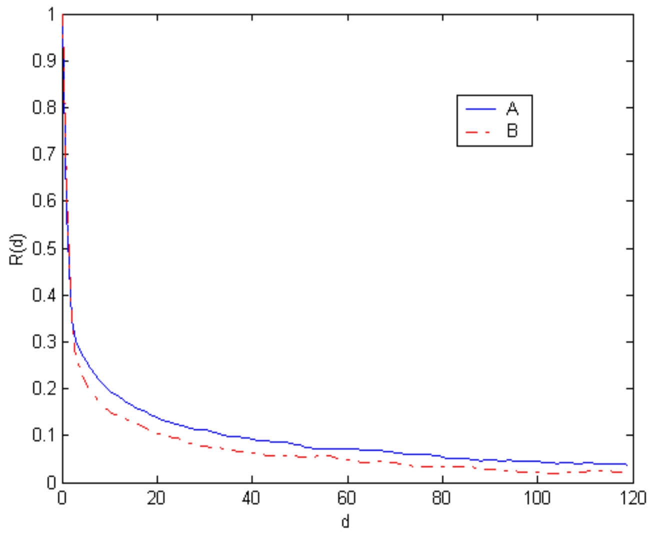

Fig 5.1 Variation of auto-correlation with distance

Figure 5.1 is a relation illustration about R(d) and d. Supposedly, there are two images. Curve A represents the variation of R(d) with d in the first image, while B represents another variation of R(d) with d in the second image. Comparing curve A and B, it is noticed A trends towards zero slowly while B does so quickly. This indicates the degree of similarity between pixels in the second image (autocorrelation expressed by curve B) decreases faster than the one in the first image (autocorrelation expressed by curve A).

From Fig.5.1, it is obvious that the autocorrelation coefficient varies with the increasing distance, and it may greatly changes at some points. The point could be used as window size for tiepoints matching. Ideally, when the autocorrelation coefficient is zero, it means there is no correlation between pixels. Therefore, this point could be the optimum window size for tiepoint matching. Actually, the autocorrelation coefficient may not go down to zero but tend to a steady number.

In order to get the optimum window size, the decomposition of signal with wavelet can be used for analyzing the variation of autocorrelation coefficient because of the powerful analysis of wavelet. Obviously, the autocorrelation function, R(d), could be regarded as a signal varying with d. Based on wavelet multiresolution analysis, this signal could be decomposed into low and high frequency components. It could be noticed, as shown later, that there are some jumps of amplitude in the low frequency components. The low frequency component is corresponding to the signal's overall trend whose variation, such as jumps, could be found. The corresponding high frequency component represents the local variation. By analyzing the low and high frequency components, some characteristics on auto-correlation could be observed. The value of distance corresponding to every jump could be used as a window size. These different window sizes will result in different results. After a certain jump, if the amplitude of low and high frequency component almost keeps the same, the distance corresponding to this jump may be the optimum window size for tiepoint matching.

5.3 Determination of optimum window size based on auto-correlation

5.3.1 Decomposition of signal with wavelet

Optimum window size could possibly be obtained by decomposing auto-correlation. In order to decompose an auto-correlation, wavelet is inducted. The theory of wavelet originates from signal theory from the 80s. It has been one of the major research directions in science in the last decade and is still undergoing rapid growth (Lau, 1998). Wavelet has been widely used in signal analysis and image processing (Chan and Peng, 2003). Since wavelet transform can zoom in a signal, so the detailed features of the signal can be observed and analyzed.

The heart of signal processing lies to the task of extracting specific information from a signal, such as the occurrence of certain patterns, periodic ranges, discontinuities, irregularities and other similar features. The wavelet transformation can give a contribution to the answer to these questions whenever the sought phenomena show a multi-scale structure. Typical examples are edges, jumps or locally varying orders of differentiability, which can easily be seen by the asymptotic behaviour of the wavelet transform (Kaiser, 1994; Tang et al., 2000).

The wavelet transform has gained a great deal of interest due to its time localization and multiresolution properties. Fourier transform lacks time localization as frequency components are attributed to the entire time signal and not to specific parts of it. Windowed Fourier Transforms achieves this localization by using a window function that limits the duration of the analyzed signal segment. Windowed Fourier Transforms uses fixed size windows that cannot be adjusted to suit the speed of the changing phenomena observed in the input signal. Wavelets solve this problem by using the so called mother wavelet which can be scaled and translated to achieve both time localization and multiresolution where the decomposition of a signal is in terms of the resolution of detail (Chui, 1197; Resnikoff and Wells, 1998).

The multiresolution decomposition seems to separate components of a signal in a way that is superior to most other methods for analysis, processing, or compression. Because of the ability of the wavelet transform to decompose a signal at different independent scales and to do it in a very flexible way, Burke calls wavelets "The Mathematical Microscope" (Cohen and Ryan, 1995; Burke 1994).

In the multiresolution analysis, for scale function $\varphi(x)$ and wavelet function $\psi(x)$, the binary shift and zoom of the scale function will derive a series of functions: $\varphi_{j,k}(x) = 2^{j/2}\varphi(2^j - k)$, which consists of orthogonal bases in vector space V_j. For variable j, the function set $\{\psi_{j,k}(x) = 2^{j/2}\psi(2^j - k)\}$ also forms the supplementary space W_j. For a signal $f(x) \in L^2(R)$, in scale j, its smooth signal is

$$A_j^d f = \left\langle f(x), \varphi_{j,k}(x) \right\rangle = 2^{j/2}\int f(x)\varphi(2^j x - k)dx \tag{5.8}$$

Its detailed signal is

$$D_j f = \left\langle f(x), \psi_{j,k}(x) \right\rangle = 2^{j/2}\int f(x)\psi(2^j x - k)dx \tag{5.9}$$

Decomposing $f(x)$, from scale j+1 to scale j, is the process from high resolution to low resolution, that is, $A_{j+1}^d f$ is decomposed into $A_j^d f$ and $D_j f$:

$$A_j^d f = \sum_k h(k - 2n)\ A_{j+1}^d f \tag{5.10a}$$

$$D_j f = \sum_k g(k - 2n)\ A_{j+1}^d f \tag{5.10b}$$

where, $g(n)$ and $h(n)$ are high pass filter coefficient and low pass filter coefficient, respectively.

Wavelet analysis is useful in revealing signal trends, a goal that is complementary to the one of revealing a signal hidden in noise. It is important to remember that the trend is the slowest part of the signal. Every signal could be decomposed into two parts, low and high frequency component. The noise is contained in the high frequency component while the low frequency component corresponds to the overall trend of signal. As the scale increases, the resolution decreases, producing a better estimation of the unknown trend. Another way to think of this is in terms of frequency. Successive approximations possess progressively less high-frequency information. With the higher frequencies removed, what is left is the overall trend of the signal. The trend becomes clearer and clearer with each approximation.

In order to analyze the overall trend of signal, short wavelets are often more effective than long ones in detecting a signal rupture. The shapes of discontinuities that can be identified by the smallest wavelets are simpler than those that can be identified by the longest wavelets.

Therefore, wavelet db1 is selected for detecting discontinuities in the trend of signal. Wavelet db1 is presented by Daubechies (1988), one of the brightest starts in the world of wavelet research. He invented what are called compactly supported orthonormal wavelets, making discrete wavelet analysis practicable.

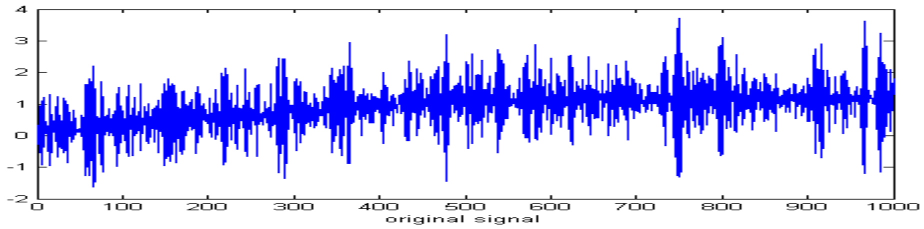

(a) Original signal

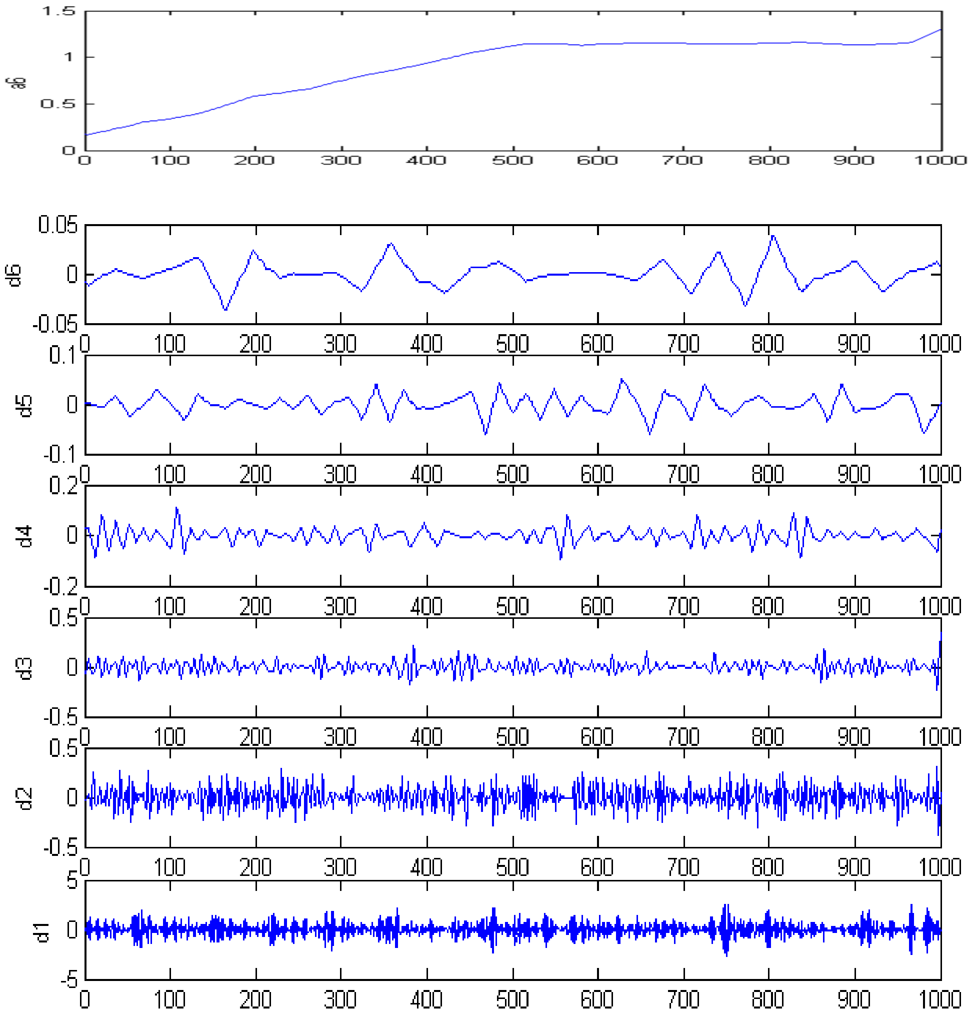

(b) Components decomposed by wavelet db3

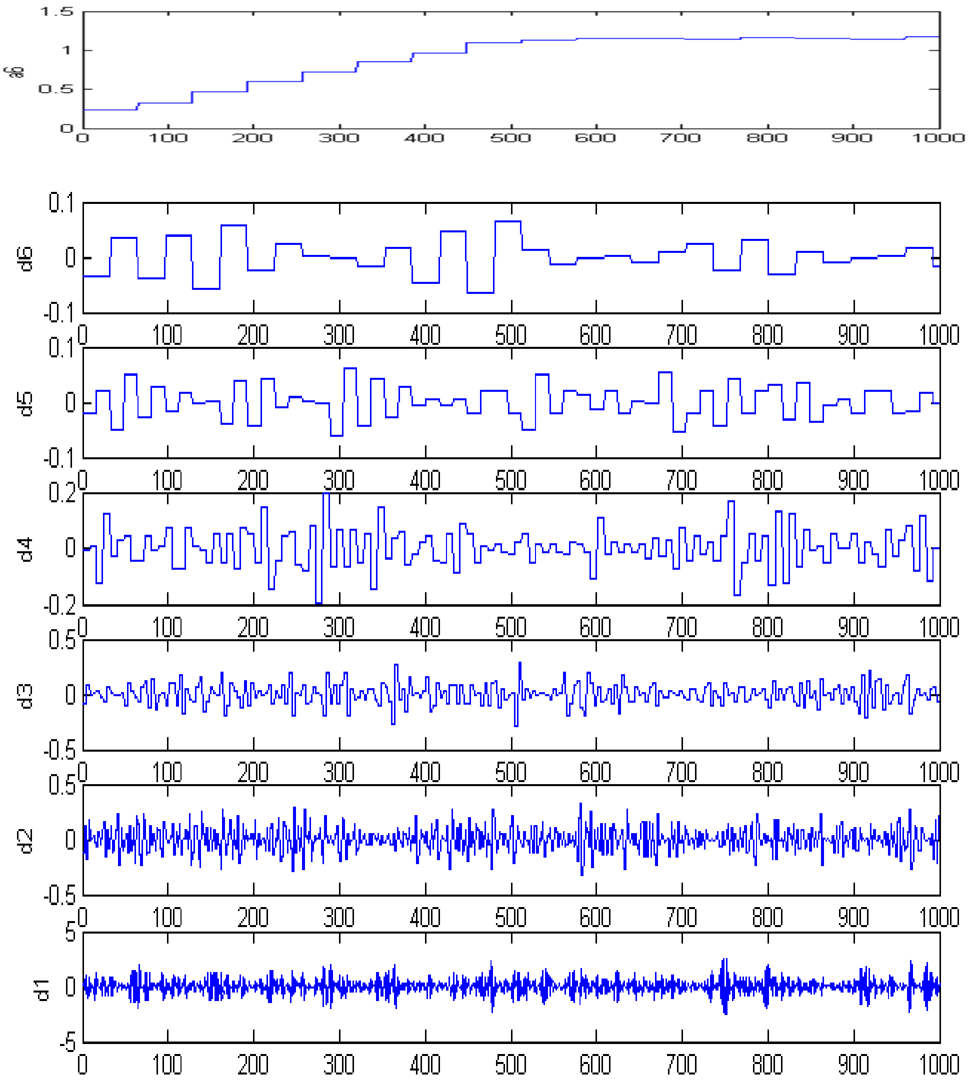

(c) Components decomposed by wavelet db1

Fig. 5.2 Original signal and its components

A signal and its components decomposed by wavelet are shown in Fig.5.2 to illustrate the characteristics of wavelet as discussed above. Fig.5.2.a shows the original signal, a time serious signal. There is so much noise in the original signal that its overall shape is not apparent upon visual inspection. Fig.5.2.b shows its decomposed components based on wavelet db3, while Fig.5.2.c shows its decomposed components based on wavelet db1. The multiresolution analysis has been used in the decomposition. In Fig.5.2.b, the components from d1 to d6 are the high frequency components while a6 is the low frequency component. The trend of signal is reflected in a6. It is noticed that all of the components are varying smoothly. Obviously, it is difficult to find the jumps in a6. In other words, the details on the discontinuity of amplitude in a6 are difficult to be observed.

However, it is different in Fig.5.2.c. All of the components are obtained based on wavelet db1. D1, …, d5 and d6 are the high frequency components. A6 is the low frequency component corresponding to the trend of signal. It is noticed that several jumps of amplitude in a6 could be found. Specially, there are several big jumps of amplitude at t=65,129,193,257,321,385,449, respectively. Although there are other jumps after t=449, the variations of amplitude are very small. The variation of amplitude, especially for the variation in the jumping point, may reflect some of the basic characteristics of signal. This may be what the observation wants to get.

5.3.2 Decomposition of auto-correlation with wavelet

Just as discussed in last section, wavelet db1 is used for decomposing the auto-correlation as shown in Fig.5.3. Fig.5.3.a is the original signal about the autocorrelation coefficient varying with the distance. The curve is derived from a SAR image. Fig.5.3.b is its components including high frequency components, d1 to d4, and low frequency component a4, which reflects the trend of signal.

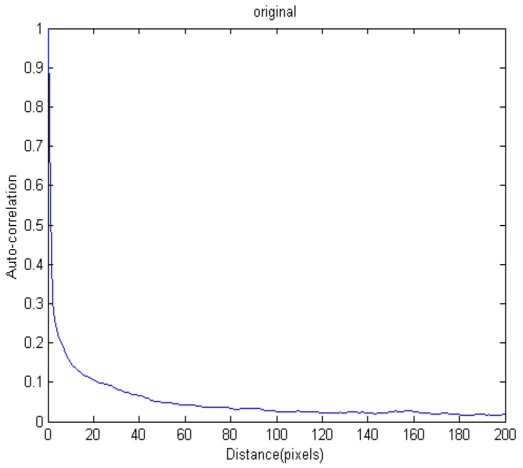

(a) Original signal

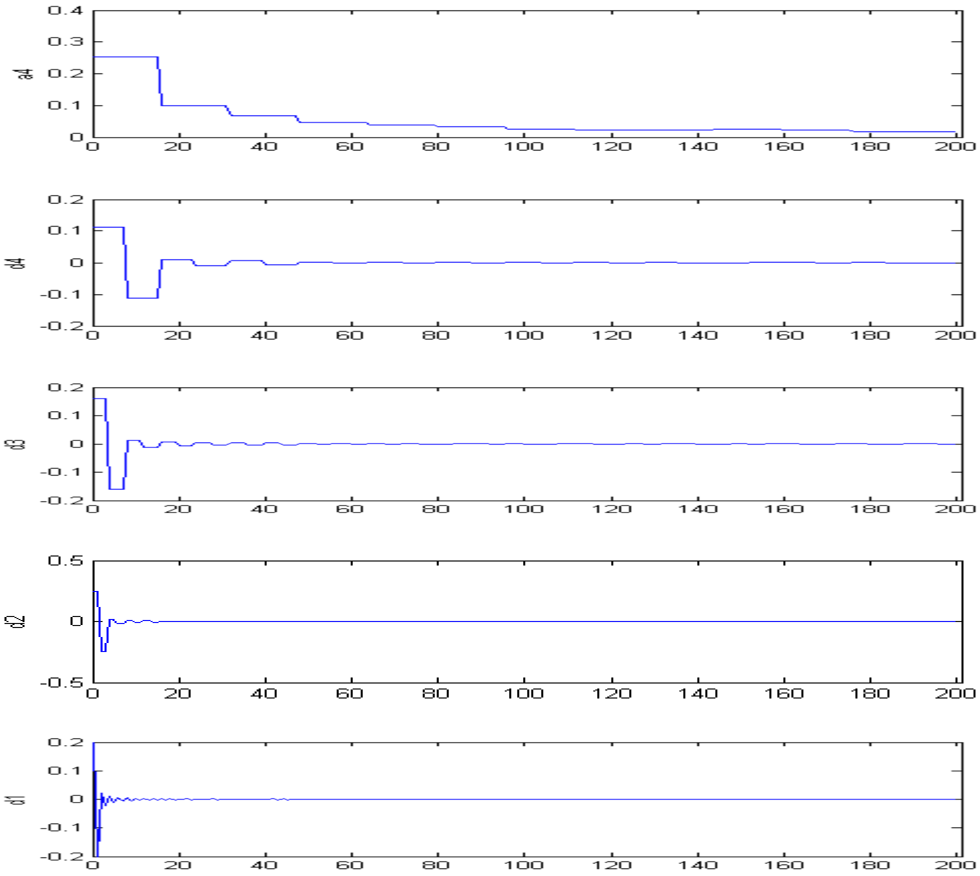

(b) Components decomposed by wavelet

Fig.5.3 Auto-correlation coefficient and its components decomposed by wavelet

5.3.3 Determination of optimum window size

From Fig.5.3, it can be noticed that the amplitude of a4 gradually tends to small one -- a steady number. Although there are some jumps in a4, the jumps at 17, 33 and 49, should be considered because of big changes of amplitude in these points. Obviously, after jumping point 49, the amplitude of the low frequency component has very little change and almost remains the same. The corresponding amplitude of high frequency component in d4 also has very little variation after point 49. Therefore, based on the previous description, 49*49 could be the optimum window size for tiepoint matching here. Of course, it could be proved by the quality of product.

5.4 Experimental evaluation

5.4.1 Design of the experiment

In the experiment, the SAR image of Tai Lam in Hong Kong is employed and its size is 1760*400 pixels. The pair of SAR images, master image and slave image as shown in Fig.5.4, has been obtained by ERS-1/2. Based on the SAR image, its autocorrelation coefficient is derived according to the formula (5.1). The autocorrelation coefficient is decomposed with wavelet db1 for detecting the variation of amplitude in low and high frequency components.

There could be several jumps in the low frequency component. In order to make the determination more reliable, several different window sizes corresponding to distance values in these jumps are used for tiepoint matching. With these different window sizes, the corresponding interferograms are carried out and their qualities are compared by their SPDs, which are derived from formula (3.3) in chapter 3. Corresponding to these different window sizes, the final products DEMs are produced and their accuracy is compared by δ_{DEM} that is calculated with formula (4.1) in chapter 4.

According to the way for determining optimum window size described previously, the optimum window size could be determined based on analyzing the variation of amplitude in low and high frequency components and could be proved by the quality of interferogram and the accuracy of DEM.

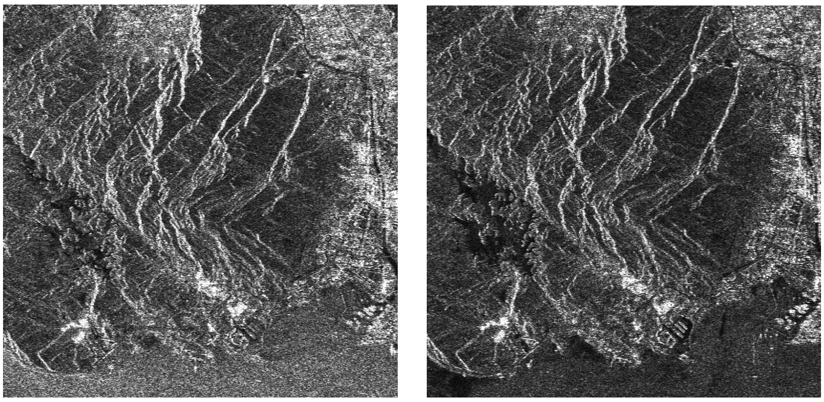

Master image

Slave image

Fig.5.4 A pair of SAR images on Tai Lam in Hong Kong

5.4.2 Execution of experiment

Based on the SAR image, the auto-correlation coefficient has been calculated and it is shown in Fig.5.5. From the curve, it is noticed that the auto-correlation coefficient goes down rapidly when the distance is increasing from 0 (pixel) to 60 (pixels). After 60 in distance, the auto-correlation coefficient does not show big changes and gradually goes to a steady number. The wavelet is needed for detecting the details.

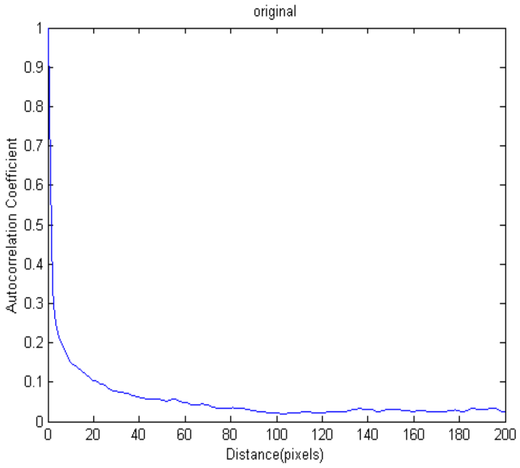

Fig.5.5 Variation of auto-correlation with the distance

The signal, auto-correlation coefficient, has been decomposed into two parts including low frequency component and high frequency components as shown in Fig.5.6. The low frequency component is a4 while the high frequency components consist of d1, d2, d3 and d4. The a4 reflects the trend of signal and the d4 reflects the local variation. They attract the attention of investigation. Totally, there are eleven jumps in a4 varying with distance. We only consider the first seven jumping points in distance, because the amplitude has very little changes after them. They are corresponding to distance=17, 33, 49, 65, 81, 97 and 113. Corresponding to these jumps, their amplitudes are 0.0956, 0.0639, 0.0524, 0.0384, 0.0301, 0.0216 and 0.0236 respectively. When the distance is 0, the whole amplitude is 0.2636. The amplitude rate is defined as the rate between the amplitude in every jump point and the whole amplitude 0.2636. In every jump, the amplitude rates are 36.27%, 24.24%, 19.88%, 14.57%, 11.42%, 8.19% and 8.95%, respectively. From the variation of these amplitudes, it is noticed that the amplitude of signal is becoming smaller and smaller when the distance is increasing.

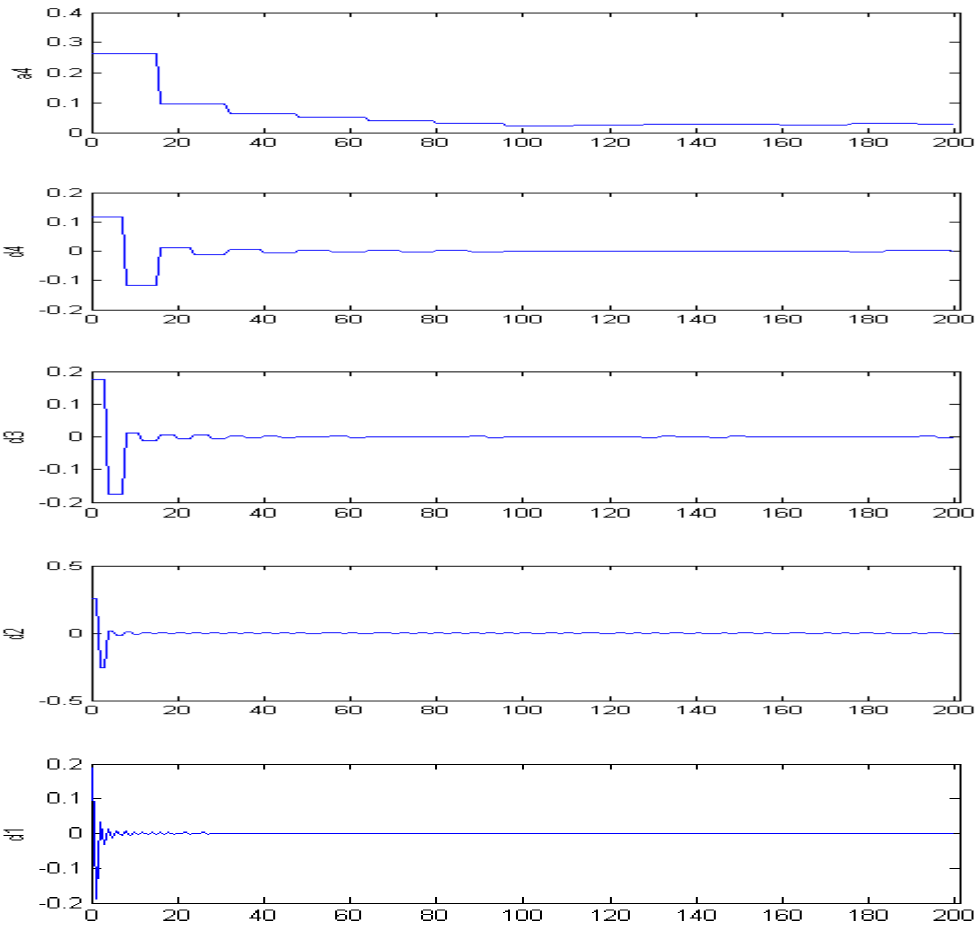

Fig.5.6 Components of auto-correlation decomposed by wavelet

When the distance is 17, the amplitude varies from 0.2636 to 0.0956. The change of amplitude is 0.168. Its changed amplitude rate at this point is 63.73%. The change rate of amplitude is defined as the rate between the changed amplitude and the whole amplitude 0.2636. When the distance is 33, the amplitude varies from 0.0956 to 0.0639. Its change rate of amplitude at this point is 12.03%. When the distance is 49, the amplitude varies from 0.0639 to 0.0524. Its change rate of amplitude at this point is 4.36%. When the distance is 65, the amplitude varies from 0.0524 to 0.0384. Its change rate of amplitude at this point is 5.31%. When the distance is 81, the amplitude varies from 0.0384 to 0.0301. Its change rate of amplitude at this point is 3.15%. When the distance is 97, the amplitude varies from 0.0301 to 0.0216. Its change rate of amplitude at this point is 3.22%. When the distance is 113, the amplitude varies from 0.0216 to 0.0236. Its change rate of amplitude at this point is 0.76%. Obviously, the change rate of amplitude becomes smaller and smaller when the distance becomes bigger and bigger

Table 5.1 Amplitude data of low frequency component

Distance value at jump points	Amplitude at jump points	Amplitude rate	Change rate of amplitude
17	0.0956	36.27%	63.73%
33	0.0639	24.24%	12.03%
49	0.0524	19.88%	4.36%
65	0.0384	14.57%	5.31%
81	0.0301	11.42%	3.15%
97	0.0216	8.19%	3.22%
113	0.0236	8.95%	0.76%

From the change rate of amplitude at every jumping point, it is noticeable that the trend of signal goes down to a stable number. The data about the variation of amplitude in these jumps are included in Table 5.1. It is noticed that when the distance is greater than 65, the change rate of amplitude is very small. This reflects the basic characteristic of the original signal, autocorrelation function. That is the autocorrelation almost remains unchanged after the jumping point at 65. From Fig5.6, it is also seen that the amplitude of high frequency component in d4 almost shows no variation after point 65. This represents the local variation of the signal. Therefore, 65*65 could be the optimum window size for tiepoint matching. Meanwhile, the other six values are also used as window sizes for making the determination of optimum window size more reliable. Totally, there are seven window sizes, 17*17, 33*33, 49*49, 65*65, 81*81, 97*97, 113*113, have been adopted for the experiments

5.4.3 Effects of window sizes on the quality of interferogram

The effects of window sizes on the quality of interferogram can be measured by the SPD. If the SPD is small, it means the window size used is good for tiepoint matching. Otherwise, the window size is bad. These results are included in Table 5.2. The seven interferograms corresponding to seven window sizes are given in Fig.5.7.

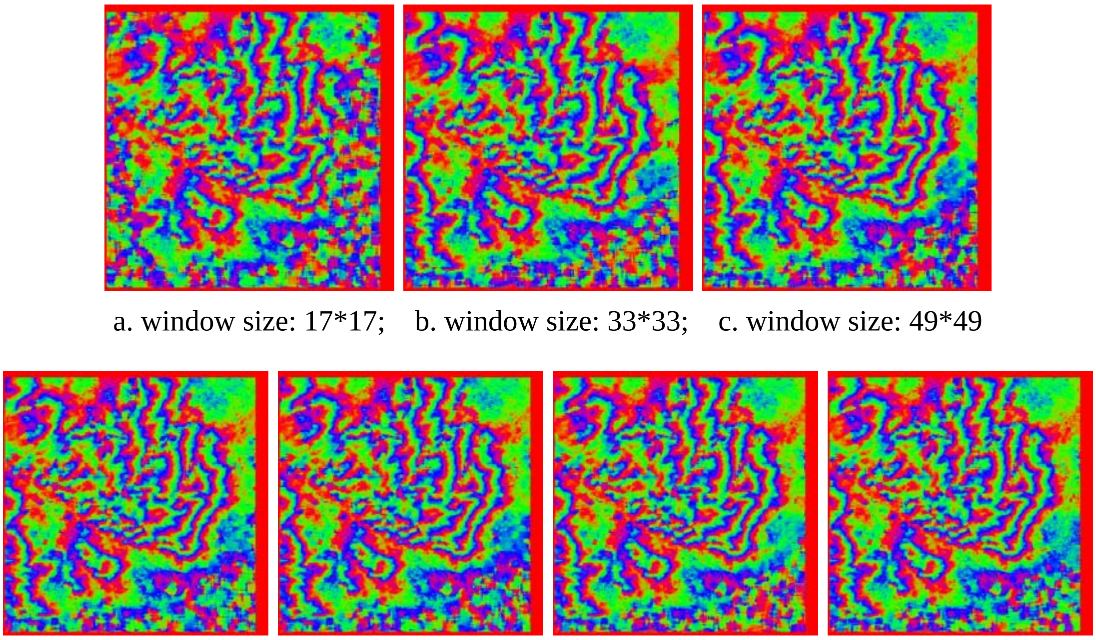

a. window size: 17*17; b. window size: 33*33; c. window size: 49*49

d.window size: 65*65; e.window size: 81*81; f.window size: 97*97; g.window size: 113*113

Fig.5.7 Interferograms with different window sizes

Table 5.2 Data of interferograms generated by different window sizes

SAR image size (pixel)	Window size (pixel)	Interferogram	RMSE at tiepoints (pixel)	SPD (radian)
1760*400	17*17	Figure 5.7.a	0.0653	109,800
	33*33	Figure 5.7.b	0.0454	107,430
	49*49	Figure 5.7.c	0.0254	106,070
	65*65	Figure 5.7.d	0.0150	105,610
	81*81	Figure 5.7.e	0.0202	105,740
	97*97	Figure 5.7.f	0.0011	107,110
	113*113	Figure 5.7.g	0.0134	106,540

For the interferogram in Fig.5.7.a, the window size is 17*17, the RMSE is 0.0653 and the SPD is 109,800 radians. Both of them are the largest among all. There is much noise in interferogram. The quality of interferogram is the worst. For the interferogram in Fig.5.7.b, the window size is 33*33, the RMSE (0.0454) is next to the largest. The SPD (107,430 radians) is also next to the largest. The quality of interferogram is worse. For the interferogram in Fig.5.7.c, the window size is 49*49. The RMSE is 0.0254, and the SPD is 106,070 radians. For the interferogram in Fig.5.7.d, the window size is 65*65, and the RMSE is 0.0150. The SPD (105,610 radians) is the smallest among all. Its quality of interferogram is the best. For the interferogram in Fig.5.7.e, the window size is 81*81. The RMSE is 0.0202. The SPD (105,740 radians) is next to the smallest. Its quality of interferogram is next to the best. For the interferogram in Fig.5.7.f, the window size is 97*97. The RMSE (0.0011) is the smallest among all. The SPD (107,110 radians) is relatively large. The quality of interferogram is not good. For the interferogram in Fig.5.7.g, the window size is 113*113, the RMSE (0.0134) is next to the smallest. The SPD is 106,540 radians.

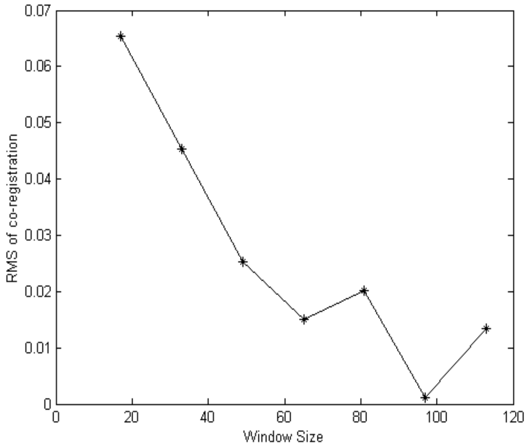

Fig.5.8 Effects of window sizes on RMSE of tiepoints

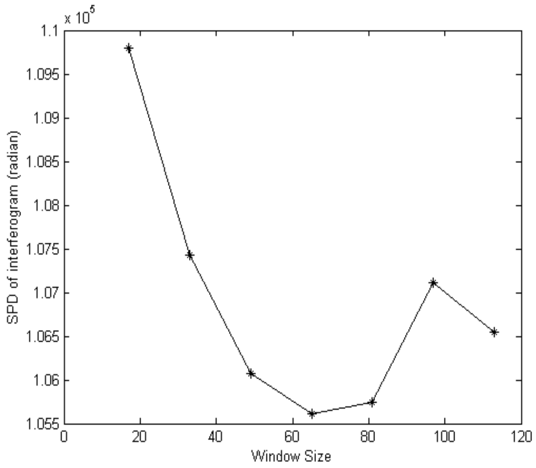

Fig.5.9 Effects of window sizes on SPD of interferograms

The Effects of window sizes on RMSE of tiepoints is shown in Fig.5.8. It is clear that the RMSE gradually becomes smaller and smaller when the window size becomes bigger and bigger. After the window size 65*65, the RMSEs are smaller than previous ones. Fig.5.9 shows the effects of window sizes on the SPD of interferograms. It is noticed that the SPD is becoming smaller when the window size increases. When the window size is 65*65, the SPD is the smallest. It means the quality of interferogram generated with window size 65*65 is the best. Although almost all the SPDs are small after 65, they are still larger than the SPD when the window size is 65*65. This may mean that substantially large window size does not necessarily result in good interferogram. Specially, when window size is 97*97, its RMSE is the smallest, but its SPD is not so.

From the results of experiment, it is seen that the effects of window sizes on the quality of interferogram is non-linear. Obviously, when window size is 65*65, the SPD is the smallest. The resultant interferogram is the best. It seems to say that 65*65 is likely to be the optimum window size for tiepoint matching in this image.

5.4.4 Effects of window sizes on the accuracy of DEM

The final product of InSAR image processing is DEM. Its accuracy is indicated by RMS error, δ_{DEM}. In order to get it, the reference DEM for the same area is used and shown in Fig.5.10. All of the DEM images corresponding to the different window sizes are shown in Fig.5.11. The effect of window size on the accuracy of DEM can be measured by δ_{DEM}. If the δ_{DEM} is small, it proves the window size is good. Otherwise, the window size is bad. The results on δ_{DEM} are included in Table 5.3.

For the DEM image in Fig.5.11.a, the window size is 17*17, the δ_{DEM} is 23.6 meters and it is the largest among all. Its DEM accuracy is the worst among all. For the DEM image in Fig.5.11.b, the window size is 33*33, the δ_{DEM} is 23.1 meters next to the largest. The accuracy of DEM is next to the worst. For the DEM image in Fig.5.11.c, the window size is 49*49. The δ_{DEM} is 22.7 meters, which is large. Its DEM accuracy is bad. For the DEM image in Fig.5.11.d, the window size is 65*65. The δ_{DEM} is, 21.1 meters, the smallest. The accuracy of DEM is the best among all. For the DEM image in Fig.5.11.e, the window size is 81*81, the δ_{DEM} is 21.9 meters, the second smallest. Its DEM accuracy is the second best. For the DEM image in Fig.5.11.f, the window size is 97*97. The δ_{DEM} is 22.9 meters, which is large. The accuracy of DEM is bad. For the DEM image in Fig.5.11.g, the window size is 113*113. The δ_{DEM} is, 22.8 meters, small. Its DEM accuracy is not bad.

Table 5.3 Data of DEMs generated by different window sizes

Window size (pixel)	DEM image	δ_{DEM} (m)
17*17	Figure 5.11.a	23.6
33*33	Figure 5.11.b	23.1
49*49	Figure 5.11.c	22.7
65*65	Figure 5.11.d	21.1
81*81	Figure 5.11.e	21.9
97*97	Figure 5.11.f	22.9
113*113	Figure 5.11.g	22.8

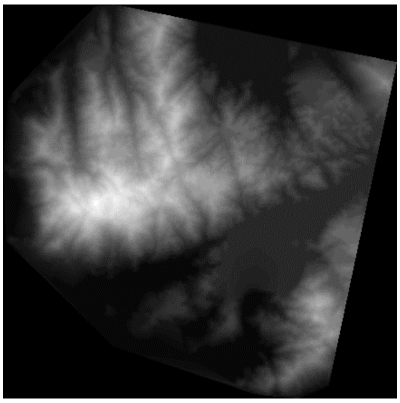

Figure 5.10 Reference DEM

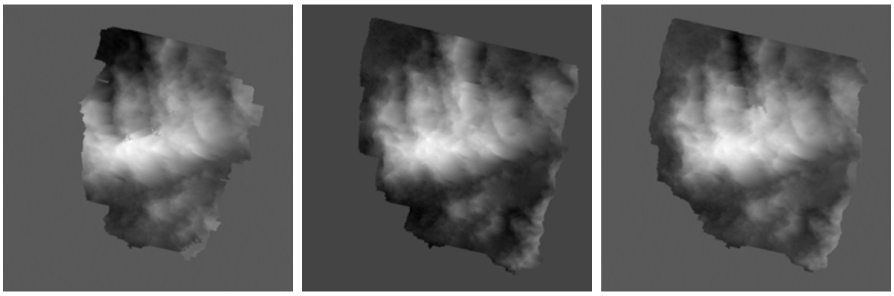

a. window size: 17*17; b. window size: 33*33; c. window size: 49*49

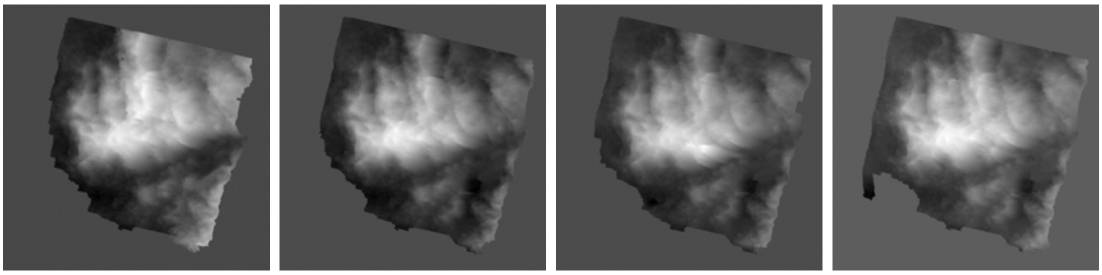

d. window size: 65*65; e. window size: 81*81; f. window size: 97*97; g. window size: 113*113

Fig.5.11 DEMs with different window sizes

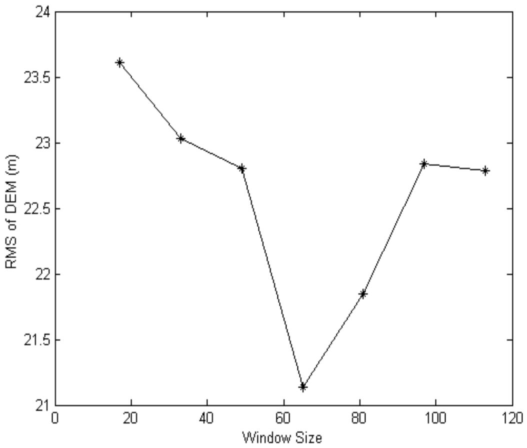

Fig.5.12 Effects of window sizes on the δ_{DEM}

The effects of window sizes on the accuracy of DEMs are shown in Fig.5.12. The accuracy of DEM is becoming better when the window size is increasing from 17*17 to 65*65. When the window size is 65*65, its corresponding DEM accuracy is the best. It is noticed that from 65 on, almost all the δ_{DEM} s are small. In spite of this, the δ_{DEM} s for window size 81*81, 97*97 and 113*113 are still larger than the one for window size 65*65. This perhaps means that very big window size does not necessarily result in accurate DEM. From the results, it might say that 65*65 may be the optimum window size for tiepoints matching.

From the experimental results, it is seen that when the window size is 65*65, the quality of interferogram and the accuracy of DEM are the best among all. Therefore, 65*65 is the optimum window size for tiepoint matching with this image. Obviously, the optimum window size can be determined based on decomposing the autocorrelation coefficient of SAR image by wavelet.

5.5 Summary

In SAR image interferometry, the quality of InSAR products can be influenced by many factors. One of them is window size, which must be considered during tiepoint matching in co-registration. The aim of this chapter is to determine the optimum window size for tiepoint matching. With an analysis of the characteristics of autocorrelation, an approach on determining optimum window size is proposed based on decomposing the autocorrelation coefficient with wavelet.

In order to prove the efficacy of the method, a set of experiment has been conducted. A pair of SAR images with a size of 1760*400 has been adopted in the experiment. The first step is to calculate the autocorrelation coefficient of the image. From the variation of autocorrelation, it is noticed that the autocorrelation becomes smaller when the distance becomes bigger.

Then, the autocorrelation was decomposed into two parts with wavelet db1. One is high frequency components including d1, d2, d3 and d4 while another one is low frequency component a4. The low frequency component expresses the varying trend of autocorrelation. The corresponding high frequency component expresses the local variation. The amplitude of a4 changes at several points in the distance axis. After point 65, the amplitude has very little changes. So 65*65 could be the optimum window size for tiepoint matching. For a more reliable result, the others are also used as window sizes. Totally, seven window sizes, 17*17, 33*33, 49*49, 65*65, 81*81, 97*97, 113*113, have been adopted for the experiments.

The effects of window sizes on the quality of interferogram and the accuracy of DEM are non-linear. From the analysis, it is shown that the quality of interferogram and the accuracy of DEM are best when the window size is 65*65. Therefore, 65*65 is the optimum window size for tiepoint matching with this SAR image. It proves that the optimum window size could be determined based on decomposing autocorrelation by wavelet.

From the analysis and experimental tests about the proposed approach on determining optimum window size for tiepoint matching, the follows can be concluded:

(1) The low frequency component of decomposed autocorrelation coefficient expresses the overall trend of autocorrelation. The high frequency component

expresses the local variation of the signal. The amplitudes corresponding to low and high frequency component have jumping points in the distance axis. After a certain distance, the amplitude has very little changes. Therefore, this distance value could be the optimum window size. For different image, the optimum window size could be different.

(2) The quality of product of InSAR is affected by the window size. Too large window size does not necessarily result in good results.

(3) It can be a reliable method to determine the optimum window size based on decomposing autocorrelation coefficient by wavelet.

Chapter 6

Extracting feature points for Co-registration based on wavelet

In image co-registration, a set of tiepoints is selected for tiepoint matching. Due to lack of well-defined points, the nodes of grids are normally selected as tiepoints for co-registration as described in chapter 4. However, if feature points could be detected in the image, it will benefit the co-registration. This chapter aims to extract feature points from SAR image based on wavelet to improve the accuracy of image co-registration of SAR interferometry.

6.1 Introduction

If feature points evenly distributes in the image, the co-registration based on these feature points would be more reliable. Two steps are involved in the procedure of feature point matching, extraction of feature points and feature point matching.

Some methods have been used to extract feature points from image. One of the methods is Interest Operators (Urban, 2003). This method is based on the maximum gradient to extract feature points. However, each pixel gradient is calculated in the original image. Therefore, too much calculation is needed. Wavelet can also be used to extract feature points from image (Moigne et al., 2002). This method is based on maximum wavelet gradient modular. Compared with Interest Operators, by wavelet, the wavelet gradient is implemented not in the original image but at the highest level. The feature points are extracted at the highest level. It, therefore, avoids a lot of calculation.

Wavelets support a multiresolution analysis of images. It could reduce the computation cost by initially registering images at lowest resolution and then proceeding to higher resolution where the co-registration process is refined. Wavelet decomposition provides all image features without duplication or loss of information and allows preserving all the important characteristics of the original data even at a lower resolution. Also, the properties of the wavelet coefficients after low-pass and high-pass filters prove to be very useful in extracting characteristic features of the image (Louis et al., 1997), and therefore to perform a detection of the tiepoints with features.

In short, the choice of using multiresolution wavelet to detect feature points for co-registration is justified by the following reasons:

a. Traditionally, the feature points refer to the points, such as houses, intersection of roads and islands. Normally, these kinds of feature points could not always be found in SAR image. Thus, the connotation of feature points should be enlarged. In the study, the feature points are defined in wavelet domain.
b. Most of all, multiresolution wavelet decomposition preserves important features of the original data, even at a lower resolution.
c. Further multiresolution wavelet decomposition highlights strong image features at the lower resolution, thus eliminating weak higher resolution

features.

d. Compared with other methods, this algorithm achieves higher accuracies with higher speeds than a full search at full resolution.

6.2 Principle of extracting feature points in image with wavelet

6.2.1 Wavelet transform modulus maxima

The analysis of images could be implemented by 2-D wavelet multiresolution analysis. In a 2-D space, if function $\psi(x,y) \in L^2(R^2)$ satisfies:

$$\iint_{R^2} \psi(x,y)dxdy = 0 \tag{6.1}$$

it is called a 2-D basic wavelet or “mother wavelet”. The continuous 2-D wavelet transform of a function $f(x,y) \in L^2(R^2)$ is given by the convolution

$$w_a[f(x,y)] = \iint_{R^2} f(x,y)\psi_{a,b}(x,y)dxdy = f * \psi_a(x,y) \tag{6.2}$$

The wavelet can be interpreted as the impulsive response of a band-pass filter and the wavelet transform of a function as a convolution of this function with the dilated filter. Thus the processing can be done at different scales or resolutions. If we look at the data with a large “window” (large a), we notice gross features. Similarly, if we look at the data with a small “window” (small a), we notice small features. Considering wavelet transform carried out with computer, in practice, the scale a has to be discretized. For a particular class of wavelets, the scale a can be sampled along a dyadic sequence $a = 2^j$ with $j \in Z$, without modifying the overall properties of the transform. The transforms corresponding to dyadic values of a are called discrete wavelet transform (DWT),

$$w_{2^j}[f(x,y)] = f * \psi_{2^j}(x,y) \tag{6.3}$$

Therefore, an image could be regarded as a function $f(x,y)$ and its discrete wavelet transform could be carried out according to the above description. In order to extract the feature points from the image, the understanding of wavelet transform modulus is needed.

Let $\theta(x,y)$ is a 2-D smooth function. The first order derivative of $\theta(x,y)$ decomposed into two components along the x and y directions, respectively, are

$$\psi^1(x,y) = \frac{\partial\theta(x,y)}{\partial x} \tag{6.4a}$$

$$\psi^2(x,y) = \frac{\partial\theta(x,y)}{\partial y} \tag{6.4b}$$

These functions can be used as wavelets. At scale $a = 2^j$, the 2-D wavelet transform of an image $f(x,y)$ can be decomposed into two independent directions as:

$$w^1_{2^j}[f(x,y)] = f * \psi^1_{2^j}(x,y) \tag{6.5a}$$

$$w^2_{2^j}[f(x,y)] = f * \psi^2_{2^j}(x,y) \tag{6.5b}$$

Basically, these two components are proportional to the coordinates of the gradient vector of $f(x,y)$ smoothed by $\theta(x,y)$ at scale 2^j in x and y directions.

At a scale 2^j, the modulus of the gradient vector of $f(x,y)$ can be calculated by:

$$M_{2^j}[f(x,y)] = \sqrt{\left|w^1_{2^j}[f(x,y)]\right|^2 + \left|w^2_{2^j}[f(x,y)]\right|^2} \tag{6.6}$$

At each scale 2^j, the modulus maxima of the wavelet transform is defined as points (x, y) where the modulus $M_{2^j}[f(x,y)]$ is local maximum along the gradient direction.

6.2.2 Extraction of feature points with wavelet threshold

A threshold procedure is applied to the wavelet transform modulus in order to eliminate non-significant feature points. Then, a point (x, y) is recorded only if

$$M_{2^j}[f(x,y)] > \lambda_{2^j} \tag{6.7}$$

where, $\lambda_{2^j} = \alpha(\delta_{2^j} + \mu_{2^j})$. δ_{2^j} and μ_{2^j} are the standard deviation and mean of the wavelet gradient modulus at level 2^j, respectively; α is a constant and normally selected as 2 (Fonseca and Costa, 1997). λ_{2^j}, a parameter whose initial value could be defined by user according to the demand. The parameter λ_{2^j} controls the number of feature points to be used for tiepoints matching. Since the number of feature points increases in the finer resolutions, the parameter λ_{2^j} is also increased at the higher levels in order to extract the most significant feature points in the images.

6.3 Procedures for extracting feature points with wavelet

6.3.1 Outline of the procedure

To test the adequacy of wavelet as a more reliable method for SAR image co-registration, a series of experiments should be conducted. The co-registration process consists of three steps: decomposing images, extracting feature points and matching feature points.

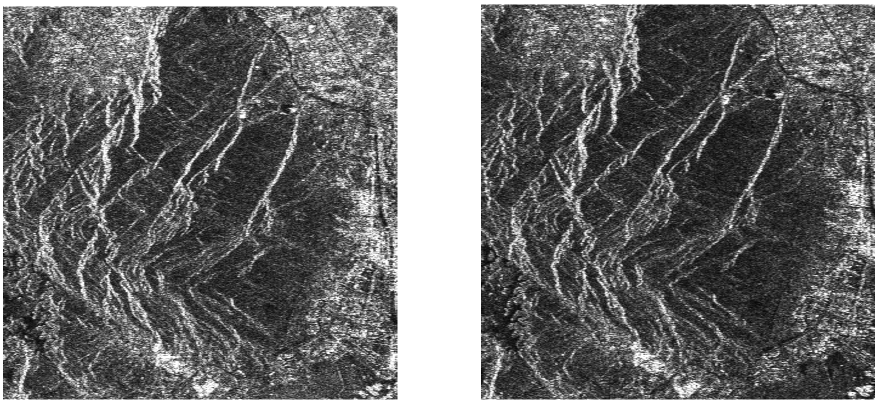

The master image The slave image

Fig.6.1 The pair of SAR complex images of Tuen Mun in Hong Kong

In order to conduct the experiments, a pair of SAR complex images of Tuen Mun in

Hong Kong is adopted, as shown in Fig.6.1. First of all, the wavelet decomposition is used to decompose the images at different levels. Totally, there are 3 levels of wavelet decomposition of images in the experiments. Once the extraction of feature points and the initial co-registration have been carried out at the lowest level as described later, the fine co-registration would be realized at the higher levels.

The results of co-registration based on wavelet method and the one based on general method should be compared to see whether the proposed method is capable of improving the reliability and accuracy of co-registration. A series of different numbers of tiepoints has been conducted for the experiments. The number of tiepoints varies from 36 to 81. For the comparability of results, the same number of points for co-registration is used in the two methods. That is, for 36 tiepoints in grid form used in general method, the same number of feature points, 36 points extracted based on wavelet is also used in wavelet method. It is the same strategy for other different number of tiepoints, 49, 64 and 81. Based on these points, a series of co-registrations could be carried out and their results corresponding to the two methods are compared.

The results of InSAR image processing include two parts: the intermediate product interferogram and the final product DEM. The measures for the reliability of co-registration include two components: one measure is for the quality of interferogram; another measure is for the accuracy of DEM. The quality of interferogram is quantitatively measured by its SPD calculated by the formula (3.1), as shown in chapter 3. The accuracy of DEM is measured by its δ_{DEM} calculated with formula (4.1), as shown in chapter 4. For this calculation, the reference DEM of the same area is used and its accuracy is about 3 meters.

6.3.2 Decomposition of SAR image with wavelet

In order to extract feature points from SAR image, first of all, the SAR image should be decomposed at different levels. With the goal of SAR image co-registration as an application of the wavelet decomposition performed in computer, discrete wavelet is only considered and it is summarized in Fig.6.2. It is noticed that the original SAR image (or previous low-pass results at level j) could be decomposed into low-pass component (L_{j+1}) and high-pass component (H_{j+1}) through filters at level $j+1$. Through low-pass filter and high-pass filter, the low-pass component (L_{j+1}) is decomposed into low-pass component (LL_{j+1}) and high-pass component (LH_{j+1}) again. The high-pass component (H_{j+1}) is decomposed into low-pass component (HL_{j+1}) and high-pass component (HH_{j+1}) through filters. LH_{j+1}, HL_{j+1} and HH_{j+1}, respectively represent the characteristics of image in horizon, vertical and diagonal. The basic energy of image is reserved in LL_{j+1}. We will refer to the four subimages created at each level of decomposition as LL_{j+1} (Low/Low), LH_{j+1} (Low/High), HL_{j+1} (High/Low) and HH_{j+1} (High/High). An image is decomposed into four subimages at each level. The pyramid structure of decomposing an image with wavelet is shown in Fig.6.3. The SAR image has been decomposed as shown in Fig.6.4. This is the preparation for next step of feature point extraction.

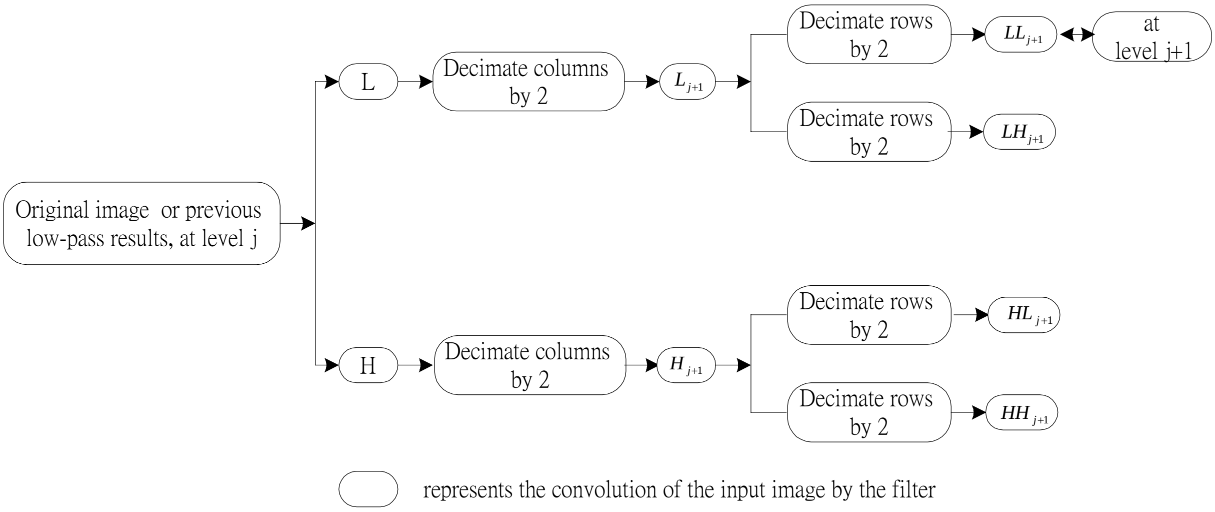

Fig.6.2 Block chart of wavelet decomposition of an image

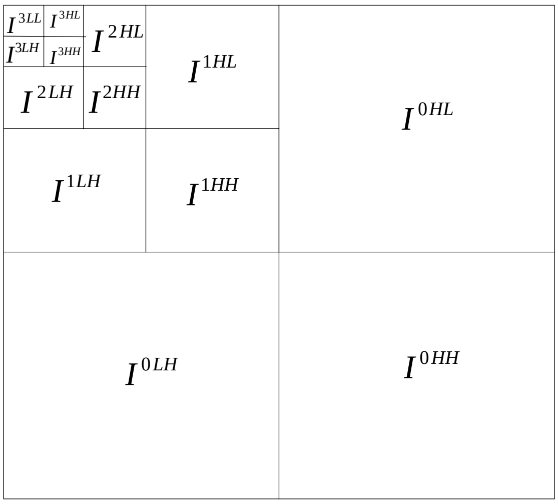

Fig.6.3 The pyramid structure of decomposing an image

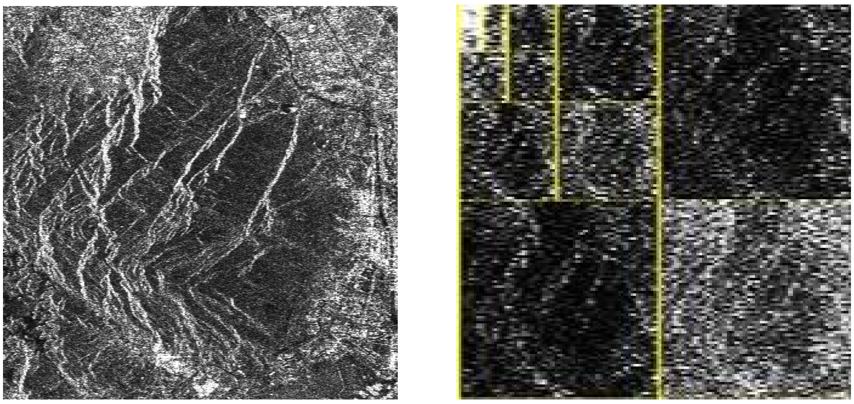

a. Original SAR image b. Decomposition of SAR image

Fig.6.4 Decomposition of a SAR image with wavelet

6.3.3 Extraction of feature points

Once the SAR images have been decomposed at each level, the next step aims to identify features that are present in both images at each level of the decomposition. Here we use the modulus maxima of the wavelet transform to detect sharp variation points according to the strategy described in previous section. The LH and HL subimages at each level of the wavelet transform are used to estimate the image gradient.

At the lowest level, the parameter λ_{2^j} is set to a value as the threshold for detecting sharp variation points. Every point's wavelet transform gradient modulus could be calculated according to the formula (6.6). With the set threshold λ_{2^j}, the points with modulus maxima are extracted as feature points.

Different numbers of tiepoints, namely 36, 49, 64 and 81, are adopted in the experiments. For the general method, the tiepoints are selected as the nodes in grid form. In order to compare the different distribution of points in these two situations, the points are displayed in the original SAR images. The distributions of grid points and feature points in the original SAR images are shown in Fig.6.5 and Fig.6.6, respectively.

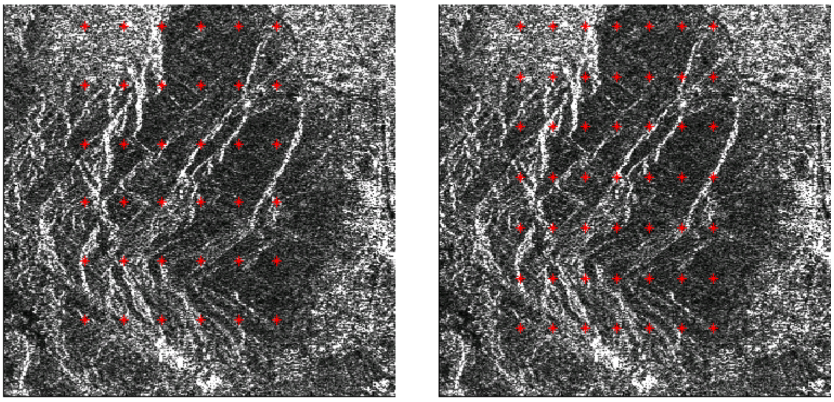

a. Number of grid points: 36　　b. Number of grid points: 49

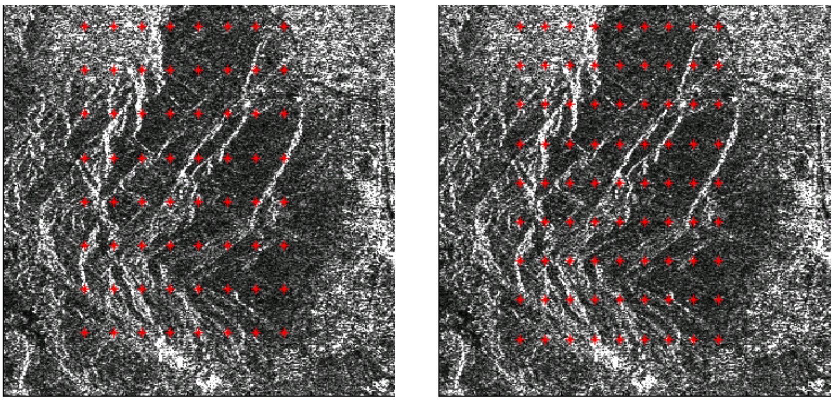

c. Number of grid points: 64　　d. Number of grid points: 81

Fig.6.5 Distribution of grid points

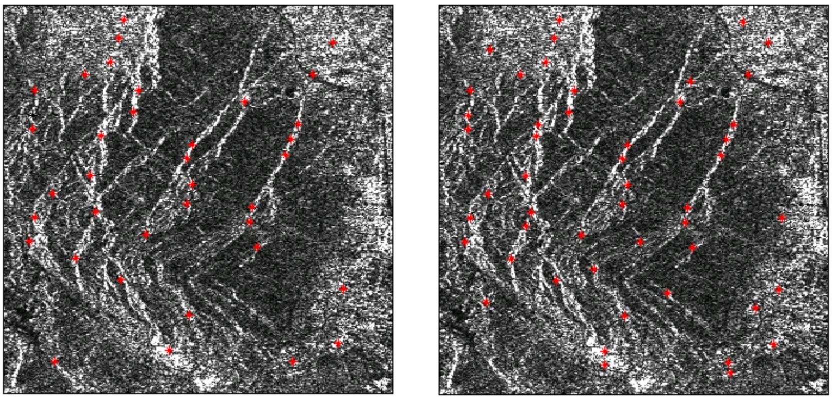

a. Number of feature points: 36

b. Number of feature points: 49

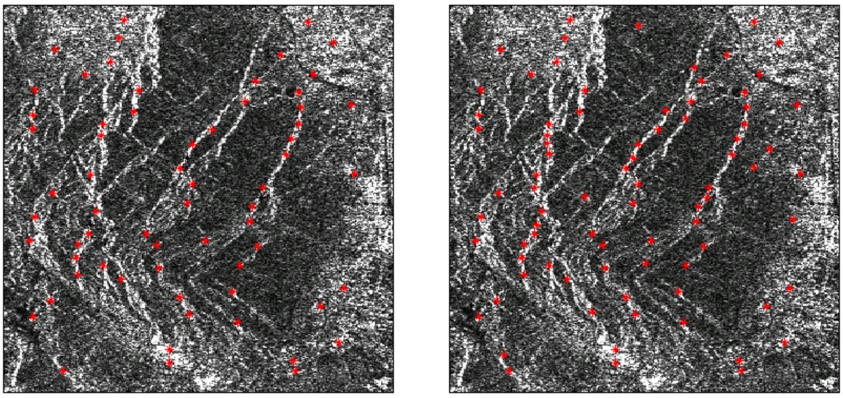

c. Number of feature points: 64

d. Number of feature points: 81

Fig.6.6 Distribution of feature points extracted by wavelet

From Fig.6.5 and Fig.6.6, it is noticed that teipoints are evenly distributed in each image whether they are selected in grid form or extracted by wavelet. In Fig.6.5, the tiepoints are distributed with a certain interval. Of course, many of them have no significant features. Contrastively, in Fig.6.6, it is noticed many of the feature points are positioned in the mountain back. All of the feature points with wavelet gradient maxima have significant features relative to the tiepoints selected in grid form.

Once the feature points have been extracted, the next step is feature point matching. Feature point matching is performed within the LL subimage of the wavelet decomposition from the lowest level to higher level. It is achieved based on the cross-correlation coefficient maximization as described previously.

6.4 Improvement of the co-registration with feature points

6.4.1 Improvement in the quality of interferograms

Certainly, the quality of interferogram is measured by the SPD. When the SPD is small, it means the interferogram is good. The data of SPD are included in Table 6.1.

Table 6.1 Data of interferograms generated based on different type of points

Number of tiepoint	Data general based on grid points				Data generated based on feature points			
	Distribution of grid points	Interferogram	RMSE (pixel)	SPD (radian)	Distribution of feature points	Interferogram	RMSE (pixel)	SPD (radian)
36	Fig.6.5a	Fig.6.7a	0.0572	41,946	Fig.6.6a	Fig.6.8a	0.0486	41,390
49	Fig.6.5b	Fig.6.7b	0.0731	44,082	Fig.6.6b	Fig.6.8b	0.0476	41,083
64	Fig.6.5c	Fig.6.7c	0.0551	40,863	Fig.6.6c	Fig.6.8c	0.0499	40,081
81	Fig.6.5d	Fig.6.7d	0.0684	42,867	Fig.6.6d	Fig.6.8d	0.0547	40,807

The interferograms, in Fig.6.7, are generated based on the grid points. The interferograms, in Fig.6.8, are generated based on the feature points. When the number of tiepoints is 36, for interferogram in Fig.6.7a, its SPD is 41,946 radians. For Fig.6.8a, the fringes of interferogram, especially in the low right area, are clearer than the ones in Fig.6.7a visually. Its SPD is 41,390 radians smaller than that of the interferogram in Fig.6.7a.

When the number of tiepoints is 49, for interferogram in Fig.6.7b, its SPD is 44,082 radians. For Fig.6.8b, it is obvious that the fringes of interferogram, especially on the right side, are clearer than the ones in Fig.6.7b visually. The SPD is 41,083 radians smaller than that of the interferogram in Fig.6.7b.

When the number of tiepoints is 64, for interferogram in Fig.6.7c, its SPD is 40,863 radians. For the interferogram in Fig.6.8c, its SPD is 40,081 radians smaller than that of the interferogram in Fig.6.7c.

When the number of tiepoints is 81, for interferogram in Fig.6.7d, its SPD is 42,867 radians. For Fig.6.8d, it is obvious that the fringes of interferogram, especially on the right part, are clearer than the ones in Fig.6.7d visually. The SPD is 40,807 radians smaller than that of the interferogram in Fig.6.7b.

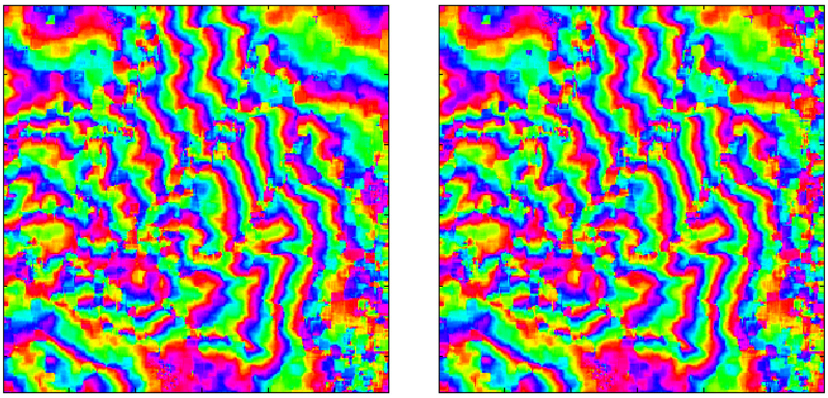
a. Number of grid points: 36

b. Number of grid points: 49

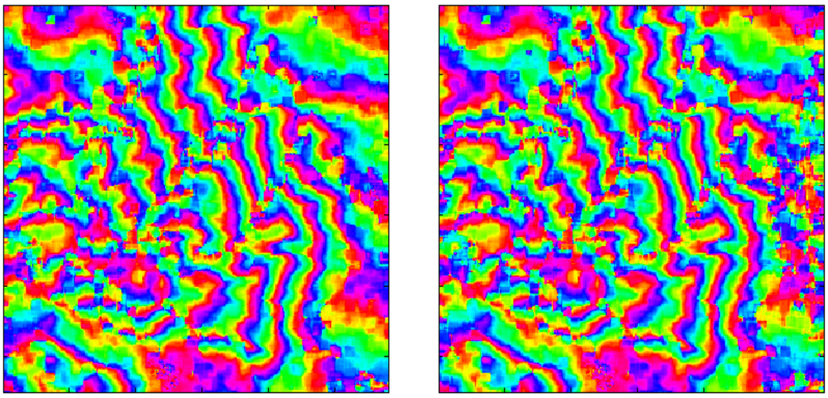

c. Number of grid points: 64

d. Number of grid points: 81

Fig.6.7 Interferograms corresponding to different numbers of grid points

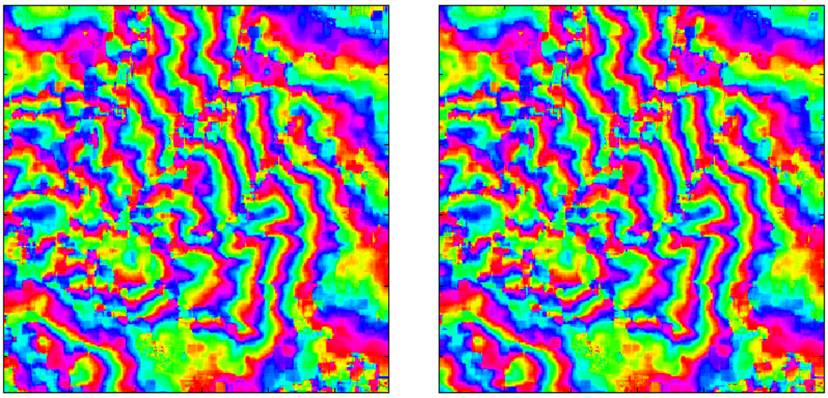

a. Number of feature points: 36

b. Number of feature points: 49

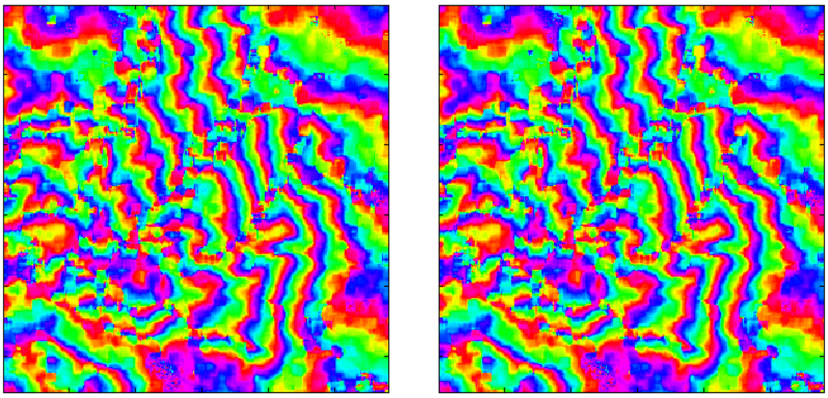

c. Number of feature points: 64

d. Number of feature points: 81

Fig.6.8 Interferograms corresponding to different numbers of feature points

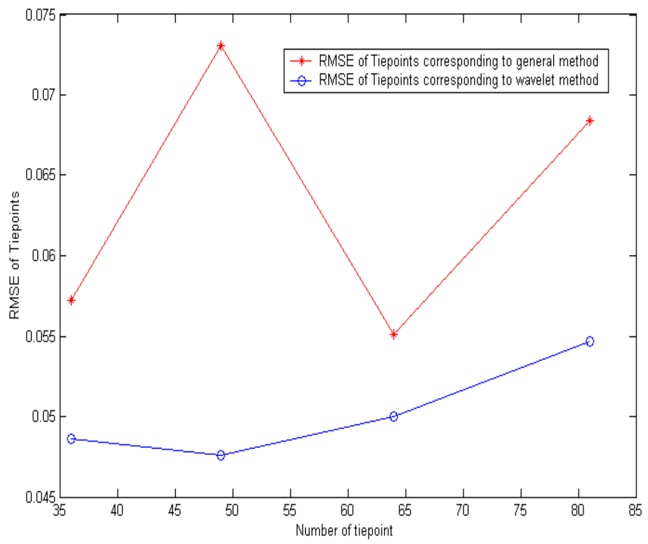

Fig.6.9 Variation of RMSE of tiepoints

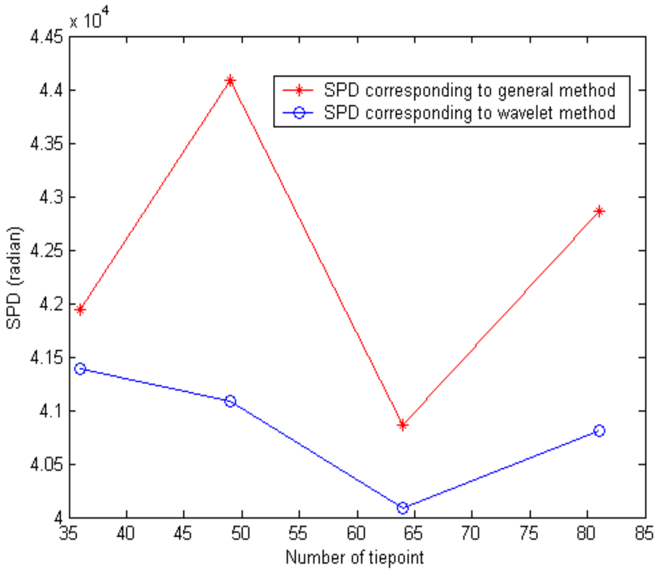

Fig.6.10 Variation of SPD with tiepoints

The variations of RMSE of tiepoints and the SPD of interferograms are shown in Fig.6.9 and Fig.6.10, respectively. From the figure, it is noticed that the SPD of interferogram generated by feature points is smaller than that generated by grid points. This indicates, therefore, that the quality of interferogram generated by the feature points is better than the one generated by grid points.

6.4.2 Improvement in the accuracy of DEM

In order to measure the accuracy of DEM, the reference DEM is used, as shown in Fig.6.11. Corresponding to different tiepoints, all of the DEM images generated based on grid points and feature points are respectively shown in Fig.6.12 and Fig.6.13. The data of δ_{DEM} are included in Table 6.2.

Table 6.2 Data of DEM generated based on different type of points

Number of tiepoint	Data generated based on grid points		Data generated based on feature points		Improved $\Delta\delta_{DEM}$ (%)
	δ_{DEM_G} (m)	DEM images	δ_{DEM_W} (m)	DEM images	
36	19	Fig.6.12a	16	Fig.6.13a	16
49	23	Fig.6.12b	15	Fig.6.13b	34
64	17	Fig.6.12c	12	Fig.6.13c	29
81	20	Fig.6.12d	13	Fig.6.13d	35

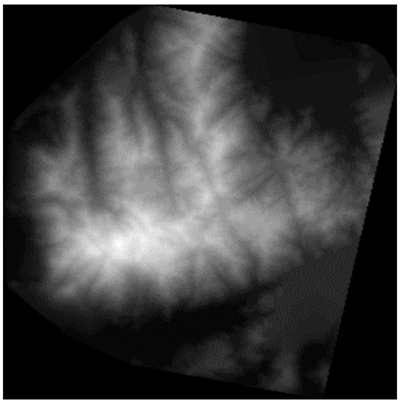

Fig.6.11 Reference DEM image

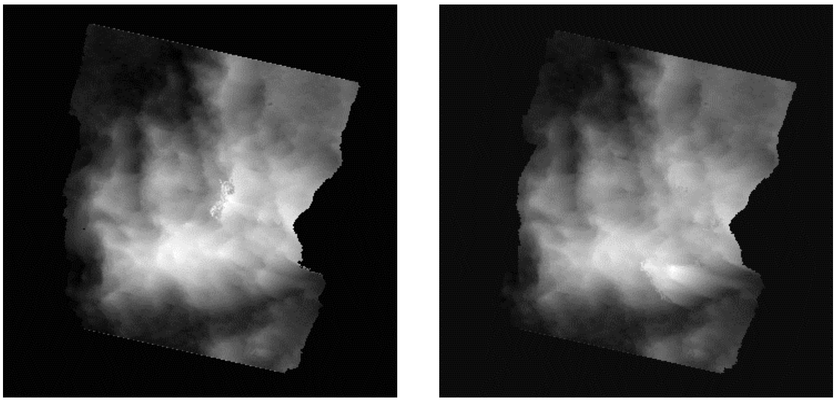

a. Number of grid points: 36 b. Number of grid points: 49

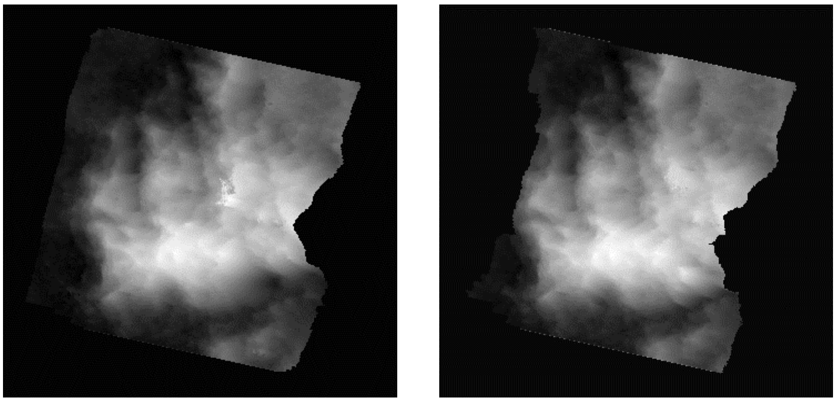

c. Number of grid points: 64 d. Number of grid points: 81

Fig.6.12 DEM images corresponding to different numbers of grid points

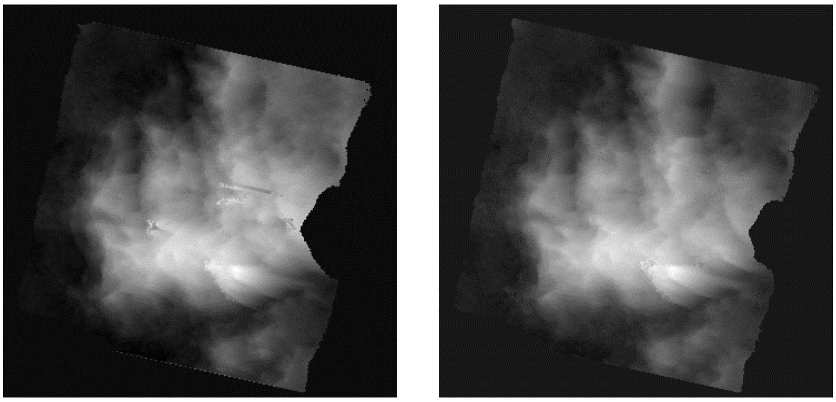

a. Number of feature points: 36 b. Number of feature points: 49

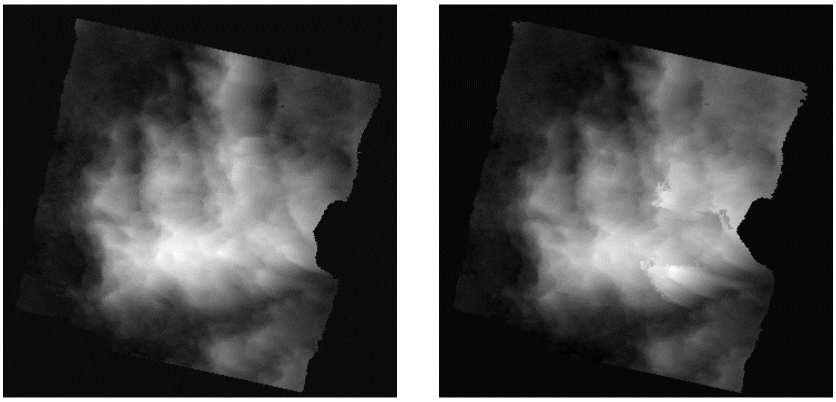

c. Number of feature points: 64 d. Number of feature points: 81

Fig.6.13 DEM images corresponding to different numbers of feature points

The RMSE of DEM generated based on grid points is expressed by δ_{DEM_G} while that one generated based on feature points is expressed by δ_{DEM_F}. The data of the improved δ_{DEM} and $\Delta\delta_{DEM}$ are also included in the table to illustrate how much δ_{DEM} has improved when DEM is generated based on feature points. The $\Delta\delta_{DEM}$ is derived as:

$$\Delta\delta_{DEM} = (\delta_{DEM\_G} - \delta_{DEM\_F}) \ / \ \delta_{DEM\_G} \tag{6.8}$$

For DEM images in Fig.6.12a and Fig.6.13a, when the number of tiepoints is 36, the accuracy of DEM generated based on grid points is 19 meters, larger than the one, , generated based on feature points, which is 16 meters. The DEM’s accuracy has been improved by 16%.

For DEM images in Fig.6.12b and Fig.6.13b, when the number of tiepoints is 49, the accuracy of DEM generated based on grid points is 23 meters, which is larger than the one generated based on feature points (15 meters). The DEM's accuracy has been improved by 34%.

For DEM images in Fig.6.12c and Fig.6.13c, when the number of tiepoints is 64, the accuracy of DEM in Fig.6.12c is 17 meters. The accuracy of DEM in Fig.6.13c is 12 meters, smaller than the former one. Based on feature points, 29% is achieved for improving DEM's accuracy.

For DEM images in Fig.6.12d and Fig.6.13d, when the number of tiepoints is 81, the accuracy of DEM in Fig.6.12d is 20 meters. The accuracy of DEM in Fig.6.13d is 13 meters, which is smaller the former one. Based on feature points, the accuracy of DEM has been improved by 35%.

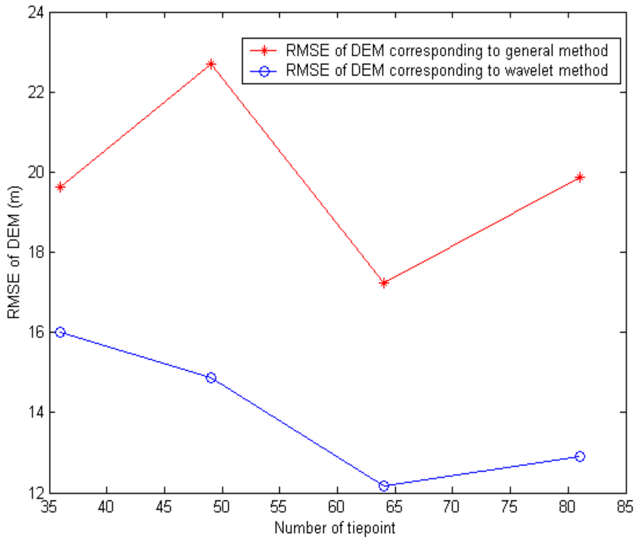

Fig.6.14 Variation of δ_{DEM} with tiepoints

The variations of δ_{DEM} with tiepoints are shown in Fig.6.14. From the curves, it is obvious that the accuracy of DEM generated based on feature points is more precise than that generated based on grid points.

From the results, it is noticed that both the quality of interferogram and the accuracy of DEM are improved with feature points. Therefore, it could be said that it is a reliable and efficient way for co-registration with feature points extracted by wavelet.

6.5 Improvement of the co-registration by the combined use of feature points and grid points

6.5.1 Design of experiment

In last section, it is noticed that the feature points extracted by wavelet are evenly distributed in the whole image. This makes the co-registration more reliable. However, the feature points are not always evenly distributed in the image. In some images, the feature points may be in cluster in a local area. In this case, if only these feature points are used, an unreliable co-registration may be obtained. So, combining the feature points and the grid points may be a more robust way for co-registration. Therefore, one more experiment based on combining feature points and grid points is employed for further investigation.

In order to compare the results generated by grid points and by combined points (feature points and grid points), the pair of SAR images adopted in the experiment is the same as the one in Fig.6.1. In the experiment, the co-registration is implemented based on the feature points and grid points, which consists of 36 feature points and 28 grid points. The distribution of points is shown in Fig.6.15 where red points are the feature points and the yellow points are the tiepoints. The tiepoint intervals, 200 pixels in row and 30 pixels in column, are considered when selecting the grid points.

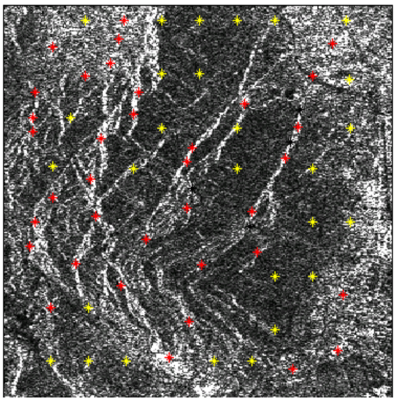

Fig.6.15 Distribution of points in an image

6.5.2 Improvement in the quality of interferogram

The co-registration is included in Table 6.3. The interferogram generated by combined use of feature points and grid points is shown in Fig.6.16. The interferogram generated by using grid points is shown in Fig.6.7c. Based on feature points and grid points, its RMSE is 0.0527 and SPD is 40,126 radians. For the results based on grid points only, its RMSE is 0.0551 and SPD is 40,863 radians.

From the interferogram, it is observed that the fringes in the interferogram, Fig.6.16, generated by feature points and grid points are clearer than those in the interferogram, Fig.6.7c, generated by grid points only.

Table 6.3 Data of co-registration generated by different types of points

Data Point type	Number of Point	RMSE (pixel)	Interferogram	SPD (radian)	DEM image	δ_{DEM} (m)	Improved $\Delta\delta_{DEM}$ (%)
Feature and grid point	64	0.0527	Fig 6.16	40,126	Fig.6.17	13	
Grid point	64	0.0551	Fig.6.7c	40,863	Fig.6.12c	17	24

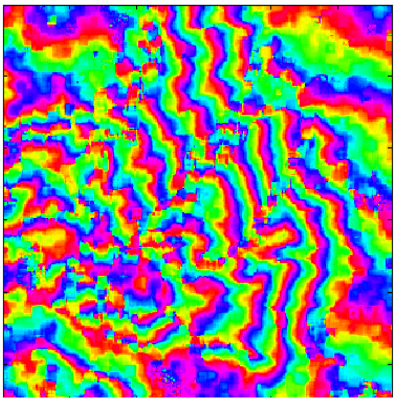

Fig.6.16 Interferogram generated by feature points and grid points

6.5.3 Improvement in the accuracy of DEM

In order to measure the accuracy of DEM, the reference DEM is used as shown in Fig.6.11. The DEM generated by combined use of feature points and grid points is shown in Fig.6.17.

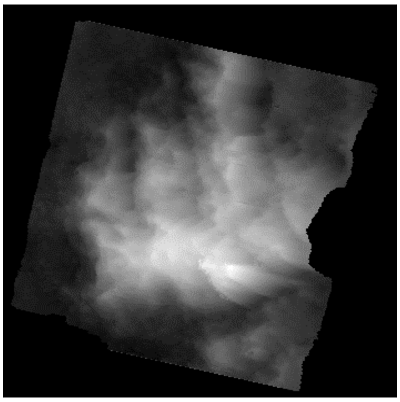

Fig.6.17 DEM generated based on feature points and grid points

The accuracy of DEM, δ_{DEM}, is 13 meters. For the results based on grid points only, its δ_{DEM} is 17 meters as shown in Table 6.3. Obviously, the accuracy of DEM is significantly improved, i.e. by 24%.

From the results, it can be seen that the reliability of co-registration is significantly improved by combined use of feature points and grid points.

6.6 Summary

This chapter presents the extraction of feature points for InSAR images co-registration based on wavelet. The feature points are extracted based on images decomposition and wavelet gradient modulus maximum. The feature point matching is done globally, instead of locally, over an image. A more reliable and accurate result of co-registration is achieved finally.

A pair of SAR images is used for proving the efficiency of the strategy based on wavelet. In the experiments, different number of points is employed to compare the quality of co-registration obtained by using grid points and feature points for getting more reliable findings. When the feature points are evenly distributed in the image, the SPD of interferogram generated based on feature points is smaller than that one generated based on grid points. By visual inspection, it is easily found the quality of interferogram is significantly improved by feature points. The accuracy of DEM is greatly improved by the use of feature points.

But in some cases, the feature points extracted by wavelet are not evenly distributed in the image, possibly in cluster. This could results in unreliable results of co-registration. In order to make the co-registration more reliable, the feature points extracted by wavelet and the grid points were combined together for a further experiment. The results generated by grid points and the results generated by combined use of feature points and grid points are compared and analyzed. From the experimental results and analysis, it is shown that combining the feature points and the grid points can make the co-registration more reliable and accurate.

In short, from the comparison and analysis of experimental results generated by the two methods, it is found that feature points can be effectively extracted from a SAR image based on wavelet and the reliability of co-registration can be significantly improved by the combined use of feature points and grid points.

Chapter 7

Toward automated system for image co-registration

In the previous chapters, many important factors involved in InSAR images processing are considered and the corresponding approaches to improve the accuracy of image co-registration are proposed. These proposed approaches include a quantitative measure for the quality of interferogram, an appropriate interval with around 200*30 pixels for tiepoint, determination of optimum window size for tiepoint matching, and extraction of feature points with wavelet. Each of them is considered for improving the reliability and the accuracy of InSAR image processing while other factors are kept unchanged. This chapter aims to realize an automated system for InSAR image co-registration by considering all factors synchronously through fusing all of the previous proposed approaches systematically and efficiently.

7.1 Concept of automated system for co-registration

It is well known that there are many factors affecting the reliability of InSAR image co-registration, such as selection of tiepoints, window size, etc. Each of the factors is considered in the procedures of InSAR image co-registration as described in previous chapters. The corresponding effective approaches are presented to improve the reliability of co-registration. Certainly, it is natural to think that all of the proposed approaches should be synchronously and systematically fused to make the image co-registration more reliable and automated. In order to implement an automated image co-registration, some important operators need to be considered. The automated system for image co-registration ($ASIP$) is as follows:

$$ASIP = (I, D, N, M, W, S, \delta) \tag{7.1}$$

where, I refers to automated decomposing an image based on wavelet; D is the operator of automated extracting feature points and grid points for co-registration; N refers to the number of points to be used for tiepoint matching; M is the automated operator to set a value about wavelet gradient threshold for selecting tiepoint; W refers to the automated operator to determine an optimum window size for tiepoint matching based on decomposing auto-correlation coefficient; S is the automated operator for measuring the quality of interferogram; and δ is the automated operator for measuring the accuracy of DEM.

It is clear that the system consists of seven operators. In this automated system, the SAR image is automatically decomposed with wavelet at first. Then, the automated extraction of feature points is to be carried out. If the feature points are not evenly distributed in the image, some grid points should be selected whose interval should be 200 pixels in row and 30 pixels in column. The next step is the automated determination of optimum window size. This is implemented based on decomposing the autocorrelation coefficient of image with wavelet. This is followed by the tiepoint matching. For a SAR image whose size is $Q * P$, its processing based on this system can be described by pseudo-code as shown in Fig.7.1.

```
Procedure $ASIP$
begin
        Decomposition operation to Images;
        t=0;
        while (n $\neq$ N) do
            for i=1 to k
            $M(t+1) = M(t) + \Delta$
            end for
        end while

        $W$ operation to Image;

        for i=1 to $Q * P$
            SPD calculation to Interferogram;
        end for

        for i=1 to $q$
            $\delta_{DEM}$ calculation to DEM;
        end for
end
```

Fig.7.1 The procedure of automated system described by pseudo-code

7.2 Automated SAR image co-registration

7.2.1 Automated decomposition of SAR images

The automated decomposition of images is the basic operator on which other operators are based. The SAR images are automatically decomposed with multiresolution wavelet decomposition and the wavelet ‘db1’ is adopted because of its powerful analysis. The size of SAR image of Po To Yan in Hong Kong is 1616*336 (pixels) as shown in Fig.7.2. Totally, three levels are achieved for decomposing the images with wavelet. It is illustrated in Fig.7.3. At each level, the image is decomposed into four sub-images, LH_{j+1}, HL_{j+1}, HH_{j+1}, and LL_{j+1}. These four sub-images respectively represent the characteristics of image in horizon, vertical, diagonal and basis.

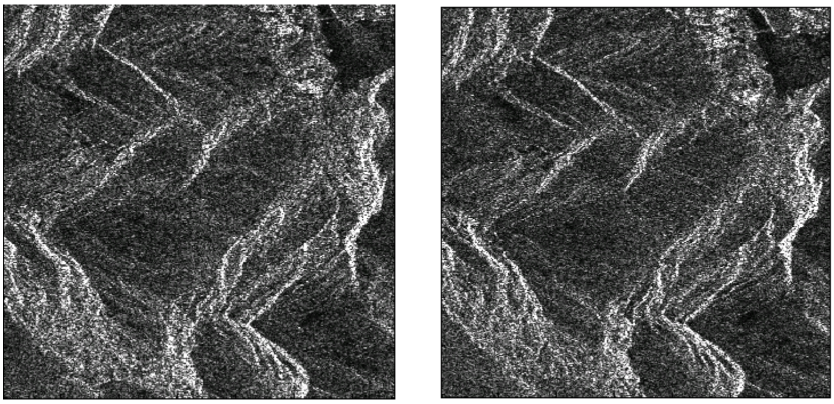

The master image The slave image

Fig.7.2 A pair of SAR images of Po To Yan in Hong Kong

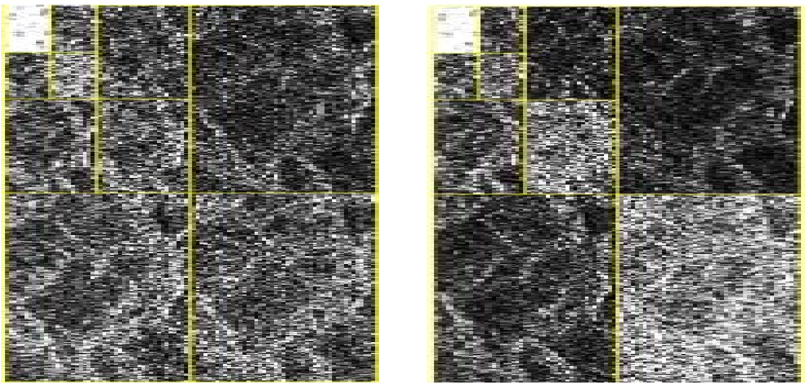

a. decomposition of master image b. decomposition of slave image

Fig.7.3 Decomposition of two images at level 3, respectively

7.2.2 Automated extraction of feature points

Once the image has been decomposed, the automated extraction of feature point could be done at the lowest level. The strategy based on wavelet transform gradient modulus maxima is used for extracting feature point. For each pixel, its gradient modulus could be derived with its gradient vectors in x and y directions. Then, the threshold value should be set to get the feature points. If the feature points extracted by wavelet are in a tight cluster, the grid points should be selected in order to get reliable co-registration. 64 tiepoints are adopted here and they are evenly distributed in the image. The points selected are displayed in the original image, shown in Fig.7.4.

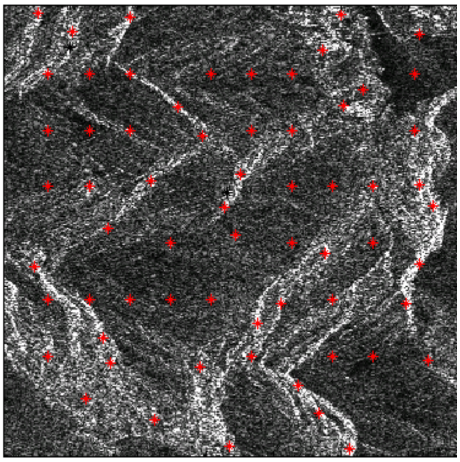

Fig.7.4 Distribution of tiepoints in the image

7.2.3 Automated determination of optimum window size

After the tiepoints have been selected, the next operation is the tiepoint matching. The window size is an important factor, which should be considered in tiepoint matching.

The optimum window size is automatically determined based on the decomposition of autocorrelation coefficient of the image. The details about the approach are described in chapter 5. Since the tiepoint matching is implemented from lower level to higher level, different window sizes should be used at different levels.

Firstly, we consider the window size at level 3. At this level, the main image is expressed by LL_2 which is inherited from level 2. The autocorrelation coefficient of this image is calculated with formula (5.1) and its curve is shown in Fig.7.5. With wavelet decomposition, the autocorrelation coefficient is decomposed into low frequency component, a_4 and high frequency components, d_4, d_3, d_2, d_1, as shown in Fig.7.6. The low frequency component a_4 has four changes of amplitude at distance points 17, 33, 49 and 65, respectively. The data of amplitude changes in low frequency component are included in Table 7.1.

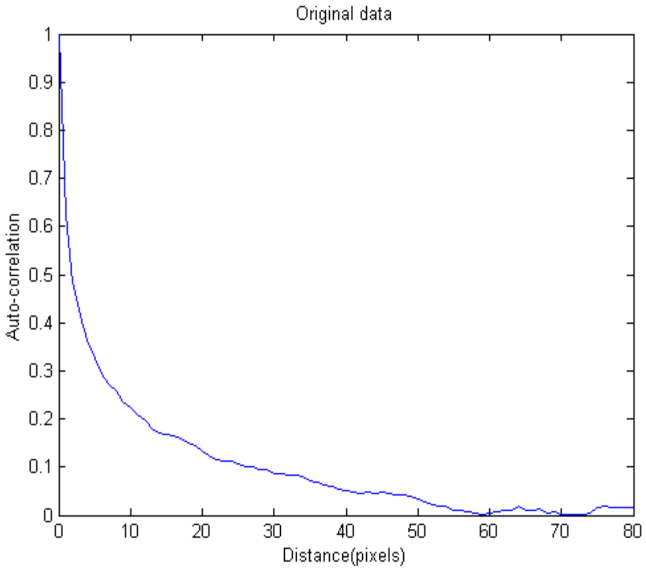

Fig.7.5 Variation of auto-correlation with distance at level 3

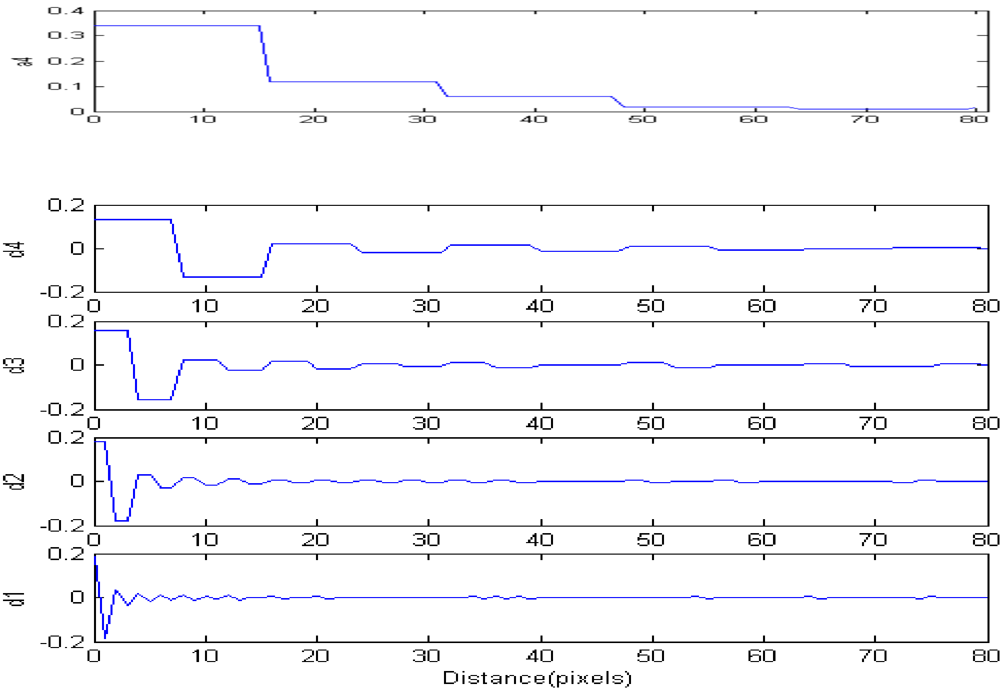

Fig.7.6 Components of auto-correlation decomposed by wavelet

Table 7.1 Amplitude data of low frequency component at level 3

Distance value at jump point	Amplitude at jump point	Amplitude rate	Changed amplitude rate
17	0.1177	34.71%	65.29%
33	0.0585	17.25%	17.46%
49	0.0171	5.04%	12.21%
65	0.0100	2.95%	2.09%

From Table 7.1, it is noticed that, at jump point 17, its amplitude is 0.1177. Its amplitude rate, the ratio between the amplitude in jump point and the whole amplitude 0.3391 is 34.71%. Its changed amplitude rate, the ratio between the changed amplitude at jump point and the whole amplitude is 65.29%. At jump point 33, its amplitude is 0.0585, its amplitude rate is 17.25% and its changed amplitude rate is 17.46%. At jump point 49, its amplitude is 0.0171, its amplitude rate is 5.04% and its changed amplitude is 12.21%. At jump point 65, its amplitude is 0.01, its amplitude rate is 2.95% and its changed amplitude rate is 2.09%. Obviously, from jump point 49 on, the amplitude rate is very small and the changed amplitude is also small. That is, after point 49, the amplitude is very small and almost remains the same. Therefore, the optimum window size should be 49*49 at level 3 for tiepoint matching.

Secondly, we consider the window size at level 2. It is similar to the procedures in level 3. At level 2, the variation of autocorrelation is shown in Fig.7.7. After decomposition with wavelet, its components include low frequency a_4 and high frequencies d_4, d_3, d_2, and d_1 as shown in Fig.7.8. The low frequency component a_4 has five obvious changes of amplitude at distance points 17, 33, 49, 65 and 81, respectively. The data of amplitude changes in low frequency component are included in Table 7.2.

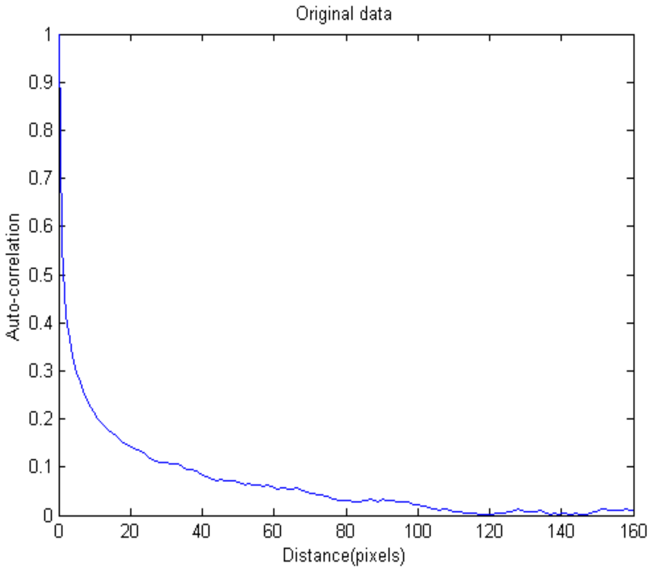

Fig.7.7 Variation of auto-correlation with distance at level 2

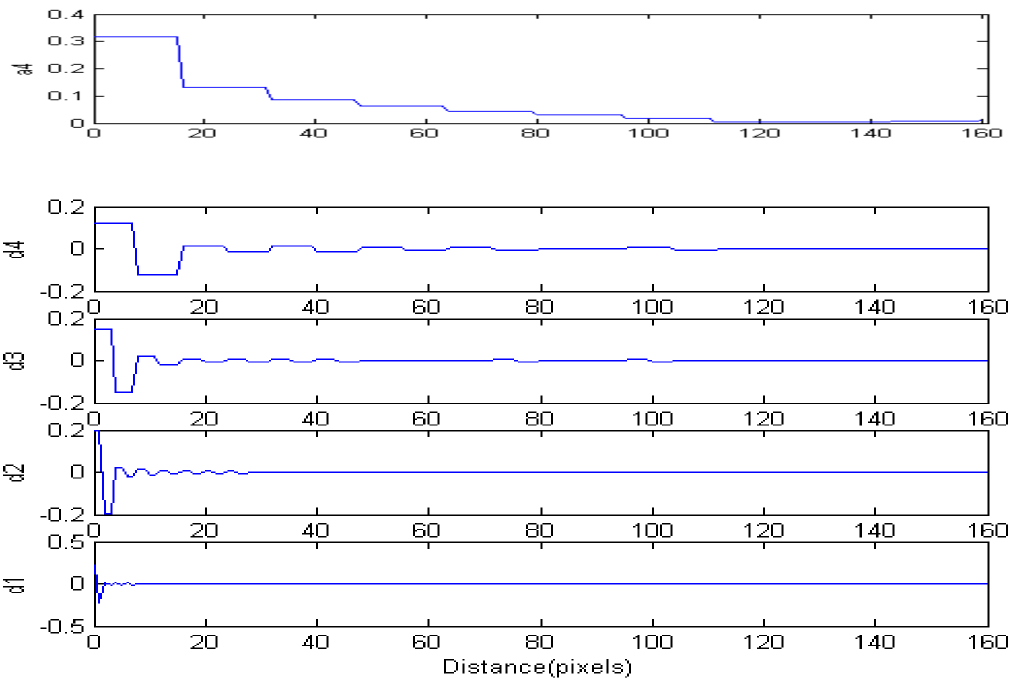

Fig.7.8 Components of auto-correlation decomposed by wavelet

Table 7.2 Amplitude data of low frequency component at level 2

Distance value at jump point	Amplitude at jump point	Amplitude rate	Changed amplitude rate
17	0.1301	40.86%	59.14%
33	0.0870	27.32%	13.54%
49	0.0623	19.57%	7.76%
65	0.0438	13.76%	5.81%
81	0.0300	9.42%	4.33%

Now we analyze the changes of amplitude in low frequency component a_4. The whole amplitude is 0.3148. At jump point 17, its amplitude is 0.1301. Its amplitude rate is 40.86%. Its changed amplitude is 59.14%. At jump point 33, its amplitude is 0.087, its amplitude rate is 27.32% and its changed amplitude rate is 13.54%. At jump point 49, its amplitude is 0.0623, its amplitude rate is 19.57% and its changed amplitude is 7.76%. At jump point 65, its amplitude is 0.0438, its amplitude rate is

13.76% and its changed amplitude rate is 5.81%. At jump point 81, its amplitude is 0.0300, its amplitude rate is 9.42% and its changed amplitude rate is 4.33%. Relatively, from jump point 33 on, the amplitude rate is small and the changed amplitude has little change. That is, after point 33, the amplitude is small and almost keeps the same. Therefore, the optimum window size should be 33*33 at level 2.

Finally, we consider the window size at the level 1. The strategy is the same as the previous two. The autocorrelation coefficient of image at level 1 is calculated and the variation with distance is shown in Fig.7.9. The autocorrelation coefficient is decomposed into two components including low frequency component a_4 and high frequency components d_4, d_3, d_2, and d_1 as shown in Fig.7.10. There are five obvious changes of amplitude in low frequency component. They are at distance points 17, 33, 49, 65 and 81, respectively. The data about amplitude changes in low frequency component are included in Table 7.3.

Table 7.3 Amplitude data of low frequency component at level 1

Distance value at jump point	Amplitude at jump point	Amplitude rate	Changed amplitude rate
17	0.1284	43.41%	56.59%
33	0.0935	31.61%	11.80%
49	0.0733	24.78%	6.83%
65	0.0629	21.26%	3.52%
81	0.0490	16.57%	4.70%

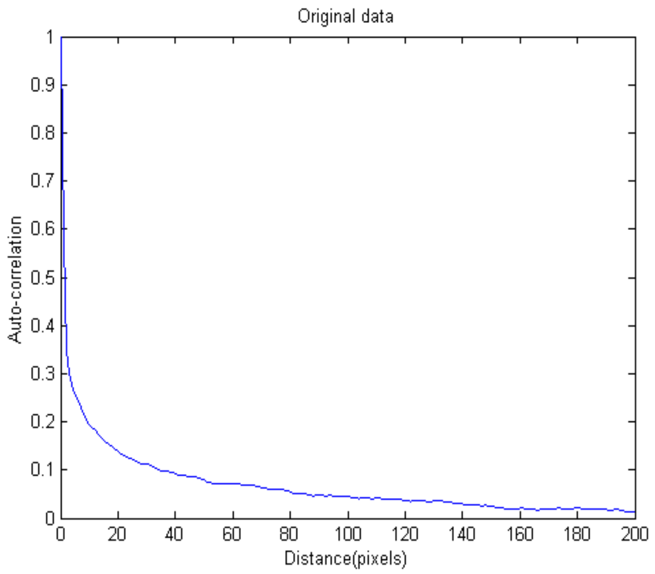

Fig.7.9 Variation of auto-correlation with distance at level 1

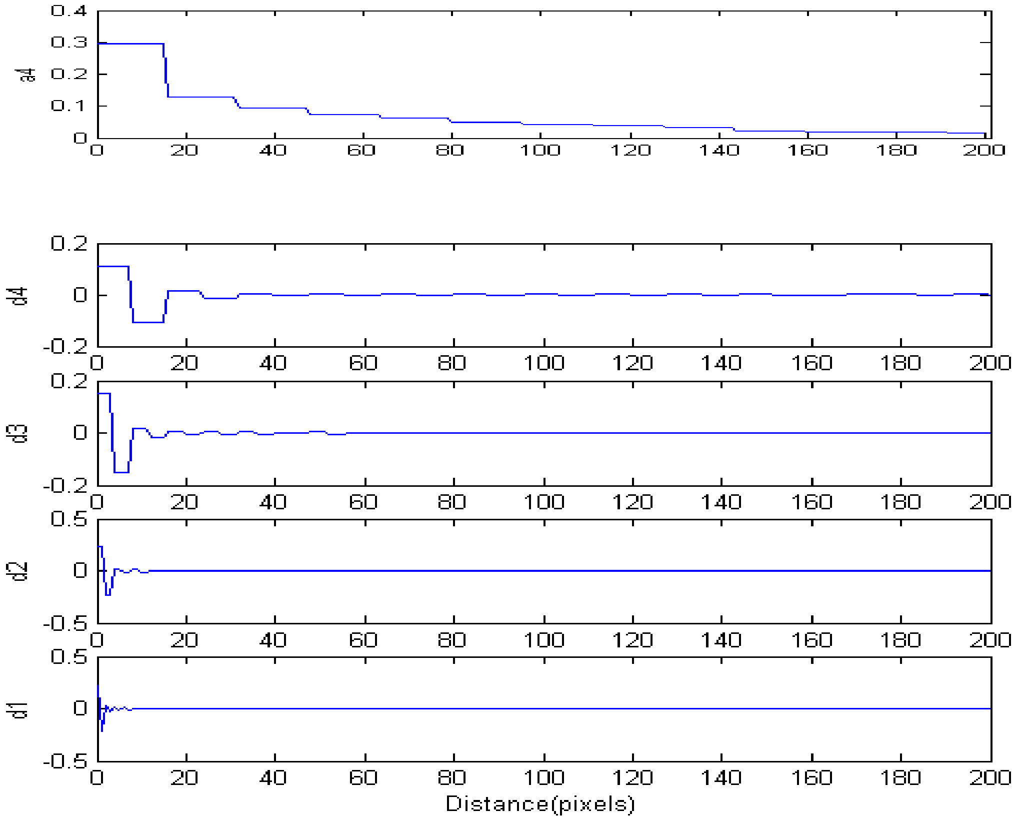

Fig.7.10 Components of auto-correlation decomposed by wavelet

The whole amplitude in low frequency component is 0.2958. At jump point 17, its amplitude is 0.1284. Its amplitude rate is 43.41%. Its changed amplitude is 56.59%. At jump point 33, its amplitude is 0.0935, its amplitude rate is 31.61% and its changed amplitude rate is 11.80%. At jump point 49, its amplitude is 0.0733, its amplitude rate is 24.78% and its changed amplitude is 6.83%. At jump point 65, its amplitude is 0.0629, its amplitude rate is 21.26% and its changed amplitude rate is 3.52%. At jump point 81, its amplitude is 0.0490, its amplitude rate is 16.57% and its changed amplitude rate is 4.70%. Relatively, from jump point 33 on, the amplitude decreases very slowly. The changed amplitude is very small. That is, after point 33, the amplitude is small and almost remains the same. Therefore, the optimum window size should be 33*33 at level 1.

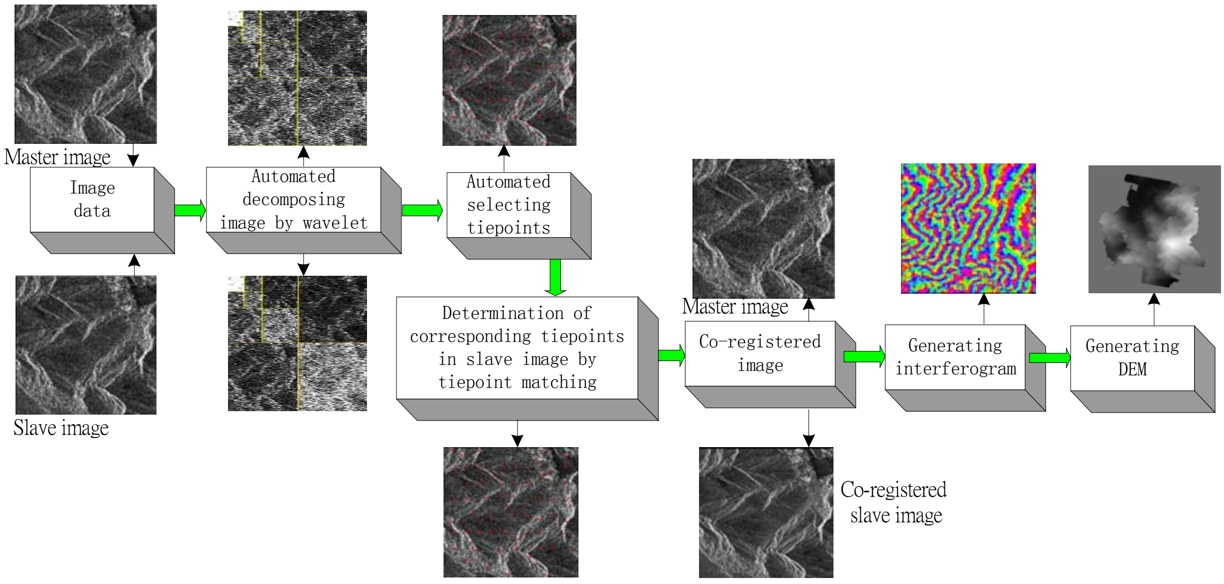

Fig.7.11 Toward automated process for InSAR image

Once the optimum window size has been determined, the tiepoint matching can be implemented. Therefore, the slave image can be registered. The interferogram and DEM can then be generated at last. The toward automated process for InSAR image is shown in Fig.7.11.

7.3 Evaluation of automated co-registration

7.3.1 The quality of interferogram

The image co-registration is automated using the system described in the previous section. The experimental interferogram is shown in Fig.7.12. The data of image processing is included in Table 7.4.

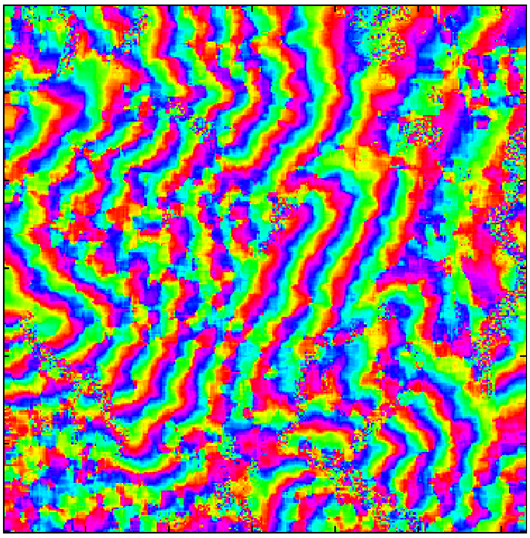

Fig.7.12 Interferogram generated by the automated system

As discussed previously, the visual inspection could reflect the quality of interferogram. That is, if the fringes are clear, the interferogram is good. Otherwise, many speckles indicate bad interferogram. From the interferogram in Fig.7.12, it is obvious that clear fringes can be inspected almost in the whole area and little speckle exists in the interferogram. The SPD is 66,026 radians. The RMSE of tiepoints is 0.0258, which is small. Therefore, the interferogram is good.

Table 7.4 Data of image processing with automated system

Image size (pixel)	Number of feature points	Interferogram	RMSE of tiepoints (pixel)	SPD (radian)	DEM image	δ_{DEM} (m)
1616*336	64	Fig. 7.12	0.0258	66,026	Fig. 7.14	12

7.3.2 Accuracy of DEM

The final product DEM is shown in Fig.7.14. In order to measure the accuracy of DEM, a reference DEM image is used as shown in Fig.7.13.

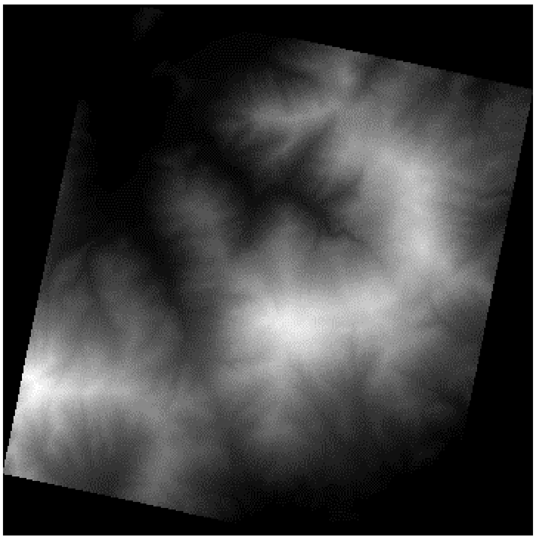

Fig.7.13 A reference DEM image

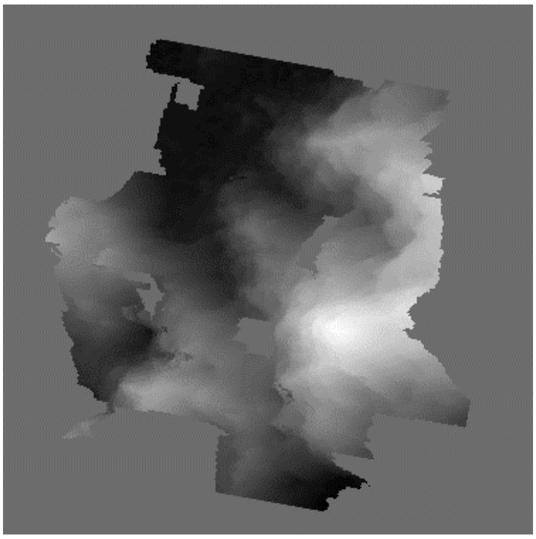

Fig.7.14 DEM image generated by the automated system

The δ_{DEM} of DEM is 12 meters. Obviously, the accuracy of DEM generated based on the automated system is accurate.

7.4 Summary

This chapter aims to automate the processing of image co-registration. Therefore, an automated system for co-registration is described. The system consists of seven operators that are the key factors involved in SAR image co-registration and their details are described. The wavelet plays an important role in the automated operators, such as in automated decomposition of image, automated extraction of feature points and automated determination of optimum window size for tiepoint matching. The co-registration based on the automated system is carried out with a pair of SAR images. The SPD is smaller and the resultant interferogram is better. The accuracy of final product DEM is more accurate.

From the analysis of the results, it is found the co-registration based on the automated system is reliable and accurate. It can be said the automated system is a systematical and an efficient way to improve the accuracy of image co-registration.

Chapter 8

Conclusions

8.1 Summary

The reliability and accuracy of SAR interferometry is affected by many factors. One of the most important factors is the image co-registration, which is the first step of SAR interferometric processing. It significantly affects the quality of the final products of SAR interferometry. This study focuses on the improvement of the accuracy of image co-registration in InSAR.

After the introduction of the principle and the procedure of generating a DEM by InSAR, which serves as a theoretical background for future discussion, detailed descriptions of work carried out in this project are given.

A quantitative measure for the quality of interferograms is proposed based on the phase differences in the interferogram, i.e. the sum of phase differences (SPD). In order to prove its reliability, two simulation experiments have been conducted. Results show that the SPD values reflect the quality of interferograms very well.

When there are no well-defined tiepoints for co-registration, the tiepoints are normally selected in grid form. In this case, in order to investigate the effects of tiepoint interval on reliability of co-registration, four pairs of images have been used for the test. From the results, it has been noticed that the tiepoint interval is not a very sensitive parameter for co-registration. However, it is found that when the grid interval is around 200*30 pixels, the quality of interferogram is good and the DEM is accurate.

If feature points can be detected in an image, it will benefit the results of co-registration. Therefore, the wavelet is used to extract feature points from SAR image to improve the accuracy of co-registration. In the case of feature points in a tight cluster, the tiepoints in grid form, with the interval 200 pixels in row and 30 pixels in column, are also considered. That is, the feature points and the tiepoints are combined together for the co-registration. The experiment based on this way is carried out and the results prove the strategy is reliable.

Then, based on the decomposition of auto-correlation with wavelet, a SAR image has been conducted for the investigation on the determination of optimum window size for tiepoint matching. The auto-correlation is decomposed into components. By analyzing the low frequency component, the optimum window size is determined. Results prove the reliability of this method.

Finally, an automated system for image co-registration is described. The system synchronously considers all factors through fusing all of the previous proposed approaches systematically and efficiently. A SAR image is adopted for testing the efficacy of the automated system. The results show that the automated system is a systematical and efficient way to enhance the accuracy of image co-registration.

8.2 Conclusions

The dissertation presents a systematic approach for the analysis and improvement of the accuracy of image co-registration. Many experimental tests have been carried out to prove the reliability of the proposed approaches. From the experimental results and the theoretical analysis, the following conclusions can be drawn:

(1) The quality of interferogram can be quantitatively measured by its sum of phase differences (SPD);

(2) The tiepoint interval is not a very sensitive parameter for co-registration. However, the grid interval with around 200*30 pixels is an appropriate grid size for tiepoint. It can be used as a guideline for processing SAR image of hill area.

(3) Feature points can be effectively extracted from a SAR image based on wavelet. The reliability of co-registration can be significantly improved by combined use of feature points and grid points;

(4) The optimum window size can be determined based on decomposition of auto-correlation by wavelet;

(5) The accuracy of SAR image co-registration based on automated system can be greatly improved.

8.3 Limitations and recommendations

The SAR interferometric processing is complicated and there are four steps in it, i.e., co-registration, interferogram generation, phase unwrapping and geocoding. The co-registration is one of the most important factors in the interferometric processing. The methods developed in the research are just the first step towards a unified method for the enhancement of SAR interferometry technology. This study is limited to the research of SAR data in Hong Kong. Although a number of issues have been considered in this study, yet, some of them need to be investigated further. The local incidence is the common factor for all images, so it is not considered in the study. It should be considered in further research.

Firstly, the effects of tiepoint interval are tested based on a series of experiments with the SAR data of Hong Kong. More data from different sources should be used for more tests.

Secondly, in all of the experiments in the dissertation, the bi-cubic function is used as the transformation model after tiepoint match in co-registration. Different polynomials, such as bias function, bilinear function and higher order function, can be used as the transformation model. The effects of different transformation models on the reliability of co-registration could also be analyzed.

Thirdly, it is worth making an effort to see if it is efficient to use wavelet transform in other steps of SAR interferometry, such as phase unwrapping, filtering noise from SAR data, etc. More research could be implemented about the effects of different wavelet on the quality of image processing. Some of the other main error sources are worthy of further investigation, such as baseline error and atmospheric error, which are not the main objectives in this dissertation. For the atmospheric modeling, some of achievements on GPS could be good reference. Finally, fusing SAR data from multi-sensors may be one of the effective strategies to get more information and to improve the accuracy of products.

References

Abdelfattah R. and Nicolas J.-M., 2004, Sub-pixelic Image Registration for SAR Interferometry Coherence Optimization, *Proceedings of the XXth ISPRS Congress,* Istanbul, Turkey, 12-23 July 2004, Vol. XXXV, part B3.

Ainsworth, T. L. and Lee, J. S., 1998, A joint adaptive interferometric phase unwrapping and filtering algorithm, *IEEE International Geoscience and Remote Sensing Symposium,* 1: 71-73.

Allen, R. L. and Kamangar F. A., 1992, Registration and Matching using Orthogonal Wavelets, *Proceedings of the IEEE-SP International Symposium on Time-Frequency and Time-Scale Analysis,* 567-570.

Askne, J. and Hagberg, J. O., 1993, Potential of interferometric SAR for classification of land surfaces, *IEEE Proceedings of the International Geoscience and Remote Sensing Symposium (IGARSS'93),* Tokyo, Japan, 18-21 August 1993, 3: 985-987.

Bamler, R., Adam, N., Davidson, G, W. and Just, D., 1998, Noise-induced slope distortion in 2-D phase unwrapping by linear estimators with application to SAR interferometry, *IEEE Transactions on Geoscience and Remote Sensing,* 36 (3): 913-921.

Bamler, R. and Just, D., 1993, phase statistics and decorrelation in SAR interferograms, *IEEE International Geoscience and Remote Sensing Symposium*, Tokoy, Japan, 18-21 Aug., 980-984.

Bao, M., Kwoh, L. K. and Singh, K., 1998, An improved least-squares method for INSAR phase unwrapping, *IEEE International Geoscience and Remote Sensing Symposium*, 1: 62-64.

Burgett, S., 1993, Target location in WGS-84 coordinates using synthetic aperture radar images, *Proceedings of 49th Annual Meeting, Institute of Navigation'93*, 57-65.

Burke, B., 1994, The mathematical microscope: waves, wavelets, and beyond, in Bartusiak, M., et al (eds.), *A Position Named Priscilla, Scientific Discovery at the Frontier*, National Academy Press, 196-235.

Burns, T. J., Rogers, S. K., Oxley, M. F. and Ruck D. W., 1996, A Wavelet Multiresolution Analysis for Spatio-Temporal Signals, *IEEE Transactions on Aerospace and Electronic Systems*, 32 (2): 628-649.

Chan, A. K. and Peng C., 2003, *Wavelet for Sensing Technologies*, Artech House Publishers Press, 237p.

Chui, C. K., 1997, *Wavelet: A Mathematical Tool for Signal Analysis*, Siam Press, 210p.

Cohen, A. and Ryan, R., 1995, *Wavelets and Multiscale Signal Processing*, Chapman & Hall Press, 238p.

Corvi, M. and Nicchiotti, G., 1995, Multiresolution Image Registration, *Proceedings of International Conference on Image Processing*, 224-227.

D'Attellis, C. E. and Fernandez-Berdaguer, E. M., 1997, *Wavelet Theory and Harmonic Analysis in Applied Sciences*, Birkhauser Press, 345p.

Daubechies, I., 1988, Orthonormal Bases of Compactly Supported Wavelets, *Communications on Pure and Applied Mathematics*, XLI: 909-996.

Davis, R. E., Foote, F. S., Anderson, J. M. and Mikhail, E. M., 1981, *Surveying: Theory and Practice*, 6th edition, McGraw-Hill Press, 992p.

Devor, R. A., 1992, Image compression through wavelet transform coding, *IEEE Transactions on Information Theory*, 38 (2), 719-746.

Dummer, G., and Winton, R., 1986, *An Elementary Guide to Reliability*, 3rd edition, Pergamon Press, 47p.

Eldhuset, K., Aanvik, F., and Aksnes, K., 1996, First results from ERS tandem InSAR processing on Svalbard, *http://www.geo.unizh.ch/rsl/fringe96/papers/eldhuset-et-al/* (Last accessed 20 Feb. 2003).

Fonseca, L. M. G. and Costa, M. H. M., 1997, Automatic Registration of Satellite Images, *IEEE Proceedings of Computer Graphics and Image Processing*, 219-226.

Fotnaro, G., 1999, Trajectory deviations in airborne SAR: analysis and compensation, *IEEE Transactions on aerospace and electronic systems*, 35 (3): 997-1009.

Fornaro, G. and Franceschetti, G., 1995, Image registration in interferometric SAR processing, *IEE Proc. Radar, Sonar Navig.*, 142: 291-313.

Franceschetti, G. and Lanari, R., 1999, *Synthetic Aperture Radar Processing,* CRC Press, 307p.

Franceschetti, G.; Lanari, R. and Marzouk, E. S., 1995, Efficient and high precision space-variant processing of SAR data, *IEEE Transactions on Aerospace and Electronic Systems,* 31 (1): 227-237.

Frankich, K., 1993, *Mathematical cartography part one: Geographic map projections,* The University of Calgary press, 320p.

Gabriel, A. K. and Goldstein, R. M., 1988, Crossed orbit interferometry: Theory and experimental results from sir-b, *International Journal of remote Sensing,* 9 (5): 857-872.

Gabriel, A. K., Goldstein, R. M. and Zebker, H. A., 1989, Mapping small elevation changes over large areas: Differential radar interferometry, *Journal of Geophysical Research,* 94 (B7), 9183-9191.

Gatelli, F., Monti, G. A., Parizzi, F., Pasquali, P., Prati, C. and Rocca, F., 1994, The wavenumber shift in SAR interferometry, *IEEE Transactions on Geoscience and Remote Sensing,* 32: 855-864.

Ge, L. L., Tsujii, T. and Rizos, C., 2002, Tropospheric Heterogeneities Corrections in Differential Radar Interferometry, http://www.gmat.unsw.edu.au/snap/publications/ge_etal2002a.pdf (Last accessed 11 Feb. 2003).

Gens, R., 1998, *Quality assessment of SAR interferometric data,* Ph.D. dissertation: Hannover University, Germany, 141p.

Goldstein, R. M. and Werner, C. L., 1998, Radar interferogram filtering for geophysical applications, *Geophysical Research Letters,* 25(21): 4035-4038.

Goldstein, R. M. and Zebker, H. A., 1988, Satellite radar interferometry: two-dimensiona phase unwrapping, *Radio Science*., 23: 713.

Graham, L. C., 1974, Synthetic interferometer radar for topographic mapping, *Proceedings of the IEEE*, 62: 763-768.

Gray, A. L. and Farris-Manning, P. L., 1993, Repeat-pass Interferometry with Airborne Synthetic Aperture Radar, *IEEE Transactions on Geoscience and Remote Sensing*, 31: 180-191.

Gray, A. L., Mattar, K. E. and Farris-Manning, P. J., 1992, Airborne SAR interferometry for terrain elevation, *Proceedings of IGARSS'92*, Houston, Texas, pp.1589-1591.

Guarino, R. and Ibsen, P., Integrated GPS/INS/SAR/GMTI radar precision targeting flight test results, 1995, *Proceedings of 51th Annual Meeting, Institute of Navigation'95*, 373-379.

Guarnieri, A. M. and Prati, C., 1997, SAR Interferometry: A "Quick and Dirty" Coherence Estimatior for DATA Browsing, *IEEE Trans. Geosci.Remote Sensing*, 35 (3), 660-669.

Hanssen, R. F., 2000, *Radar Interferometry Data Interpretation and Error Analysis*, Kluwer Acadamic Publishers Press, 308p.

Hilland, J. E., Stuhr, F. V., Anthony, F., Imel, D., Shen, Y., Jordan, R. and Caro, E. R., 1998, Future NASA spaceborne SAR missions, *IEEE AES Systems Magazine*, November, pp.9-16.

Huang, Y., 2000, An algorithm for interferometric SAR data processing, *Journal of Electronics* (in Chinese), 22 (3), 373-378.

Irving, W. W., Novak, L. M. and Willsky, A. S., 1997, A Multiresolution Approach to Discrimination in SAR Imagery, *IEEE Transactions on Aerospace and Electronic Systems*, 33 (4): 1157-1169.

Ji, Z., Jiang, Y. and Zhang, J., 2000, Automatic Registration Algorithm Based on Wavelet Transform, *Proceeding of the 5th International Conference on Signal Processing*, 2: 979-982.

Joughin, I. R., Kwok, R. and Fahnestock A., 1998, Interferometric estimation of three-dimensional ice-flow using ascending and descending passes, *IEEE Transactions on Geoscience and Remote Sensing*, 36 (1): 25-37.

Kaewkamnerd, N. and Rao, K. R., 2000, Wavelet Based Watermarking Detection Using Multiresolution Image Registration, *IEEE International Technical Conference*, 2: 171-175.

Kaiser, G., 1994, *A Friendly Guide to Wavelets*, Birkhauser Press, 300p.

Kennethr, C., 1998, *Digital image processing*, Tsinghua University Press, 209p.

Kimura, H. and Todo, M., 1997, Baseline estimation using ground points for interferometric SAR, *IEEE International Geoscience and Remote Sensing*, 1: 442-444.

Kwoh, L. K., Chang, E. C., Heng, W. C. A. and Lim, H., 1994, DTM generation from 35-day repeat pass ERS-1 interferometry, *Proceedings of IGARSS'94*, Pasadena, California, 2288-2290.

Lau, K. S., 1998, *Advances in wavelets*, Springer, 282p.

Layne, J. R. and Paschall, R. N., 1994, *Proceedings of 50th Annual Meeting, Institute of Navigation'94*, 157-168.

Li, F. K. and Goldstein, R. M., 1990, Studies of multibaseline spaceborne interferometric sythetic aperture radars, *IEEE Transactions on Geoscience and Remote Sensing*, 28: 88-96.

Li, J. and Zelnio, E., 1996, Target detection with Synthetic Aperture Radar, *IEEE Transactions on aerospace and electronic systems*, 32 (2): 613-627.

Li, Z. and Fan, X. T., 2001, Registration between remote sensing images based on multi-window cross-correlation, *Journal of Image and Graphic*, 6(A)-2: 129-132.

Li, Z. L., 1991, Effects of check points on the reliability of DTM accuracy estimates obtained from experimental tests, *Photogrammetric Engineering & Remote Sensing*, 57 (10): 1333-1340.

Li, Z. L., 1994, A comparative study of the accuracy of digital terrain models (DTMs) based on various data models, *ISPRS Journal of Photogrammetry & Remote Sensing*, 49(1): 2-11.

Li, Z. L., 2001, Orthoimage Generation and Measurement from Single Images, in Chen, Y.Q. and Lee, Y.CH. (eds.), *Geographical data acquisition*, SpringerWienNewYork, 173-183.

Li, Z. L. and Zhu, Q., 2000, *Digital Elevation Model*, Wuhan Technical University of Surveying and Mapping Press, 248p. (in Chinese)

Li, Z. W. and Ding, X. L., 2003, Modeling of atmospheric effects on InSAR measurements with the method of stochastic simulation, *International Archives of Fringe 2003 workshop*, ESA ESRIN, Frascati, Italy, 1-5 Dec., 2003.

Liao, M. S., 2000, *Study on automatic generation of interferogram from InSAR data*, Ph.D dissertation: Wuhan Technical University of Survering and Mapping, 112p. (in Chinese).

Lim, I., Yeo, T.S., Ng, C.S., Lu, Y.H. and Zhang, B.C., 1997, Phase noise filter for interferometric SAR, *IEEE International Geoscience and Remote Sensing*, 1: 445-447.

Lin Q., 1992, New Approaches in Interferometric SAR Data Processing, *IEEE Transaction on Geoscience and Remote Sensing*, 30: 560-567.

Lin, Q., Vesecky, J. F. and Zebker, H. A., 1992, New approaches in interferometric SAR data processing, *Transaction on Geoscience and Remote Sensing*, 30 (3): 560-567.

Liu, G. X., Ding, X. L., Li, Z. L., Chen, Y. Q. and Zhang, G. B., 2001, Co-registration of satellite SAR complex images, *Acta Geodaetica et Cartographica Sinica* (in Chinese), 30 (1): 60-66.

Liu, G. X., 2003, *Mapping of Earth Deformations with Satellite SAR Interferometry: A Study of Its Accuracy and Reliability Performances*, Ph.D dissertation: The Hong Kong Polytechnic University, Hong Kong, China, 229p.

Louis, A. K., Maab, P. and Rieder, A., 1997, *Wavelets: Theory and Applications*, John Wiley & Sons press, 324p.

Ludwig, R., Lampart, G. and Mauser, W., 1998, the determination of hydrological model parameters from airborne interferometric SAR-data, *Journal of Remote Sensing*, 2609-2611.

Madsen, S. N., Zebker, H. A. and Martin, J., 1993, Topographic mapping using radar interferometry: processing techniques, *IEEE Transaction on Geoscience and Remote Sensing*, 31 (1): 246-256.

Maling, D. H., 1992, *Coordinate systems and map projections*, 2nd edition, Pergamon Press, 476p.

Mallat, S. and Hwang, W. L., 1992, Singularity detection and processing with wavelet, *IEEE Trans. On Information Theory*, 38 (2): 617-643.

Marc, S. and Gianfranco, D., 1998, Analysis of speckle noise contribution on wavelet decomposition of SAR images, *IEEE Transaction on Geoscience and Remote Sensing*, 36 (6): 1953-1962.

Massonnet, D., Rossi, M., Carmona, C., Adragna, F., Peltzer, G., Feigl, K. and Rabaute, T., 1993, The displacement field of the Landers earthquake mapped by radar interferometry, *Nature*, 364: 138-142.

Mattar, K.E., Vachon, P.W., Geudtner D., Gray, A.L., Cumming, I.G. and Brubman, M., 1998, Validation of Alpine glacier velocity measurements using ERS tandem-mission SAR data, *IEEE Transaction on Geoscience and Remote Sensing*, 36 (3): 974-984.

Moigne, J. L., Campbell, W. J. and Cromp R. F., 2002, An Automated Parallel Image Registration Technique Based on the Correlation of Wavelet Features, *IEEE Transactions on Geoscience and Remote Sensing*, 40 (8): 1849-1864.

Moigne, J. L., Netanyahu, N. S. and Masek, J. G., 2001, Robust Matching of Wavelet Features for Sub-pixel Registration of Landsat Data, *IEEE International Geoscience and Remote Sensing Symposium*, 2: 706-708.

Mu, L. H., 1999, *Fourier analysis and wavelets analysis*, Shandong University (in Chinese), 407p.

Porcello, L. J., Jordan, R. L., Zelenka, J. S., Adams, G. F., Phillips, R. J., Brown, W. E., Jr., Ward, S. H., and Jackson, P. L., 1974, The Apollo lunar sounder radar system, *Proceedings IEEE*, 62: 769–783.

Resnikoff, H. L. and Wells, R. O. Jr., 1998, *Wavelet Analysis*, Springer Press, 435p.

Rosen, P.A., Hensley, S., Zebker, H. A., Webb, F. H. and Fielding, E. J., 1996, Surface deformation and coherence measurements of Kilauea Volcano, Hawaii, from SIR-C radar interferometry, *Journal of Geophysical Research*, 101: 23109-23125.

Seisuke, F. and Haruto, H., 1998, Land cover classification from multifrequency polarimetric synthetic aperture radar data using wavelet-based textural information, *IEEE International Geoscience and Remote Sensing Symposium Proceedings*, 357-359.

Sherwin, C. W., Ruina, J. P., and Rawcliffe, R. D., 1962, Some early developments in synthetic aperture radar systems, *IRE Transactions on Military Electronics*, 6: 111-116.

Shi, J. C. Dozier, J and Rott, H., 1994, Snow mapping in Alpine regions with synthetic aperture radar, *IEEE Transactions on Geoscience and Remote Sensing*, 32(1): 152-158.

Singh, K., Stussi, N., Keong, K. L. and Hock, L., 1997, Baseline estimation in interferometric SAR, *IEEE International Geoscience and Remote Sensing*, 1: 454-457.

Solaas, G. A., Gatelli, F., and Campbell, 1996, *Initial testing of ERS tandem data quality for InSAR applications*, ESR technical report.

Stevens, D. R., Cumming, I. G. and Gray, A. L., 1995, Options for airborne interferometric SAR motion compensation, *IEEE Trans. On Geoscience and Remote Sensing*, 33: 409-419.

Tai, J. C., 1992, *An introduction to wavelets* (in Chinese), Xi'an Jiaotong University, 367p.

Tang, Y. Y., Yang, L. H., Liu J. and Ma, H., 2000, *Wavelet Theory and Its Application to Pattern Recognition*, World Scientific Press, 345p.

Tobita, M., S. Fujiwara, Ozawa, S. and Rosen, P. A., 1998, Deformation of the 1995 North Sakhalin earthquake detected by JERS-1/SAR interferometry, *Earth Planets Space*, 50: 313-335.

Toutin, T. and Gray, L., 2000, State-of-the-art of Elevation Extration from Satellite SAR Data, *ISPRS Journal of Photogrammetry & Remote Sensing*, 55: 13-33.

Urban, *M., 2003,* Harris Interest Operator, http://cmp.felk.cvut.cz/cmp/courses/dzo/resources/lecture_harris_urban.pdf, (Last accessed 17 Dec. 2004).

Usevitch, B. E., 2001, A Tutorial on Modern Lossy Wavelet Image Compression: Foundations of JPEG 2000, *IEEE Signal Processing Magazine*, 18 (5): 22-35.

Varkekamp, C. and Hoekman, D. H., 2001, Segmentation of high-resolution InSAR data of a tropic forest using Fourier parameterized deformable models, *International Journal of Remote Sensing*, 22 (12), 2339-2350.

Wan, F.G., 1990, *Digital processing of remotely sensed images,* Huazhong Polytechnical University, 198p. (in Chinese).

Wangensteen, B., Weydahl, D. J. and Hagen, J. O., 1999, Mapping glacier velocities at Spitsbergen using ERS tandem SAR data, *IEEE Proceedings of International Geoscience and Remote Sensing Symposium (IGARSS)*, 28 June-2 July 1998, Hamburg, Germany, 4: 1954-1956.

Wegmuller, U. and Werner, C., 1997, Retrieval of vegetation parameters with SAR interferometry, *IEEE Transactions on Geoscience and Remote Sensing,* 35: 18-24.

Weydahl, D. J., 1991, Change detection in SAR images, *IEEE International Geoscience and Remote Sensing Symposium,* Espoo, Finland, 3-6 June, 1421-1424.

Weydahl, D. J., 1998, *Analysis of satellite SAR images for change detection over land areas*, PhD thesis, University of Oslo, Norway, 152p.

Weydahl, D. J., 2001, analysis of ERS SAR coherence umages acquired over vegetated areas and urban features, *International Journal of Remote Sensing,* 22(14): 2811-2830.

Wiley, C. A., 1965, *Pulsed Doppler radar methods and apparatus,* U.S. Patent 3196436, filed in 1954.

Wivell, C. E., Steinwand, D. R., Kelly, G. G. and Meyer, D. J., 1992, Evaluation of terrain models for the geocoding and terrain correction of synthetic aperture radar (SAR) image, *IEEE Transactions On Geoscience and Remote Sensing,* 30 (6): 1137-1143.

Wood, J. D. and Fisher, P. F., 1993, Assessing interpolation accuracy in elevation models, *IEEE Computer Graphics and Applications,* 13 (2): 48-56.

Yang, Q. Y. and Wang, C., 1999, Registration of INSAR complex images and interferogram enhancement, *Journal of Remote Sensing* (in Chinese), 3 (2): 122-131.

Yu, Q., Tian J. and Liu J., 2002, Automatic multisensor image registration using wavelet transform, *Proceedings of the 6th international conference on signal processing,* 1: 616-619.

Zebker, H. A., Rosen, P. A., Goldstein, R. M., Gabriel, A. and Werner, C. L., 1994a, On the derivation of coseismic displacement fields using differential radar interferometry: The Landers earthquake, *Journal of Geophysical Research,* 99 (B10): 19617-19634.

Zebker, H. A., Rosen, P. A., and Hennsley, S., 1997, Atmospheric effects in interferometric synthetic aperture radar surface deformation and topographic mapping, *Journal of Geophysical Research*, 102 (B4): 7547-7563.

Zebker, H. A., Rosen, P. A., Hennsley, S. and Mouginis-Mark, P. J., 1996, Analysis of active lava flows on Kilauea volcano, Hawaii, using SIR-C radar correlation measurements, *Geology*, 24: 495-498.

Zebker, H. A. Werner, C. L., Rosen, P. A. and Hensley, S., 1994b, Accuracy of topographic maps derived from ERS-1 interferometric radar, *IEEE Transaction on Geoscience and Remote Sensing*, 32 (4): 823-836.

Zou, W. B., Li, Z. L., Ding, X. L., Chen, Y. Q. and Liu, G. X., 2002, Effects of the interval of tiepoints on the reliability of SAR image co-registration, *International Archives of Photogrammetry and Remote Sensing*, XXXIV(2), 639-644.

Zou, W. B., Li, Z. L., Ding, X. L. and Chen, Y. Q., 2003, Effects of the interval of tiepoints on the quality of co-registration in InSAR, *Proceedings of 7th South East Asian Survey Congress*, 3-7 Nov. 2003, Hong Kong.